Application of the Lagrangian descriptors method to Hamiltonian systems with emphasis to models of barred galaxies

Dylan Grant Theron
Supervisor: Professor Haris Skokos

University of Cape Town
Faculty of Science
Department of Mathematics and Applied Mathematics

22nd May 2024

Abstract

The Lagrangian descriptors (LDs) method is a numerical technique that assigns to an orbit's initial condition a positive scalar value. Its implementation permits the conversion of a dynamical system's phase space into a scalar field which can be used to distinguish regions of different dynamical behaviours and ultimately reveal structures in the system's phase space. In this work, we apply the LDs method to different dynamical systems. We first study a Hamiltonian system of galactic type to highlight normally hyperbolic invariant manifolds (NHIMs), examining the impact of different pattern speeds and energy levels on the NHIMs' structure and determine how these features influence orbital morphologies seen in the model's configuration space. Thereafter, we apply the LDs method to a dynamical system whose evolution is governed by fractional ordinary differential equations (FDEs) and showcase the utility of this method in qualitatively revealing phase space structures for systems described by FDEs. In our study, we implement two numerical techniques to integrate such systems, namely the Grünwald-Letnikov (GL) method to solve Caputo type derivatives and the GL approximation for Riemann-Liouville derivatives. We emphasise the differences between these two methods and examine the resulting phase space structures. Additionally, we investigate the effect of the final integration time and the order of the involved fractional derivatives on the features seen in the system's phase portraits, which are revealed through the computation of the LDs for large ensembles of orbits.

List of acronyms

CPU:	central processing unit
dof:	degrees of freedom
eom:	equations of motion
FDE:	fractional order ordinary differential equation
GL:	Grünwald-Letnikov
IC:	initial condition
LD:	Lagrangian descriptor
NHIM:	normally hyperbolic invariant manifold
ODE:	ordinary differential equation
OFM:	origin-fate map
PSS:	Poincaré Surface of Section
RK:	Runge-Kutta method

Acknowledgements

I would like to begin by expressing my sincerest thanks to my supervisor, Professor Haris Skokos, for his unwavering support and guidance. He not only provided an enriching environment for me to grow academically, but also offered support as I faced personal challenges. Next, I wish to thank my past and present colleagues in the Nonlinear Dynamics and Chaos research group: Dr. Malcolm Hillebrand, Dr. Arnold Ngapasare, Henok Moges, Sané Erasmus, Jean-Jacq Du Plessis, Sebastian Zimper, Samuel Cheong, and Cassandra Barbis for their stimulating discussions. For the direction that he provided when examining a dynamical system of galactic type, I would like to thank Dr. Matthaios Katsanikas. To Professor Hadi Susanto and Assistant Professor Makrina Agaoglou, thank you for your advice and assistance on our work on applying the Lagrangian descriptors method to dynamical systems whose evolution is governed by fractional ordinary differential equations. I would like to express my utmost thanks to my mother for her encouragement and support throughout my degree. Additionally, I would like to thank the Center for High Performance Computing and the High Performance Computing facility of UCT, for allowing me access to the computing facilities that I utilised throughout my studies. I wish to thank the University of Cape Town and the Harry Crossley Foundation for their financial support. Finally, I would like to thank those closest to me for your encouragement and mentorship during this journey.

Contents

Chapter 1

Introduction

Mathematically modeling various natural and artificial phenomena is a challenging procedure that can be undertaken using tools from an array of mathematical fields. Regardless of how a phenomenon is modeled, it is important to understand the intricate and complex dynamical behaviours that emerge from the evolution of a system. This evolution can be defined by the solution of a dynamical system's ordinary differential equations (ODEs) [1] or fractional ordinary differential equations (FDEs) [2]. A large portion of dynamical systems are described by nonlinear equations. Thus, finding analytical solutions to these ODEs or FDEs is not feasible and consequently numerical approaches are required. In this thesis, we use various numerical approaches to find solutions of ODEs and FDEs as well as to investigate the dynamics of nonlinear dynamical systems. Furthermore, we discuss the advantages and shortfalls of these approaches. Additionally, we have suggested methods to improve on an integration technique for FDEs.

Following the evolution of a dynamical system, we can observe patterns and structures in its phase space (mathematical space representing all possible states of a dynamical system). These geometrical structures can be revealed using a numerical technique called the Lagrangian descriptors (LDs) method (see e.g., [3] and references therein). The structures highlighted by the LDs method also separate phase space regions which display qualitatively different dynamical behaviour, providing in this way much information about the system's dynamics. Additionally, this tool is simple to implement and computationally inexpensive.

In this thesis we extended the applicability of the LDs method to some basic dynamical systems of diverse nature. In that spirit, we first apply the LDs method to a dynamical system which describes the motion of stars within a rather simple galactic model [4]. In particular, we examine the influence of the underlying phase space structures on potential orbital morphologies supported by the system's orbits. Secondly, using the LDs method we make a novel attempt to geometrically understand the phase space of a dynamical system whose evolution is governed by FDEs.

The thesis is structured as follows. In Chapt. 2, we present the various dynamical systems that will be used throughout this work. In Chapt. 3 we then showcase the

numerical integration schemes that are applied to the different dynamical systems, and describe the LDs method together with some of its properties that will prove useful at a later point in the thesis. Chapter 4 focuses on the application of the LDs method to a galactic type dynamical system, and explores how this method is used to study the orbits of stars and their associated morphologies. Then in Chapt. 5, we apply the LDs method to a dynamical system described by FDEs to observe the underlying phase space structures. Lastly, we summarise the results of this thesis and make concluding remarks in Chapt. 6.

Chapter 2

Dynamical systems

Understanding complex phenomena requires a foundation that allows for the co-action of variables throughout their dynamical evolution. Dynamical systems assume this fundamental role, while also acting as a platform from which we can expose, analyse, and comprehend certain intricate dynamical behaviours. It is, therefore, essential to establish formal notations for the systems pertaining to the research that shall be conducted throughout this thesis. The current chapter is constructed in a manner which allows for the attainment of this goal. We begin by providing a brief description of the broad notion of a dynamical system and reasons why such systems are important, followed by an introduction to generalised coordinates and an exposition of Lagrangian mechanics. This will serve as a segue into an illustration of Hamiltonian mechanics. Hamiltonian mechanics forms the basis from which dynamical systems are studied throughout the thesis. Lastly, we lay the foundation of systems consisting of FDEs. In contrast to their ODE counterparts, these systems tend to be challenging to interpret physically. Nonetheless, their utility in this research will be featured at a later juncture.

2.1 Preliminaries

Dynamical systems are often described in the language of ODEs. It is, therefore, important to define the notion of a general system of differential equations, which takes the form

$$\dot{\mathbf{x}} = \mathbf{f}(\mathbf{x}, t), \quad \mathbf{x} \in \mathbb{R}^n, \tag{2.1}$$

where $\mathbf{x}$ is a real vector of n dependent variables, $\dot{\mathbf{x}}$ is the usual time (t) derivative of $\mathbf{x}$, $\mathbf{f}$ is the vector field ($\mathbf{f} : \mathbb{R}^n \to \mathbb{R}^n$), and $\mathbf{f}$ is continuously differentiable [5].

General dynamical systems that have an explicit dependency on time are called non-autonomous, and those that do not contain an explicit dependence on time are termed autonomous systems. Both types of systems are ensured to have a unique solution [5]. This unique solution is referred to as the flow, $\phi(\mathbf{x}_0, t)$, which describes the trajectory associated with an initial condition (IC), $\mathbf{x}(0) = \mathbf{x}_0$, over a time

interval, $t \in [0, t_{\mathcal{N}}]$, and is given as

$$\mathbf{x}(t) = \phi(\mathbf{x}_0, t), \tag{2.2}$$

where $\mathbf{x}(t) \in \mathbb{R}^n$. Through the observation of the trajectories associated with various ICs, one is able to witness trends displayed by the dynamical system. The trends exhibited by the trajectories allow for the possibility to recognise potential reasons for various dynamical phenomena seen in a variety of research areas (see for example [6, 7, 8]).

Dynamical systems can be described by a multitude of distinct approaches. Some of the earliest systems studied come from classical mechanics, which relates to the dynamics of macroscopic objects. Newtonian mechanics is perhaps the earliest formalism of classical mechanics. The interested reader is, for example, referred to Chapt. 2 of [9] for a complete elucidation of this topic. The notion of Newtonian mechanics employs the use of the Cartesian coordinates to recount the dynamics of the underlying system in terms of its spatial position. While an object's spatial coordinates are useful in describing its dynamical evolution, it may not be the most efficient approach. The reason for this pitfall is due to a dynamical system being, potentially, constrained to a certain geometrical configuration (see for example Sect. 10.2 of [10]). There are, however, formulations of classical mechanics which utilise coordinates which are more general and thus, allow for a more comprehensive analysis of a system's governing dynamics, such as the Lagrangian and Hamiltonian mechanics. Such coordinates are called *generalised coordinates* and will be discussed in the subsequent section of this chapter.

2.2 Generalised coordinates

Dynamical systems can be used to describe certain phenomena through the evolution of various variables and parameters. Additionally, dynamical systems offer a lens through which a system's associated phenomena can be better understood. As stated in Sect. 2.1, Euclidean coordinates are not always an optimal choice. To showcase an example where Euclidean coordinates are not best, we examine the motion of a pendulum along a fixed arc of radius r (Fig. 2.1).

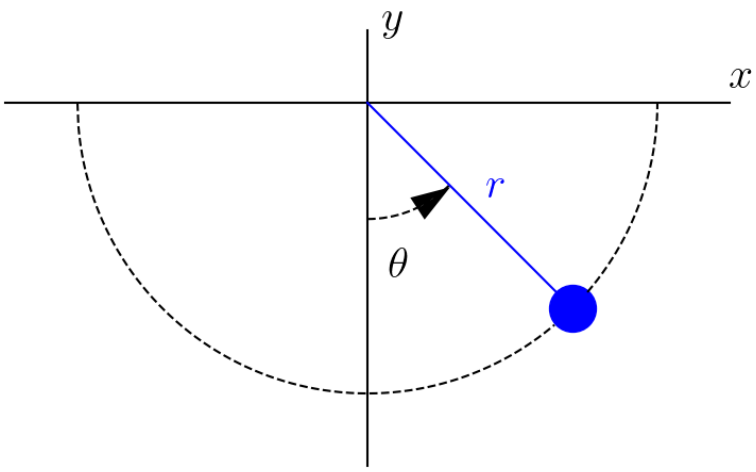

Figure 2.1: Pendulum of fixed length r swinging in the x-y plane.

The motion of the pendulum can be described by using the coordinates $x(t)$ and $y(t)$ (Euclidean coordinates at each point in time t). However, it is beneficial to mathematically reformulate the system's description by using the constant r and the angular displacement $\theta(t)$. This is because the $x(t)$ and $y(t)$ coordinates can be described by the singular variable, $\theta(t)$, through the following equations

$$\begin{aligned} x(t) &= r\cos(\theta(t)), \\ y(t) &= r\sin(\theta(t)). \end{aligned} \tag{2.3}$$

From this simple example, it is clearly observed that only one variable ($\theta(t)$) is required to describe the system in totality. The notion of describing the dynamics of a system, in terms of the minimum number of independent parameters, is a trait of the generalised coordinates, q_i. The number of generalised coordinates, necessary to fully describe a system's dynamics, is equal to the so-called system's degrees of freedom (dof). A consequence of the independent variables characterising all feasible configurations of a dynamical system, is that they define the dimensionality of what is called *configuration space*.

2.3 Lagrangian mechanics

Lagrangian mechanics (discussed in this section) and Hamiltonian mechanics (presented in the subsequent section of this chapter) are reformulations of the classical, Newtonian, mechanics into an elegant mathematical formulation using generalised coordinates. The introduction to Lagrangian mechanics provided here will act as a precursor to the exposition of Hamiltonian mechanics. The reason that the current section acts as a segue into Hamiltonian mechanics is because it defines beneficial tools which are used in Hamiltonian mechanics and due to the fact that Hamiltonian mechanics can be directly derived from Lagrangian mechanics through a Legendre transformation [11]. Descriptions for both classes of mechanics will follow a similar format to that given in [9].

The dynamical properties of a system can be exposed through the system's potential (V) and kinetic (T) energies, by means of the Lagrangian function L (for example Chapt. 4.2 of [9] mentions that it was first described by Lagrange in 1811)

$$L = L(q_1, \ldots, q_N, \dot{q}_1, \ldots, \dot{q}_N) = T - V, \tag{2.4}$$

where N is the system's dof. The Lagrangian function provides the possibility to examine the evolution of the system's path, C, from point S_1 to point S_2, in the configuration space. Thus, these points correspond to the state of the system at the chronological times t_1 and t_2 ($t_1 < t_2$). Provided that the forces are conservative (meaning that the forces experienced by particles in the system are independent of the path taken by the particle), the system's evolution over $t \in [t_1, t_2]$ will permit the line integral

$$\int_C L\, dt, \tag{2.5}$$

to obtain its extremum. The extremum principle is termed the *Hamiltonian principle*. As discussed on pg. 81 of [9], the Hamiltonian principle shows that a system will always evolve in the most efficient manner. An example of an equation whose solution allows for the Hamiltonian principle to be met is the *Lagrange* (*Euler-Lagrange*) equation. To derive the Lagrange equation, a function $y(x)$, from point $x_1 = x(t_1)$ to point $x_2 = x(t_2)$, has to be found such that it satisfies the Hamiltonian principle. That is the integral

$$I = \int_{x_1}^{x_2} f(y, y', x)\, dx, \tag{2.6}$$

attains an extremum, where $f(y, y', x)$ is a known function and $y' = \frac{dy}{dx}$. Without loss of generality, the boundary values of the function, $y_1 = y(x_1)$ and $y_2 = y(x_2)$, can be provided in advance.

Although the goal is to determine the optimal path of the function, y, it is important to note that there are infinitely many paths between points x_1 and x_2. These alternate pathways can be parametrised through the introduction of an arbitrary function $h = h(x)$, which vanishes at the points x_1 and x_2, and a parameter a as

$$y(x, a) = y(x, 0) + ah(x), \tag{2.7}$$

where $y(x, 0)$ is the optimal path. By implementing (2.7), the integral of (2.6) can be rewritten in terms of the parametrised pathways, while gaining dependency on a, such that

$$I(a) = \int_{x_1}^{x_2} f(y(x, a), y'(x, a), x)\, dx. \tag{2.8}$$

For (2.8) to possess an extremum at $a = 0$, the derivative $\frac{\partial I}{\partial a}$ must equal zero at the value of $a = 0$. The derivative can be written explicitly as

$$\begin{aligned}\frac{\partial I}{\partial a} &= \int_{x_1}^{x_2} \left(\frac{\partial f}{\partial y}\frac{\partial y}{\partial a} + \frac{\partial f}{\partial y'}\frac{\partial y'}{\partial a} \right) dx \\ &= \int_{x_1}^{x_2} \frac{\partial f}{\partial y}\frac{\partial y}{\partial a}\, dx + \int_{x_1}^{x_2} \frac{\partial f}{\partial y'}\frac{\partial y'}{\partial a}\, dx \\ &= \int_{x_1}^{x_2} \frac{\partial f}{\partial y}\frac{\partial y}{\partial a}\, dx + \int_{x_1}^{x_2} \frac{\partial f}{\partial y'}\frac{\partial^2 y}{\partial x \partial a}\, dx \\ &= \int_{x_1}^{x_2} \frac{\partial f}{\partial y}\frac{\partial y}{\partial a}\, dx + \left[\frac{\partial f}{\partial y'}\frac{\partial y}{\partial a} \right]_{x_1}^{x_2} - \int_{x_1}^{x_2} \frac{d}{dx}\left(\frac{\partial f}{\partial y'} \right)\frac{\partial y}{\partial a}\, dx,\end{aligned} \tag{2.9}$$

where $\frac{\partial y}{\partial a} = h(x)$, as we can easily see from (2.7). The derivative may be further simplified by recalling that $h(x) = 0$ at the points x_1 and x_2. Thus, $\left[\frac{\partial f}{\partial y'}\frac{\partial y}{\partial a} \right]_{x_1}^{x_2} = 0$ and the derivative, (2.9), is further simplified to

$$\begin{aligned}\frac{\partial I}{\partial a} &= \int_{x_1}^{x_2} \frac{\partial f}{\partial y}\frac{\partial y}{\partial a}\, dx - \int_{x_1}^{x_2} \frac{d}{dx}\left(\frac{\partial f}{\partial y'} \right)\frac{\partial y}{\partial a}\, dx \\ &= \int_{x_1}^{x_2} \frac{\partial f}{\partial y}\frac{\partial y}{\partial a} - \frac{d}{dx}\left(\frac{\partial f}{\partial y'} \right)\frac{\partial y}{\partial a}\, dx \\ &= \int_{x_1}^{x_2} \left[\frac{\partial f}{\partial y} - \frac{d}{dx}\left(\frac{\partial f}{\partial y'} \right) \right]\frac{\partial y}{\partial a}\, dx.\end{aligned} \tag{2.10}$$

For f to be an extremum, it is necessary that $\frac{\partial I}{\partial a} = 0$. Due to the arbitrary nature of $\frac{\partial y}{\partial a} = h(x)$, the integrand must equal zero over the entire interval, to ensure that an extremum is achieved. Therefore,

$$\frac{\partial f}{\partial y} - \frac{d}{dx}\left(\frac{\partial f}{\partial y'} \right) = 0, \tag{2.11}$$

which is known in the literature as the *Lagrange* (or *Euler-Lagrange*) *equation*. The solution, $y(x)$, to this equation ensures that (2.6) attains its extremum.

If y is a vector of n functions, the generalisation follows the same methodology, yielding the Lagrange equations as:

$$\frac{\partial f}{\partial y_i} - \frac{d}{dx}\left(\frac{\partial f}{\partial y_i'} \right) = 0, \quad i = 1, 2, \ldots, n. \tag{2.12}$$

As the Hamiltonian principle requires that a Lagrangian function be used in (2.5), we can substitute the generic function, $f(y, y', x)$, with the Lagrangian function, (2.4), to yield

$$\frac{\partial L}{\partial q_i} - \frac{d}{dt}\left(\frac{\partial L}{\partial \dot{q}_i} \right) = 0, \quad i = 1, 2, \ldots, n, \tag{2.13}$$

which are called the *Lagrangian equations of motion* (Lagrangian eom), and describe the dynamics of the underlying system.

The Lagrangian function is defined as the difference between kinetic and potential energy, as seen in (2.4). However, the total energy of the system is obtained through the summation of the kinetic and potential energies, $T + V$. The total energy is used in Hamiltonian mechanics and is advantageous because it allows one to determine if a system conserves its energy. Furthermore, Lagrangians may contain cyclic coordinates, i.e., which do not appear in the Lagrangian but the corresponding velocity does. Therefore, the eom include the equations relating to the cyclic coordinate (see [9]). In contrast, the Hamiltonian does indeed decrease the number of equations if a cyclic coordinate exists. An additional difference between Hamiltonian mechanics and Lagrangian mechanics stems from the fact that the Lagrangian utilises a system's generalised coordinates and the associated velocities. The Hamiltonian instead uses generalised coordinates, q_i, and conjugate momenta, p_i, where the conjugate momenta is defined as

$$p_i = \frac{\partial L}{\partial \dot{q}_i}. \tag{2.14}$$

Thus, as we transition from Lagrangian mechanics to Hamiltonian mechanics, we transition from N second order ODEs to $2N$ first order ODEs, where N is the dimensionality of the system.

2.4 Hamiltonian mechanics

Hamiltonian mechanics will serve as the foundational framework for all studies pertaining to systems consisting of ODEs in this research. The focal point of this section is the definition of the Hamilton's equations of motion (eom), as they can be integrated to determine the flow of the various systems of interest. This section follows a similar format as seen in Chapt. 4.5 of [9].

The definition of generalised momenta, p_i,

$$p_i = \frac{\partial L}{\partial \dot{q}_i}, \tag{2.15}$$

allows for the replacement of the Lagrangian by a function which has dependency on both q_i and p_i. Altering of the Lagrangian, by means of the introduction of generalised momenta, is achieved through the implementation of the Legendre transformation (see e.g., [11]) which is a transformation from one quantity (in our case the generalised velocity) to the conjugate quantity (in our case the generalised momentum). To demonstrate how this is achieved, a function $f = f(x, y)$ is considered along with the function's differential

$$df = \frac{\partial f}{\partial x}dx + \frac{\partial f}{\partial y}dy = udx + vdy, \tag{2.16}$$

where u and v represent $\frac{\partial f}{\partial x}$ and $\frac{\partial f}{\partial y}$, respectively. In addition, a new function, g, can be defined as

$$g = ux - f(x, y), \tag{2.17}$$

with its differential being

$$dg = udx + xdu - udx - vdy = xdu - vdy. \tag{2.18}$$

Thus,

$$dg = \frac{\partial g}{\partial u}du + \frac{\partial g}{\partial y}dy. \tag{2.19}$$

Through the observation of (2.19), it is seen that the function g is only dependent on u and y.

Similarly, the Lagrangian can be transformed to derive the *Hamiltonian*, H, for a system in the following manner

$$H = H(\mathbf{q}, \mathbf{p}, t) = \sum_{i=1}^{N} \dot{q}_i q_i - L(\mathbf{q}, \dot{\mathbf{q}}, t), \tag{2.20}$$

where $\mathbf{q} = (q_1, q_2, \ldots, q_N)$, $\mathbf{p} = (p_1, p_2, \ldots, p_N)$, $\dot{\mathbf{q}} = (\dot{q}_1, \dot{q}_2, \ldots, \dot{q}_N)$, and N is the system's number of dof. The total differential of the Hamiltonian can be obtained in the following manner:

$$\begin{aligned} dH &= \sum_{i=1}^{n} \dot{q}_i dp_i + \sum_{i=1}^{n} p_i d\dot{q}_i - \sum_{i=1}^{n} \frac{\partial L}{\partial q_i}dq_i - \sum_{i=1}^{n} \frac{\partial L}{\partial \dot{q}_i}dq_i - \frac{\partial L}{\partial t}dt \\ &= \sum_{i=1}^{n} \dot{q}_i dp_i + \sum_{i=1}^{n} p_i d\dot{q}_i - \sum_{i=1}^{n} \frac{\partial L}{\partial q_i}dq_i - \sum_{i=1}^{n} p_i d\dot{q}_i - \frac{\partial L}{\partial t}dt. \end{aligned} \tag{2.21}$$

From the Lagrangian eom, (2.13), we can deduce

$$\frac{\partial L}{\partial q_i} = \frac{d}{dt}\frac{\partial L}{\partial \dot{q}_i} = \frac{d}{dt}p_i = \dot{p}_i. \tag{2.22}$$

Therefore, the differential takes the form

$$dH = \sum_{i=1}^{N} \dot{q}_i dp_i - \sum_{i=1}^{N} \dot{p}_i dq_i - \frac{\partial L}{\partial t}dt. \tag{2.23}$$

However, we can also find the differential utilising the chain rule of (2.20), as

$$dH = \sum_{i=1}^{N} \frac{\partial H}{\partial q_i}dq_i + \sum_{i=1}^{N} \frac{\partial H}{\partial p_i}dp_i + \frac{\partial H}{\partial t}dt. \tag{2.24}$$

Equating the two differentials, (2.23) and (2.24), it is seen that

$$\begin{aligned}\frac{\partial H}{\partial p_i} &= \dot{q}_i, \\ \frac{\partial H}{\partial q_i} &= -\dot{q}_i, \\ \frac{\partial H}{\partial t} &= -\frac{\partial L}{\partial t}.\end{aligned} \tag{2.25}$$

Equations (2.25) are the so-called *Hamiltonian eom*, where the generalised coordinates, q_i, and conjugate momenta, p_i, are considered as independent variables. The third equation of motion in an autonomous system lead to

$$\frac{\partial H}{\partial t} = -\frac{\partial L}{\partial t} = 0, \tag{2.26}$$

and thus, there are only $2N$ first order eom, where N is the system's dimensionality. An additional result which is observed from (2.26), is that the value of H is constant for autonomous systems and therefore is a conserved quantity. This principle is known as the *conservation of energy*.

2.5 Dynamical systems described by fractional differential equations

Throughout this chapter, introductions have been made to various dynamical systems composed of differential equations of integer orders. What about dynamical systems described by FDEs? It is the goal of this section to introduce and investigate systems which are built upon differential equations of non-integer orders. The full history of this subject is not addressed in this study; for additional information consult [12]. The reason for our interest in fractional calculus stems from its recent historical development. During the 1970s, fractional calculus experienced a change from being a purely abstract field of study to one which contains utility in fields pertaining to various applications such as electromagnetism [13], viscoelasticity [14], fluid mechanics [15], electrochemistry [16], population dynamics [17], and optical solitons [18].

Unlike classical derivatives, there are several definitions for fractional derivatives. Some of these definitions include the left and right Grünwald-Letnikov (GL) derivatives [19], the left and right Riemann-Liouville derivatives [2], the left and right Caputo derivatives [20], and the Riesz derivative [2], to name a few. For the purpose of this work, we shall only define the Riemann-Liouville derivative, the Caputo derivative, and the GL derivative as in [21].

Most definitions of fractional derivatives are described by the action of a differential operator over the time interval $[a, t]$, as $D^{\alpha}_{a,t} f(t)$. For reasons of simplicity, the interval $[0, t]$ is instead considered and $a = 0$ is omitted as an index. Let $f(\tau)$ be

a general function that satisfies some smoothness conditions in every finite interval $(0, t)$. The finite interval is showcased as an equidistant grid of the form

$$0 = \tau_0 < \tau_1 < \ldots < \tau_N < \tau_{N+1} = t, \tag{2.27}$$

and $\tau_{k+1} - \tau_k = h$, $k = 0, 1, 2, \ldots, N$, is the step size between the equidistant grid points. The *Riemann-Liouville derivative* is then defined as

$$D_R^\alpha f(t) = \begin{cases} \dfrac{1}{\Gamma(m-a)} \dfrac{d^m}{dt^m} \displaystyle\int_0^t \frac{f(\tau)}{(t-\tau)^{\alpha+1-m}} d\tau & m-1 \leq \alpha < m \\ \dfrac{d^m f(t)}{dt^m} & \alpha = m, \end{cases} \tag{2.28}$$

where the subscript R indicates that this is the Riemann-Liouville derivative, $m \in \mathbb{N}$, $\Gamma(x)$ is the usual Gamma function, and $\frac{d^m}{dt^m}$ is a time derivative of integer, m, order. Following again [21], the *Caputo derivative* is defined as

$$D_*^\alpha f(t) = \begin{cases} \dfrac{1}{\Gamma(m-a)} \displaystyle\int_0^t \frac{f^{(m)}(\tau)}{(t-\tau)^{\alpha+1-m}} d\tau & m-1 \leq \alpha < m \\ \dfrac{d^m f(t)}{dt^m} & \alpha = m. \end{cases} \tag{2.29}$$

It is important to note that the two definitions seen here are not equivalent. The difference between the Riemann-Liouville derivative (2.28) and the Caputo derivative, (2.29), has been calculated and demonstrated, in [21], as

$$D_*^\alpha f(t) = D_R^\alpha f(t) - \sum_{\nu=0}^{m-1} r_\nu^\alpha(t) f^{(\nu)}(0), \quad \text{where} \quad r_\nu^\alpha(t) = \frac{t^{\nu-\alpha}}{\Gamma(\nu+1-\alpha)}. \tag{2.30}$$

In our study, we consider the case $0 < \alpha < 1$, meaning that from the inequality $m - 1 < \alpha < m$ we get $m = 1$. Thus, by substituting $m = 1$ into (2.30), we get

$$D_*^\alpha f(t) = D_R^\alpha f(t) - r_0^\alpha(t) f(0), \quad \text{where} \quad r_0^\alpha(t) = \frac{t^{-\alpha}}{\Gamma(1-\alpha)}. \tag{2.31}$$

The effect of the correction term, $r_0^\alpha(t) f(0)$, on (2.31) will be discussed in Sect. 3.5, where a numerical integrator will be formulated for Caputo derivatives.

The third and final definition of a FDE is based on finite differences of an equidistant grid (see [21]), and is called the GL derivative. The exact definition of the GL derivative first calls for a notation of finite differences which may be viewed as

$$\frac{1}{h^\alpha} \Delta_h^\alpha f(t) = \frac{1}{h^\alpha} \left(f(\tau_{n+1}) - \sum_{\nu=1}^{n+1} c_\nu^\alpha f(\tau_{n+1-\nu}) \right), \tag{2.32}$$

where

$$c_\nu^\alpha = (-1)^{\nu-1} \binom{\alpha}{\nu}, \tag{2.33}$$

and

$$\binom{\alpha}{\nu} = \frac{\Gamma(\alpha+1)}{\Gamma(\nu+1)\Gamma(\alpha-\nu+1)}. \tag{2.34}$$

This notation allows for the *Grünwald-Letnikov derivative* to be clearly defined as

$$D_R^\alpha f(t) = \lim_{h\to 0} \frac{1}{h^\alpha} \Delta_h^\alpha f(t). \tag{2.35}$$

The GL derivative is introduced as it will prove to be useful in the derivation of a numerical technique to integrate a system composed of FDE (see Sect. 3.5).

2.6 Summary

In this chapter we briefly introduced the notion of a dynamical system and saw that a system's flow describes trajectories of various ICs. The flow is important when comprehending and analysing phenomena associated with a dynamical system. It was then stated in Sect. 2.2 that although a dynamical system can be defined in terms of Euclidean coordinates, this is not always the most efficient or useful method to study the system's evolution. In some cases generalised coordinates are implemented to exhibit a form of mechanics which is more useful than the common Newtonian mechanics, entitled Lagrangian mechanics. However, Lagrangian mechanics still encounters pitfalls, some of which include: the total energy is not utilised and therefore, it is not possible to know whether the energy of the dynamical system is conserved, Lagrangians may contain cyclic coordinates which do not appear in the Lagrangian but their corresponding velocities are experienced, and lastly, Lagrangians make use of a system's generalised coordinates and their associated velocities which means that one would need to solve N (the dimensionality of a system) second order ODEs, which can sometimes lead to challenges. For these reasons, Sect. 2.4 exposed the form of mechanics which will be utilised to construct the systems considered throughout this research, known as Hamiltonian mechanics. Both the evolution of Lagrangian and Hamiltonian systems are defined by integer order ordinary differential equations, yet there are systems which are built on the premise of FDEs and they require their own exposition, which was outlined in Sect. 2.5.

Chapter 3

Numerical techniques

The dynamical systems outlined in Chapt. 2 lay the foundation for certain phenomena to be described mathematically. Understanding the dynamics governed by these systems requires methods which expose the temporal evolution of the flow (2.2). The delineation of a dynamical system's flow is achieved through the integration of the system's eom. Integration can be conducted by either analytical or numerical methods. Systems which are useful for studying models related to physical processes are more often than not portrayed by nonlinear eom. Due to the complexities associated with the nonlinear nature of these equations, analytical solutions are rare to find. Therefore, the implementation of numerical integrators is pertinent in examining a system's flow (some of which are found for example in [22]). This chapter will introduce and compare two numerical methods: a sixth order Runge-Kutta (RK) method and the ABA864 symplectic integrator. In addition we explore relevant integration schemes for dynamical systems described by FDEs. These integration methods will then be used along with numerical techniques that allow us to study phase space structures of dynamical systems. The first procedure that is discussed is the Poincaré Surface of Section (PSS) and secondly, we consider the Lagrangian descriptors (LDs) method. The LDs method is a useful tool that will be implemented throughout this thesis.

3.1 Runge-Kutta methods

The RK methods are robust techniques for solving ODEs, and are widely used throughout the field of nonlinear dynamics. These integration schemes are an extension of the Taylor expansion. However, instead of computing the derivatives of a function, they have various function evaluations from one time step to the next (see for example Chapt. 4 of [23]). Therefore, different RK methods are constructed according to the number of stages and the order of accuracy that they have. The reason that we have chosen to implement a RK integrator, is due to its good accuracy and the ease of implementation compared to other integration schemes. The definition for the RK technique is easily obtained and understood by first observing an introductory numerical integration method called Euler's method. To recount

Euler's method, we shall follow a similar layout to that provided by Chapt. 12 of [24].

Euler's method and RK methods are applicable to first order ODEs of the form

$$\dot{\mathbf{x}} = \mathbf{f}(\mathbf{x}, t), \tag{3.1}$$

and are used to solve initial value problems. This is because the method computes the solution at the next point in time from the current solution. Hence, to iteratively reveal the flow we need a starting point which is the IC. The goal is then to integrate the ODE from the IC $\mathbf{x}(t_0) = \mathbf{x}_0$ to a final point $\mathbf{x}(t_\mathcal{N}) = x_\mathcal{N}$, where $t \in [t_0, t_\mathcal{N}]$. This is done by allowing the time interval to be given as n discrete points (t_n), where $n = 0, 1, \ldots, \mathcal{N}$ and h is the step size from one t value to the next (the points are usually equidistant). Through the discretisation of t, we can rewrite (3.1) as

$$\dot{\mathbf{x}}_n = \mathbf{f}(\mathbf{x}_n, t_n). \tag{3.2}$$

To create an integration method for finding the next position of a dynamical system's flow, $\mathbf{x}(t_n + h) = \mathbf{x}_{n+1}$, in terms of the current value of the flow, $\mathbf{x}(t_n) = \mathbf{x}_n$, one may introduce a Taylor series expansion of $\mathbf{x}(t_n + h)$ about t_n as follows:

$$\mathbf{x}_{n+1} = \mathbf{x}_n + h\mathbf{f}(\mathbf{x}_n, t_n) + \mathcal{O}(h^2). \tag{3.3}$$

Neglecting higher order terms, i.e., the $\mathcal{O}(h^2)$ term, leads to the equation

$$\mathbf{x}_{n+1} = \mathbf{x}_n + h\mathbf{f}(\mathbf{x}_n, t_n), \tag{3.4}$$

which is Euler's method. This approach is an example of a one-step procedure, which means that it expresses the next position of the system's flow, $\mathbf{x}_{n+1}$, in terms of the current value, $\mathbf{x}_n$. Furthermore, a one-step method can be written in the form

$$\mathbf{x}_{n+1} = \mathbf{x}_n + h\Phi(\mathbf{x}_n, t_n; h), \tag{3.5}$$

where Φ is a continuous function of its variables. The shortcoming of Euler's method is that we disregarded the second and higher order terms, i.e., the $\mathcal{O}(h^2)$ term in (3.3), meaning that this approach is only first order accurate. To eradicate this issue, it is necessary to utilise a numerical integrator which has an accuracy of higher order. One such class of numerical integrators is the explicit RK methods. For a comprehensive explanation of the RK methods, the reader is referred to Chapt. 3 of [25]. We shall employ a 6^{th} order RK (RK6) method as it provides an increase in accuracy relative to the commonly used 4^{th} order RK (RK4) method (which is for example presented in Sect. 16.1 of [26]). The technique was described in [27] and can be explicitly written as

$$\mathbf{x}_{n+1} = \mathbf{x}_n + \frac{9\mathbf{k}_1 + 64\mathbf{k}_3 + 49\mathbf{k}_5 + 49\mathbf{k}_6 + 9\mathbf{k}_7}{180}, \tag{3.6}$$

where

$$
\begin{aligned}
\mathbf{k}_1 &= h\mathbf{f}(\mathbf{x}_n, t_n),\\
\mathbf{k}_2 &= h\mathbf{f}(\mathbf{x}_n + \mathbf{k}_1, t_n + h),\\
\mathbf{k}_3 &= h\mathbf{f}\left(\mathbf{x}_n + \frac{3\mathbf{k}_1 + \mathbf{k}_2}{8}, t_n + \frac{h}{2}\right),\\
\mathbf{k}_4 &= h\mathbf{f}\left(\mathbf{x}_n + \frac{8\mathbf{k}_1 + 2\mathbf{k}_2 + 8\mathbf{k}_3}{27}, t_n + \frac{2h}{3}\right),\\
\mathbf{k}_5 &= h\mathbf{f}\Bigg(\mathbf{x}_n + \big[3(3\sqrt{21} - 7)\mathbf{k}_1 - 8(7 - \sqrt{21})\mathbf{k}_2 + 48(7 - \sqrt{21})\mathbf{k}_3\\
&\qquad - 3(21 - \sqrt{21})\mathbf{k}_4\big]/392, t_n + \frac{\left(7 - \sqrt{21}\right)h}{14}\Bigg),\\
\mathbf{k}_6 &= h\mathbf{f}\Bigg(\mathbf{x}_n + \big[-5(231 + 51\sqrt{21})\mathbf{k}_1 - 40(7 + \sqrt{21})\mathbf{k}_2 - 320\sqrt{21}\mathbf{k}_3\\
&\qquad + 3(21 + 121\sqrt{21})\mathbf{k}_4 + 392(6 + \sqrt{21})\mathbf{k}_5\big]/1960, t_n + \frac{(7 + \sqrt{21})h}{14}\Bigg),\\
\mathbf{k}_7 &= h\mathbf{f}\Bigg(\mathbf{x}_n + \big[15(22 + 7\sqrt{21})\mathbf{k}_1 + 120\mathbf{k}_2 + 40(7\sqrt{21} - 5)\mathbf{k}_3 - 63(3\sqrt{21} - 2)\mathbf{k}_4\\
&\qquad - 14(49 + 9\sqrt{21})\mathbf{k}_5 + 70(7 - \sqrt{21})\mathbf{k}_6\big]/180, t_n + h\Bigg).
\end{aligned}
\tag{3.7}
$$

It is important to note that the selection of the parameter h, i.e., the integration time step, can highly impact the accuracy of the numerical integrator. The importance of this choice is because of the inherent continuity and nonlinearity of the studied dynamical systems. Nonlinearity can imply that the flow is highly intricate and complex. Due to the RK method being a one-step method, it is important that the step size is small enough that each step accurately resembles the continuous and complex flow of the dynamical system. Thus, there is an inverse relation between the step size and accuracy of the computation of the system's flow. Additionally, the step size is inversely proportional to the required central processing unit (CPU) runtime. Therefore, there is a natural trade-off between the desired accuracy and the computation costs. At this point, we add that due to the higher order terms being considered, the RK6 method is inherently more accurate than the common 4^{th} order method. Due to the 6^{th} order scheme's improved accuracy, this method can be employed with a larger h value to determine the flow of a dynamical system with a level of accuracy that would require a smaller step size for the 4^{th} order numerical technique.

3.2 Symplectic integrators

Runge-Kutta methods are extremely versatile and applicable to a wide range of ODEs as they are simply applied to a dynamical system's eom. However, these

integration schemes do not take advantage of a specific property of Hamiltonian systems: their symplecticity. Recall that the flow is a mapping which iteratively reveals the solution at t_n. A mapping $\mathbb{M}$ (on a $2N$ dimensional manifold) is said to be symplectic if

$$D\mathbb{M}^T \cdot J_{2N} \cdot D\mathbb{M} = J_{2N}, \tag{3.8}$$

where $D\mathbb{M}$ is the Jacobian matrix of $\mathbb{M}$, T denotes the transpose of a matrix, and J_{2N} is the matrix

$$J_{2N} = \begin{bmatrix} 0_N & \mathbb{I}_N \\ -\mathbb{I}_N & 0_N \end{bmatrix}, \tag{3.9}$$

where $\mathbb{I}_N$ is the $N \times N$ identity matrix and 0_N is the $N \times N$ zero matrix. Runge-Kutta methods do not advantageously utilise the symplectic nature of separable Hamiltonian systems. There are, however, a broad class of integrators that make use of the symplectic nature of Hamiltonian systems called symplectic integrators. In what follows we will reformulate the eom of a Hamiltonian system into a mapping which will be useful in the creation of a symplectic integrator. Then we will use the redeveloped eom to specifically define the symplectic integrator that will be used throughout this study.

Hamiltonian systems satisfy the symplectic condition at all points in phase-space, and consequently preserve the phase space volume, a result known as Louville's theorem (see e.g., [28]). It is possible to utilise this property to create integration schemes which approximate the exact flow to a desired order of accuracy and that are precisely symplectic [28].

Since the introduction of symplectic integrators (by De Vogelaere [29]), multiple symplectic integration schemes have been devised. The interested reader is referred to [30, 31] for some examples of symplectic integrators and their associated efficiency. Here, we shall demonstrate how symplectic integrators are constructed, in a way similar to that shown in the appendix of [32].

As shown in Sect. 2.4, an autonomous Hamiltonian system, $H(q, p)$, with N dof, has the following eom

$$\frac{dq_i}{dt} = \frac{\partial H}{\partial p_i}, \qquad \frac{dp_i}{dt} = -\frac{\partial H}{\partial q_i}. \tag{3.10}$$

where $i = 1, 2, \ldots, N$. However, the eom can be written in an alternate format, using the Poisson bracket. The Poisson bracket of two generic functions, $f(q, p)$ and $g(q, p)$, is defined as

$$\{f, g\} = \sum_{i=1}^{N} \left(\frac{\partial f}{\partial q_i}\frac{\partial g}{\partial p_i} - \frac{\partial f}{\partial p_i}\frac{\partial g}{\partial q_i} \right). \tag{3.11}$$

Implementing the definition of the Poisson bracket, the Hamilton's eom can be re-expressed as

$$\dot{\mathbf{x}} = \{\mathbf{x}, H\} = \sum_{i=1}^{N} \left(\frac{\partial \mathbf{x}}{\partial q_i}\frac{\partial H}{\partial p_i} - \frac{\partial \mathbf{x}}{\partial p_i}\frac{\partial H}{\partial q_i} \right) = L_H \mathbf{x}, \tag{3.12}$$

where L_H is the differential operator defined by $L_H\mathbf{x} = \{\mathbf{x}, H\}$ and $\mathbf{x} = (\mathbf{q}, \mathbf{p})$ is a vector of the generalised positions and the conjugate momenta. The solution to the eom can be formally given as

$$\mathbf{x}(\tau) = e^{\tau L_H}\mathbf{x}_0, \tag{3.13}$$

where $\mathbf{x}_0$ denotes the IC. Provided that the Hamiltonian can be split into two parts, the kinetic energy A (which depends only on the conjugate momenta p_i) and the potential energy B (depending only on the generalised coordinates q_i), the operator $e^{\tau L_H}$ can be rewritten in the following manner

$$e^{\tau L_H} = e^{\tau(L_A + L_B)}. \tag{3.14}$$

To create a symplectic integrator for (3.12) which will propagate the flow from time t to $t + \tau$, requires that one approximates $e^{\tau L_H} = e^{\tau(L_A+L_B)}$ by products of $e^{c_i\tau L_A}$ and $e^{d_i\tau L_B}$, where $i = 1, 2, 3, \ldots, n$. The terms $e^{c_i\tau L_A}$ and $e^{d_i\tau L_B}$ denote exact integrations over times $c_i\tau$ and $d_i\tau$ of the Hamiltonians A and B. These products can be used to iteratively describe the flow of a Hamiltonian system in the following manner

$$\mathbf{x}_{n+1} = \left(\prod_{i=1}^{k} e^{c_i\tau L_A} e^{d_i\tau L_B}\right)\mathbf{x}_n. \tag{3.15}$$

Equation (3.15) is symplectic in nature due to it being a product of symplectic mappings $e^{c_i\tau L_A}$ and $e^{d_i\tau L_B}$ (see e.g., [33]). It is now possible to redefine the eom by implementing the solution for $e^{\tau c_i L_A}\mathbf{x}_n$ as

$$\begin{aligned} \mathbf{q}_{n+1} &= \mathbf{q}_n + \tau c_i \left.\frac{\partial A}{\partial \mathbf{p}}\right|_{\mathbf{p}_n} \\ \mathbf{p}_{n+1} &= \mathbf{p}_n, \end{aligned} \tag{3.16}$$

and the explicit rule for $e^{\tau d_i L_B}\mathbf{x}_n$ is noted by

$$\begin{aligned} \mathbf{q}_{n+1} &= \mathbf{q}_n \\ \mathbf{p}_{n+1} &= \mathbf{p}_n - \tau d_i \left.\frac{\partial B}{\partial \mathbf{q}}\right|_{\mathbf{q}_n}. \end{aligned} \tag{3.17}$$

The symplectic integration method that will be implemented throughout the work to follow, is the ABA864 symplectic integrator first demonstrated in [34]. The reason that this integrator is selected is attributed to its increased level of accuracy coupled with the method's computational performance, which have been demonstrated in [30, 31]. The ABA864 integrator is mathematically seen as

$$\begin{aligned} \text{ABA864} =& e^{a_1\tau L_A} e^{b_1\tau L_B} e^{a_2\tau L_A} e^{b_2\tau L_B} e^{a_3\tau L_A} e^{b_3\tau L_B} e^{a_4\tau L_A} e^{b_4\tau L_B} e^{a_4\tau L_A} \\ & e^{b_3\tau L_B} e^{a_3\tau L_A} e^{b_2\tau L_B} e^{a_2\tau L_A} e^{b_1\tau L_B} e^{a_1\tau L_A}, \end{aligned} \tag{3.18}$$

where the involved constants can be found in Table 3.1.

Constant	Value
a_1	0.071133426498223117777938730006154996417 4
a_2	0.241153427956640098736487795326289649618
a_3	0.521411761772814789212136078067994229991
a_4	-0.333698616227678005726562603400438876027
b_1	0.183083687472197221961703757166430291072
b_2	0.310782859898574869507522291054262796375
b_3	-0.026564618511958800697212137916498759266 3
b_4	0.065396142282373418455972179391113436371 0

Table 3.1: The constants for the ABA864 symplectic integrator as shown in [34].

3.3 Comparison of the methods

To implement and compare the RK6 (3.6) and ABA864 integrators (3.18), we consider a simple Hamiltonian system. We are then able to integrate various orbits from this system and compare the energy error produced by each integration method. Additionally, we can observe each integrator's required computational time to reveal the trajectory over a time interval. The system of choice is the Hénon-Heiles Hamiltonian system, as it is a dynamically rich system which is often used to authenticate new numerical methods, see e.g., [35, 36, 37].

The Hénon-Heiles Hamiltonian was first presented in [38]. This paper was written with the purpose of showcasing that a third integral of motion exists and is isolating. An integral of motion is a function of the coordinates that remains constant throughout the evolution of a dynamical system in phase space. This integral is isolating if it restricts the motion of orbits to a hyper-surface of dimensionality one less than the phase space, and each additional isolating integral of motion further reduces the dimensionality of the surface by one. On the other hand, a non-isolating integral is one where the integral adds no additional information as it does not uniquely determine a system's path. Therefore, a non-isolating integral of motion is of no importance analytically. It was previously assumed that a third integral of motion was non-isolating as no analytical solutions were found, for example see papers such as [39, 40, 41, 42]. However, some orbits in Hamiltonian models of galaxies were computed numerically in [43, 44], where it was demonstrated that behaviours were nonconforming to this past belief. This led Hénon and Heiles to attempt to numerically demonstrate that the third integral was indeed isolating. They found that the third isolating integral of motion exists for a limited range of ICs.

The Hénon-Heiles Hamiltonian is written as follows:

$$H = \frac{1}{2}(p_x^2 + p_y^2) + \frac{1}{2}(x^2 + y^2) + x^2 y - \frac{1}{3}y^3, \tag{3.19}$$

where x and y are positions in configuration space, while p_x and p_y are the corresponding conjugate momenta. The Hamiltonian eom for this system are found by

applying (3.10), and are written as

$$\begin{aligned} \dot{x} &= p_x, \\ \dot{y} &= p_y, \\ \dot{p_x} &= -x - 2xy, \\ \dot{p_y} &= -y - x^2 + y^2. \end{aligned} \tag{3.20}$$

As the eom for this dynamical system have been expressed in (3.20), the RK6 method (3.6) can be simply implemented together with ICs to determine and examine the flow. On the other hand, the utilisation of the ABA864 integrator (3.18) requires that the functional forms of the kinetic and potential energies of the Hamiltonian system are first defined. The functional forms can be found because the Hénon-Heiles Hamiltonian can be split into its kinetic energy A and potential energy B, in the following way

$$A = \frac{1}{2}\left(p_x^2 + p_y^2\right), \qquad B = \frac{1}{2}(x^2 + y^2) + x^2 y - \frac{1}{3}y^3. \tag{3.21}$$

The eom of A are then expressed using the explicit rule $e^{\tau c_i L_A}\mathbf{z}(t_n)$ [where $\mathbf{z}(t_n) = (x(t_n), y(t_n), p_x(t_n), p_y(t_n))$] as

$$\begin{aligned} x(t_{n+1}) &= x(t_n) + \tau c_i p_x(t_n), \\ y(t_{n+1}) &= y(t_n) + \tau c_i p_y(t_n), \\ p_x(t_{n+1}) &= p_x(t_n), \\ p_y(t_{n+1}) &= p_y(t_n), \end{aligned} \tag{3.22}$$

and the evolution of B is found using the solution of $e^{\tau d_i L_B}\mathbf{z}(t_n)$ as

$$\begin{aligned} x(t_{n+1}) &= x(t_n), \\ y(t_{n+1}) &= y(t_n), \\ p_x(t_{n+1}) &= p_x(t_n) - \tau d_i[x(t_n) + 2x(t_n)y(t_n)], \\ p_y(t_{n+1}) &= p_y(t_n) - \tau d_i[y(t_n) + x^2(t_n) - y^2(t_n)]. \end{aligned} \tag{3.23}$$

It is now wise to compare the integration schemes in terms of their accuracy and the computational time required to achieve a certain level of accuracy. One way of quantifying the accuracy of integration schemes is through their ability to conserve the dynamical system's energy H. Due to this Hamiltonian system being autonomous, we can use the conservation of energy property [as discussed after (2.26)]. The reason that we use this feature is because it holds true throughout the entire evolution of the dynamical system. Therefore, the comparison will take place by integrating various ICs and observing the deviation of the current computed energy from the initial energy. The energy is calculated at each time step by means of the Hénon-Heiles Hamiltonian (3.19). Thus, the difference between the initial energy and the energy at time t is quantified through the relative energy error

$$E_r(t) = \left| \frac{H(q_i(t), p_i(t)) - H(q_i(0), p_i(0))}{H(q_i(0), p_i(0))} \right|, \tag{3.24}$$

where q_i are the generalised coordinates of a dynamical system and p_i are the conjugate momenta, $H(q_i(0), p_i(0))$ is the initial energy of the system and $H(q_i(t), p_i(t))$ is the energy calculated at each time t along the system's evolution. To ensure that the energy is appropriately conserved requires that the relative energy error falls within some tolerance. For the Hénon-Heiles system, we determined that the appropriate tolerance level is $\log_{10}(E_r(t)) < -8$ until our final integration time of $t = 2000$. Furthermore, an energy level of $H(q_i(0), p_i(0)) = \frac{1}{8}$ is used to conduct the examination of the performance of the RK6 and ABA864 integrators. It should, however, be mentioned that multiple energy values have been tested and similar behaviours are exhibited for all relevant energy levels. The Hénon-Heiles system contains some regions in phase space which display regular dynamics and some regions which display chaotic motion. Chaotic motion means that a deterministic orbit has sensitive dependence on its IC, while regular motion does not. Additionally, the maximum Lyapunov exponent (see e.g., [45] and references therein) of a trajectory with regular motion is zero, and the maximum Lyapunov exponent of a chaotic orbit is positive. Thus, an in-depth analysis of our two numerical integrators requires that we integrate ICs from each of the two dynamical regimes. However, we showcase the results of only one chaotic and one regular IC as all results were similar. The IC of the considered chaotic orbit is

$$x = 0, \quad y = -0.1, \quad p_y = 0.2, \tag{3.25}$$

where the momentum $p_x > 0$ is calculated using (3.19) to ensure that the IC satisfies the chosen energy level. The IC pertaining to a regular orbit is given as

$$x = 0, \quad y = 0.3, \quad p_y = 0.01. \tag{3.26}$$

By requiring that $\log_{10}(E_r(t)) < -8$ over the interval $t \in [0, 2000]$, we are able to determine an appropriate time step, h, for each integration method. The ABA864 integrator required a step size of $h = 0.079$ and the RK6 method called for a step size of $h = 0.048$. The results are displayed in Fig. 3.1, wherein the panels (a) and (c) present the $\log_{10}(E_r(t))$ curve from one time step to the next over the time interval $t \in [0, 2000]$ for the ABA864 integrator, while panels (b) and (d) exhibit similar results but for the RK6 method. Additionally, the findings pertaining to the chaotic orbit are seen in (a) and (b), whereas the results for the regular orbit are showcased in (c) and (d). In Fig. 3.1, all plots contain a horizontal orange line at $\log_{10}(E_r(t)) = -8$. This line represents the maximum relative energy error required for the energy of this dynamical system to be considered sufficiently conserved.

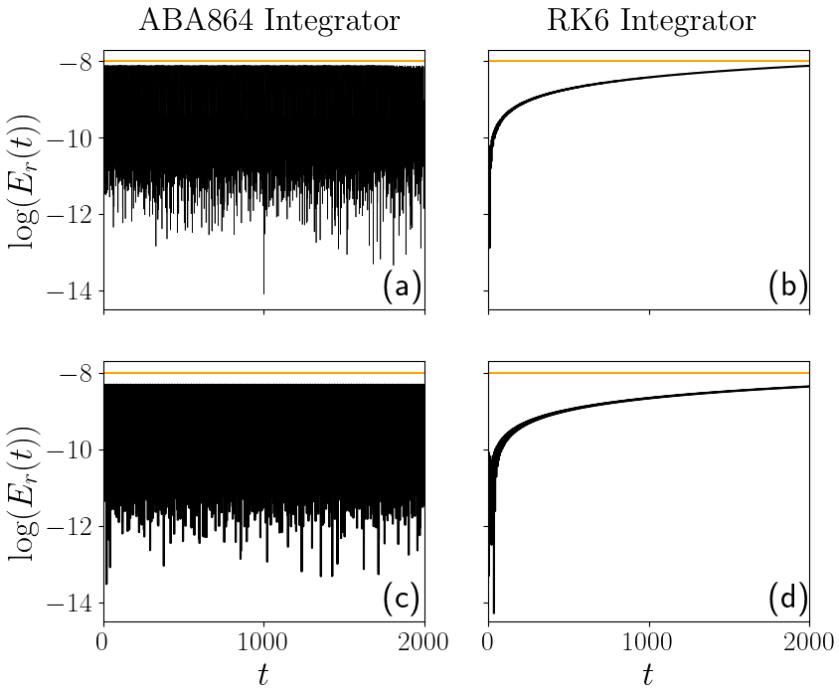

Figure 3.1: Relative energy error (3.24) for the integration of two orbits of the Hénon-Heiles Hamiltonian (3.19). Both trajectories are integrated using the ABA864 integrator (3.18) [presented in panels (a) and (c)] and the RK6 method (3.6) [plots (b) and (d)]. The integration schemes used step sizes of $h = 0.079$ and $h = 0.048$, respectively. These h values were selected to ensure that $\log_{10}(E_r(t))$ is closely below a level of -8 (displayed as orange lines in all panels). Additionally, panels (a) and (b) depict the results of the chaotic orbit with an IC (3.25) and panels (c) and (d) show the results for a regular orbit with an IC (3.26).

From Fig. 3.1 we can see that the energy error curves (shown in black) of the ABA864 method [Fig. 3.1(a) and Fig. 3.1(c)] are asymptotically bounded, whereas the RK6 [Fig. 3.1(b) and Fig. 3.1(d)] integrator's relative energy error tends to gradually increase over time. This bounded property is attributed to the ABA864 method's utilisation of the symplectic property for autonomous Hamiltonian systems, as mentioned in Sect. 3.2. In contrast, the RK6 scheme does not incorporate this property and, therefore, its relative energy error worsens as t increases. A consequence of the decline in accuracy experienced by the RK6 integrator, is the need for smaller h values for longer integration periods. This requirement is to ensure the energy of the system is conserved within the required tolerance level. A direct repercussion for decreasing the value of h, is an increase in the required CPU time. In contrast, we can find an acceptable h value for the ABA864 integrator over a short period of time and this value typically ensures that the conservation property is preserved over any arbitrary integration interval. Additionally, we note the CPU time taken for obtaining the results of Fig. 3.1(a) and Fig. 3.1(c) is 1.174 seconds and 1.163 seconds, respectively, in a Dell Inspiron 15 7510 with an Intel

Core i7 processor. Furthermore, the CPU time required to find $E_r(t)$ for panels (b) and (d) of Fig. 3.1 is respectively given as 3.609 seconds and 3.591 seconds. These times reinforce the fact that the ABA864 integration scheme not only bounds the energy error but also that it is computationally faster than the RK6 method for this dynamical system at this tolerance level over long integration times. Thus, a symplectic integrator is preferred over a RK integrator for autonomous Hamiltonian systems as the accuracy of the integration is bounded and the required CPU time is less due to smaller step sizes.

3.4 Poincaré surface of section

As we now have defined two methods of numerical integration, we can plot the flow of various trajectories from a large assortment of dynamical systems. However, many systems have a phase space which is greater than three dimensions. This becomes a problem when attempting to visualise various trajectories of a system or structures found within the phase space. Thus, we present the PSS. A PSS is a way of presenting a trajectory in phase space of an autonomous Hamiltonian system, in a $2N-2$ dimensional space. The motion of such a dynamical system is restricted to a $2N-1$ energy hypersurface (see e.g., Chapt. 14 of [46]), as the energy of an autonoumous Hamiltonian system is constant (2.26). This reduction takes place by expressing one variable from the system in terms of the remaining $2N-1$ variables and the value of the energy. From this $2N-1$ dimensional space, we are able to plot the points on the $2N-2$ dimensional PSS by selecting a space such that one of the variables is constant.

To numerically create a PSS, we begin with a grid of ICs in a $2N-2$ dimensional subspace of the phase space. We then integrate the orbits associated with all ICs and plot the points of intersection of the generated orbit with this subspace. However, numerically finding the intersections is not a straightforward process as our numerical integrators use a discrete time step. Without loss of generality we choose a PSS such that one of the generalised coordinates is constant, i.e., $q_i(t) = C$, where C is some constant value and $q_i(t)$ is a generalised coordinate from some autonomous Hamiltonian system. Then having a fixed h value for our integrator means that an orbit from the system may experience consecutive integration steps (t_n and t_{n+1}) such that $q_i(t_n) < C < q_i(t_{n+1})$. Due to the continuity of the trajectory, the intermediate value theorem (see e.g., Chapt. 2 of [47]) states that for some $t \in (t_n, t_{n+1})$ the orbit will intersect the PSS. To find the exact point of intersection, we use the procedure described in [48]. That is, we begin at the point $q_i(t_n)$ and integrate the Hamiltonian system with respect to $q_i(t)$ (instead of the usual t) for an integration step of $C - q_i(t_n)$. This process ensures that after one step, the point will lie exactly

on the PSS. To integrate with respect to $q_i(t)$, we cannot integrate the usual eom

$$\begin{aligned}
\frac{dq_1}{dt} &= f_1(q_1, \ldots, q_N, p_1, \ldots, p_N), \\
&\vdots \\
\frac{dq_N}{dt} &= f_N(q_1, \ldots, q_N, p_1, \ldots, p_N), \\
\frac{dp_1}{dt} &= f_{N+1}(q_1, \ldots, q_N, p_1, \ldots, p_N), \\
&\vdots \\
\frac{dp_N}{dt} &= f_{2N}(q_1, \ldots, q_N, p_1, \ldots, p_N).
\end{aligned} \tag{3.27}$$

Instead we have to integrate the following system of differential equations

$$\begin{aligned}
\frac{dq_1}{dq_i} &= \frac{f_1}{f_i}, \\
&\vdots \\
\frac{dq_N}{dq_i} &= \frac{f_N}{f_i}, \\
\frac{dp_1}{dq_i} &= \frac{f_{N+1}}{f_i}, \\
&\vdots \\
\frac{dp_N}{dq_i} &= \frac{f_{2N}}{f_i},
\end{aligned} \tag{3.28}$$

for some $i \in \{1, \ldots, N\}$. This method is highly accurate and computationally inexpensive when compared to root finding methods such as the bisection method.

We now use the Hénon-Heiles system (3.19) to present an example of a PSS and this method's ability to showcase phase space structures. The PSS is constructed such that $x = 0$ and $p_x > 0$, as to exhibit a 2D slice of the dynamical system's phase space. Additionally, we select two different energy values ($H = \frac{1}{8}$ and $H = \frac{1}{12}$) to demonstrate the method's ability to reveal various structures. The results are presented in Fig. 3.2(a) and Fig. 3.2(b) respectively. Each PSS is created by integrating 400 evenly spaced ICs for an integration time of $t = 5000$. The ICs for Fig. 3.2(a) are selected over the intervals $y \in [-0.45, 0.65]$ and $p_y \in [-0.55, 0.55]$ and for Fig. 3.2(b) the equidistant grid of ICs is over the intervals $y \in [-0.4, 0.55]$ and $p_y \in [-0.45, 0.45]$. In these plots, two kinds of dynamical regimes are seen. The first consists of regular regions and are seen as more cohesive structures [all curves in Fig. 3.2(b)]. The next corresponds to chaotic regions, which are seen as points that appear to be randomly distributed and are only evident in Fig. 3.2(a).

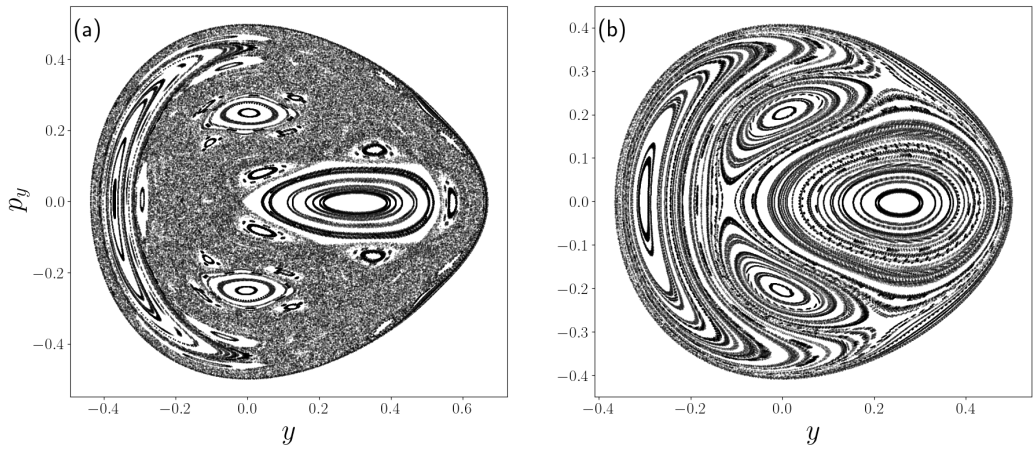

Figure 3.2: The PSS with $x = 0$ and $p_x > 0$, for the Hénon-Heiles system (3.19) with an energy of (a) $H = \frac{1}{8}$ and (b) $H = \frac{1}{12}$. Plots are constructed by selecting an equidistant grid of 20×20 ICs from the interval (a) $y \in [-0.45, 0.65]$ and $p_y \in [-0.55, 0.55]$, as well as (b) $y \in [-0.4, 0.55]$ and $p_y \in [-0.45, 0.45]$. Each IC is integrated for a time of $t = 5000$, using the ABA864 method (3.18) and the intersections are found using the method of Hénon [48] with the RK6 scheme (3.6).

3.5 Integration methods for dynamical systems described by fractional order differential equations

In Sect. 2.5 we indicated that, in addition to dynamical systems governed by ODEs, there exist systems described by FDEs. Unlike the usual dynamical systems whose flow at time $t+h$ is found using the current state (at time t), an FDE's flow at time $t+h$ is found using all past states [as seen by the integrals in (2.28) and (2.29), as well as the summation term in (2.32)]. Therefore, the integration procedures outlined in Sect. 3.1 and Sect. 3.2 bare no use for dynamical systems comprised of FDEs. Thus, we require an introduction of new integration methods. Similarly to integrators for ODEs, there are a multitude of numerical integrators that may be implemented for FDEs (some of which are discussed in [2, 49]). The specific integration method that will be used in this thesis, is the so-called GL approximation. This scheme is described below in a similar manner to that demonstrated in [21].

The reason that this integrator was chosen is due to its reliable nature for solving Caputo derivatives (2.29), with $0 < \alpha < 1$. We consider FDEs of the form

$$D_*^\alpha y(t) = f(y(t)), \tag{3.29}$$

where $D_*^\alpha y(t)$ is the Caputo derivative of order α with respect to the function $y(t)$ [as seen in (2.29)], t is the independent variable for time and $f(y(t))$ is a function describing how the rate of change of $y(t)$ depends on its value at time t. As was the case for the RK6 and ABA864 methods, respectively discussed in Sect. 3.1 and

Sect. 3.2, this integration scheme needs an IC $y(\tau_0) = y_0$. Additionally, it may be postulated that there exists a solution $y = y(\tau)$ over the interval $[0, t]$. Calculating the flow of this FDE system, numerically, requires the time interval to be considered in a discretised format. The discretisation may be implemented through partitioning the time interval as follows

$$0 = \tau_0 < \tau_1 < \cdots < \tau_n < \tau_{n+1} = t, \tag{3.30}$$

where $\tau_{k+1} - \tau_k = h$ $(k = 0, 1, \ldots, n)$ is the step size between the equidistant time instances. Additionally, we have the numerical approximation y_k of the actual solution $y(\tau_k)$ at each point in time. One may then apply the GL approximation (2.32) and the correction term, outlined in (2.31), to (3.29) with respect to $\tau_{n+1} = (n + 1)h$. The right-hand side of (3.29) may then be approximated by $f(y_n)$ or $f(y_{n+1})$, which leads, respectively, to the definitions of the explicit GL method

$$y_{n+1} - \sum_{\nu=1}^{n+1} c_\nu^\alpha y_{n+1-\nu} - r_{n+1}^\alpha y_0 = h^\alpha f(y_n), \tag{3.31}$$

or the implicit GL method

$$y_{n+1} - \sum_{\nu=1}^{n+1} c_\nu^\alpha y_{n+1-\nu} - r_{n+1}^\alpha y_0 = h^\alpha f(y_{n+1}), \tag{3.32}$$

where

$$\begin{aligned} r_{n+1}^\alpha &= h^\alpha r_0^\alpha(\tau_{n+1}) = \gamma_{0,-1}^\alpha (n+1)^{-\alpha}, \\ \gamma_{\mu,j}^\alpha &= \frac{\Gamma(\mu\alpha + 1)}{\Gamma(j\alpha + 1)}, \qquad \mu, j \in \mathbb{N}_0 \cup \{-1\}, \end{aligned} \tag{3.33}$$

and,

$$c_\nu^\alpha = \left(1 - \frac{\alpha + 1}{\nu}\right) c_{\nu-1}^\alpha, \qquad c_1^\alpha = \alpha. \tag{3.34}$$

It is crucial to note that $r_{n+1}^\alpha y_0 \to 0$ as $n \to \infty$ and that $r_{n+1}^\alpha y_0 = 0$ if the IC is zero.

3.5.1 Application of the Grünwald-Letnikov method

To demonstrate the utility and accuracy of the explicit and implicit GL methods, we conduct a basic numerical investigation. Here, we juxtapose the explicit and implicit GL methods with the actual solution (calculated through the implementation of the one-parameter Mittag-Leffler function) of a simple FDE which can be obtained analytically. First, an introduction is made for the tool which will allow the true solution to be explicitly stated, the one-parameter Mittag-Leffler function.

The one-parameter Mittag-Leffler function is closely related to a function which is useful for describing solutions of ODEs, the exponential function e^z, where $z \in \mathbb{C}$.

For this reason, the function introduced by Mittag-Leffler [50] has found use in expressing analytical solutions of FDEs (see for example [51, 52, 53]). This function has been described in [19] and is given by

$$E_\alpha(z) = \sum_{k=0}^{\infty} \frac{z^k}{\Gamma(k\alpha + 1)}, \tag{3.35}$$

and can be easily reverted to the exponential function by setting $\alpha = 1$, as follows

$$E_1(z) = \sum_{k=0}^{\infty} \frac{z^k}{\Gamma(k+1)} = \sum_{k=0}^{\infty} \frac{z^k}{k!} = e^z. \tag{3.36}$$

The impact of $E_\alpha(z)$ is easily showcased by introducing a simple FDE, which will allow for the comparison of the two numerical integrators, as

$$D_*^\alpha y(t) = \lambda y(t), \qquad y(0) = y_0. \tag{3.37}$$

The analytical solution is elucidated by incorporating (3.35) in the following manner

$$y(t) = y_0 E_\alpha(\lambda t^\alpha) = y_0 \sum_{\nu=0}^{\infty} \gamma_{0,\nu}^\alpha (\lambda t^\alpha)^\nu, \tag{3.38}$$

where

$$\gamma_{0,\nu}^\alpha = \frac{\Gamma(1)}{\Gamma(\nu\alpha + 1)} = \frac{1}{\Gamma(\nu\alpha + 1)}, \qquad \nu \in \mathbb{N}_0 \cup \{-1\}. \tag{3.39}$$

In terms of the numerical solutions, both explicit and implicit GL methods are applied to the FDE (3.37). The explicit method (3.31) is applied to this FDE through the following steps:

$$\begin{aligned}
&y_{n+1} - \sum_{\nu=1}^{n+1} c_\nu^\alpha y_{n+1-\nu} - r_{n+1}^\alpha y_0 = h^\alpha f(y_n) \Rightarrow \\
&y_{n+1} - c_1^\alpha y_n - \sum_{\nu=2}^{n+1} c_\nu^\alpha y_{n+1-\nu} - r_{n+1}^\alpha y_0 = h^\alpha (\lambda y_n) \Rightarrow \\
&y_{n+1} - \alpha y_n - \sum_{\nu=2}^{n+1} c_\nu^\alpha y_{n+1-\nu} - r_{n+1}^\alpha y_0 = \lambda h^\alpha y_n \Rightarrow \\
&y_{n+1} = (\alpha + \lambda h^\alpha) y_n + \sum_{\nu=2}^{n+1} c_\nu^\alpha y_{n+1-\nu} + r_{n+1}^\alpha y_0.
\end{aligned} \tag{3.40}$$

The implicit method (3.32) is found through the ensuing procedure

$$
\begin{aligned}
y_{n+1} - \sum_{\nu=1}^{n+1} c_\nu^\alpha y_{n+1-\nu} - r_{n+1}^\alpha y_0 &= h^\alpha f(y_{n+1}) \Rightarrow \\
y_{n+1} - \sum_{\nu=1}^{n+1} c_\nu^\alpha y_{n+1-\nu} - r_{n+1}^\alpha y_0 &= h^\alpha (\lambda y_{n+1}) \Rightarrow \\
y_{n+1} - \lambda h^\alpha y_{n+1} &= \sum_{\nu=1}^{n+1} c_\nu^\alpha y_{n+1-\nu} + r_{n+1}^\alpha y_0 \Rightarrow \\
(1 - \lambda h^\alpha) y_{n+1} &= \sum_{\nu=1}^{n+1} c_\nu^\alpha y_{n+1-\nu} + r_{n+1}^\alpha y_0 \Rightarrow \\
y_{n+1} &= \frac{1}{(1 - \lambda h^\alpha)} \sum_{\nu=1}^{n+1} c_\nu^\alpha y_{n+1-\nu} + r_{n+1}^\alpha y_0.
\end{aligned} \tag{3.41}
$$

As we now have an analytical and two numerical representations for the FDE solution, we can compare the results obtained from each integrator. In order to conduct such an exploration we compare the analytical solution to the two numerical approaches for various values of h. The different step sizes are used in the methods to present the accuracy of each approximation. This investigation will be conducted using the same α values as shown in [21], $\alpha = 0.5$ and $\alpha = 0.8$, to validate the implementation of our code. Additionally, we use $\lambda = -4$ and the IC is set to $y_0 = 0.5$. We examined multiple ICs over the interval $[-10^{10}, 10^{10}]$ and found that the GL method appropriately approximates the true solution. Furthermore, it is important to note that the upper bound of ∞ in the summation of the Mittag-Leffler function (3.35) is impossible to implement numerically. However, we can accurately approximate the summation due to

$$
\gamma_{0,\nu}^\alpha (\lambda t^\alpha)^\nu \to 0 \qquad \text{as} \qquad \nu \to \infty. \tag{3.42}
$$

To show that this is true, we begin by rewriting (3.42) using (3.39) with $\lambda = -4$, which leads to

$$
\gamma_{0,\nu}^\alpha (-4t^\alpha)^\nu = \frac{1}{\Gamma(\alpha\nu + 1)} (-4t^\alpha)^\nu . \tag{3.43}
$$

Before continuing with this derivation, we note that the asymptotic approximation of the gamma function can be given using Stirling's approximation (see e.g., [54]), which is seen as

$$
\Gamma(x) \sim \sqrt{2\pi} x^{x-0.5} e^{-x}, \tag{3.44}
$$

where the notation $f(x) \sim g(x)$ indicates that $\frac{f(x)}{g(x)} \to 1$ as $x \to \infty$. We are then able to rewrite (3.43) using (3.44), as

$$\begin{aligned}\frac{(-4t^\alpha)^\nu}{\Gamma(\alpha\nu+1)} &\sim (-4t^\alpha)^\nu \Big/ \left(\sqrt{2\pi}(\alpha\nu+1)^{\alpha\nu+1-0.5}e^{-\alpha\nu-1}\right) \\ &= (-4t^\alpha)^\nu \Big/ \left(\frac{\sqrt{2\pi(\alpha\nu+1)}}{e}\frac{(\alpha\nu+1)^{\alpha\nu}}{e^{\alpha\nu}}\right) \\ &= \frac{e}{\sqrt{2\pi(\alpha\nu+1)}}\left(\frac{-4t^\alpha e^\alpha}{(\alpha\nu+1)^\alpha}\right)^\nu. \end{aligned} \tag{3.45}$$

Provided that t is finite, we see that both factors on the right hand side of (3.45) tend to zero as $\nu \to \infty$. Therefore, if the value of t is finite, we have that

$$\lim_{\nu\to\infty} \gamma^\alpha_{0,\nu}(-4t^\alpha)^\nu = 0. \tag{3.46}$$

As the convergence has been shown, it is possible to select a finite ν value which leads to $\gamma^\alpha_{0,\nu}(\lambda t^\alpha)^\nu \approx 0$ for $\alpha = 0.8$ and $\alpha = 0.5$. This convergence ensures that the analytical solution is sufficiently accurate. The finite value that we have selected is $\nu = 200$. To demonstrate that $\nu = 200$ is sufficient for our comparison of the integration schemes, over an interval of $t \in [0, 1]$, we calculated the value of $\gamma^\alpha_{0,\nu}(\lambda t^\alpha)^\nu$ for both α values and for $t = 1$. The results are displayed in Table 3.2.

$\boldsymbol{\alpha}$	$\boldsymbol{t}$	$\boldsymbol{\gamma^\alpha_{0,\nu}(\lambda t^\alpha)^\nu}$
0.8	1	-7.94×10^{-164}
0.5	1	-6.93×10^{-38}

Table 3.2: Computation of $\gamma^\alpha_{0,\nu}(\lambda t^\alpha)^\nu$ (3.39) using $\nu = 200$, $\lambda = -4$, and the values shown in columns one and two of this table (α and t).

In Table 3.2 we demonstrate that a smaller α value results in a slower convergence rate of $\gamma^\alpha_{0,\nu}(\lambda t^\alpha)^\nu$. Regardless, $\nu = 200$ results in sufficient convergence and therefore, the analytical solution (3.38) for both α values is accurately approximated. Furthermore, this table reveals the existence of an inverse relation between the value of α and the required value of ν. To numerically approximate the true solution when the α is small, a large ν is required.

Having established the accuracy of the selected upper bound ($\nu = 200$) for $\alpha = 0.5$ and $\alpha = 0.8$ over the interval $t \in [0, 1]$, a thorough comparison between the true solution (shown as a dashed blue curve in Fig. 3.3) and the numerical approximations (indicated by orange curves in Fig. 3.3) can now be conducted. The two columns on the left of Fig. 3.3 [panels (a), (b), (e), (f), (i), (j), (m), (n)] consist of results pertaining to the explicit method (3.40) versus the true solution. The two columns on the right of Fig. 3.3 [panels (c), (d), (g), (h), (k), (l), (o), (p)] showcase the implicit method (3.41) versus the true solution. The different rows of Fig. 3.3 pertain to different values of h. From the top to the bottom row, the step

sizes are $h = 0.1$, $h = 0.05$, $h = 0.01$, and $h = 0.001$, respectively. Additionally, two different values of α have been used, $\alpha = 0.8$ (first and third columns) and $\alpha = 0.5$ (second and fourth columns), to ensure that the impact of the h values are completely understood.

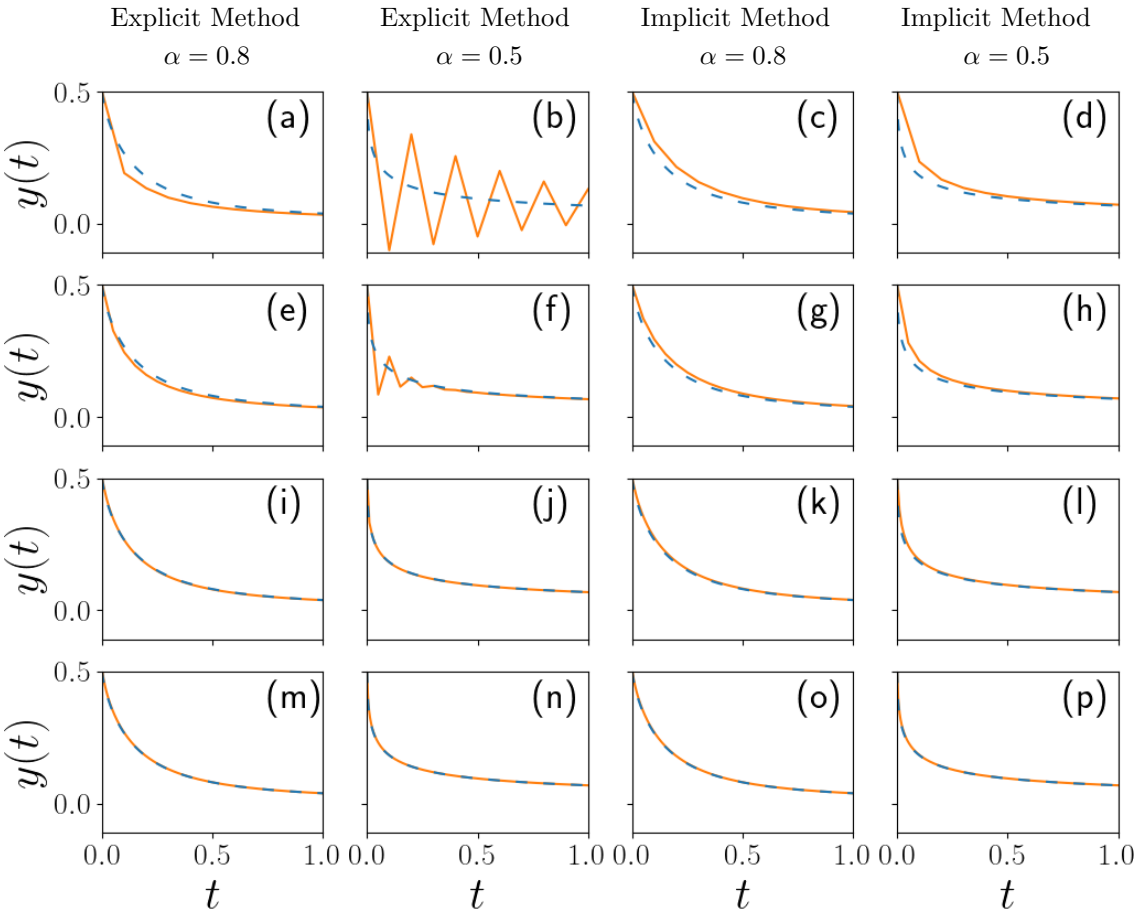

Figure 3.3: Solutions of a simple FDE (3.37) using the analytical result (3.38) presented as the blue dashed curves, as well as the explicit (3.40) and implicit (3.41) GL methods shown as the orange curves. The explicit method is used to produce the orange curves in the first two columns of panels and the last two columns relate to the implicit method. Two different α values are used for the FDE, $\alpha = 0.8$ [panels (a), (c), (e), (g), (i), (k), (m) and (o)] and $\alpha = 0.5$ [panels (b), (d), (f), (h), (j), (l), (n) and (p)]. Additionally, the GL methods make use of four different time step values, $h = 0.1,\ 0.05,\ 0.01$ and 0.001. In the top row, panels (a) to (d) utilise the largest h value. Each following row incorporates a different h value in decreasing order.

Through the observation of Fig. 3.3, the following differences between the explicit and implicit GL methods are seen: when the step size is unreasonably large, $h = 0.1$ in Figs. 3.3(a)–(d), the implicit method performs better than the explicit method but both methods are rather inaccurate. When the step size is reduced but still quite large, $h = 0.05$ in panels (e) to (h), the explicit method for $\alpha = 0.8$ is slightly better

at approximating the true solution. However, for the smaller α value ($\alpha = 0.5$), the explicit method does not accurately represent the true solution over the first half of the time interval. Furthermore, results at the second half of the considered interval indicate that the explicit method does a better job at reproducing the true solution compared to the implicit method. As we decrease the step size further to $h = 0.01$ presented in Figs. 3.3(i)–(l), we see that the GL method (represented by the orange curves) better approximates the true solution (seen as the dashed blue curves), compared to the larger h values [displayed in Figs. 3.3(a)–(h)]. In addition, we see that the orange curves of the implicit method [presented in Figs. 3.3(k) and (l)] do not perfectly match the evolution of the true solution, while the dashed blue curve of the true solution lies approximately on top of the orange curve representing the explicit method [Figs. 3.3 (i) and (j)]. Figures 3.3(m)–(p) show that a time step of $h = 0.001$ provides improved precision for both the implicit and explicit GL methods, to the point where they are nearly faultless. The conclusion from Fig. 3.3, is that the explicit method is less accurate for large step sizes (e.g., $h = 0.1$ and $h = 0.05$) but is more precise for appropriately selected small h values [as seen in Figs. 3.3(i) to (p)]. Thus, the explicit GL method will be utilised for all FDEs (with some constraints that are discussed in Sect. 3.5.3) and systems which comprised of such equations for the remainder of this study.

3.5.2 Backward integration

Backward in time integration methods for ODEs simply require the forward integration method to employ a negative time step, $-h$ ($h > 0$), to integrate over the interval from time 0 to $-t$. Using a negative time step in the RK6 (3.6) results in $\mathbf{k}_i$, $i = 1, 2, \ldots, 7$ being equivalent to changing the sign of $\mathbf{f}(\mathbf{x}, t)$ from the eom (2.1) and implementing a positive h value. By applying a negative time step to the ABA864 integration scheme (3.18), we also find that it is equivalent to considering a positive h value together with a negated function value, $-\mathbf{f}(\mathbf{x}, t)$ in the eom. This equivalence implies that a backward temporal evolution can be found in two ways: either by employing an integration method with a negative h value, or by using a positive time step and the eom with a change of sign. We qualitatively demonstrate this point by employing the RK6 method, (3.6), to the Hénon-Heiles Hamiltonian's eom (3.20), in two different ways. In the first approach the integrator is implemented is the usual way; that is to simply use a negative time step to reveal an orbit's backward temporal evolution from time 0 to $-t$, where $t > 0$. The second method is to negate the value of the function $\mathbf{f}(\mathbf{x}, t)$ in the eom and use a positive h value over the interval $[0, t]$. To demonstrate that these two methods are equivalent, we integrate 10 randomly selected ICs of the Hénon-Heiles system at $H = \frac{1}{8}$, (3.19), (which will be labeled 1–10 on the results). We compute the backward temporal evolution for $t = 50$ and $h = 0.048$. To determine that the trajectories are equivalent, we show the backward temporal evolution of the orbits in the y dimension. The results for the orbits with a negative time step and positive eom are shown in Fig. 3.4(a) and for a positive time step with negative eom in Fig. 3.4(b). To demonstrate that the

two methods of backward integration are identical, we find at every time step the phase space distance between the trajectory calculated using the first method and the second method and report the results in Fig. 3.4(c). The distance is calculated as the L_2 norm of the difference between the state vectors from each orbit at each time step.

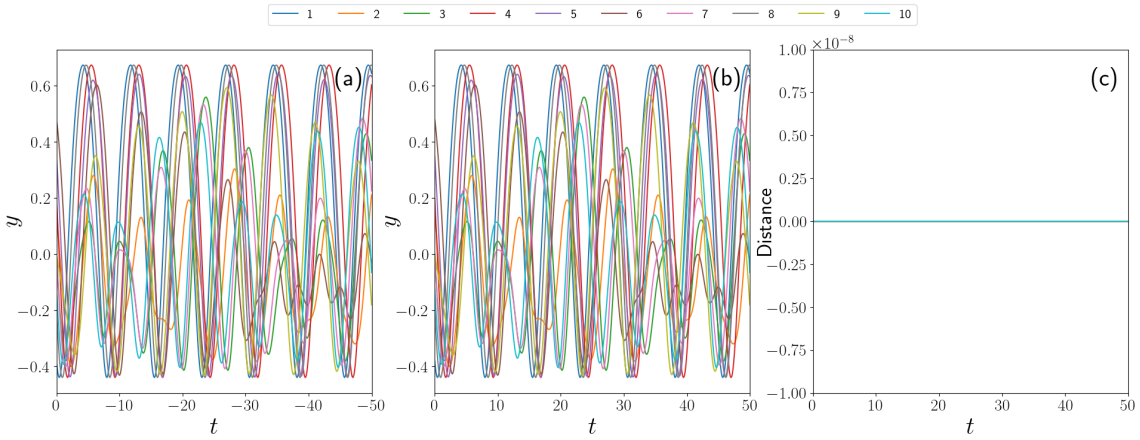

Figure 3.4: Backward temporal evolution of the y-coordinate of 10 randomly chosen orbits of the Hénon-Heiles Hamiltonian (3.19). Panel (a) presents the backward integration of the orbits using the ABA864 method (3.18) and a negative time step, whereas for the results of panel (b) we use a positive h value and change the sign of the eom by multiplying with -1. Finally, panel (c) showcases the distance between each trajectory's evolution calculated in (a) and in (b).

Examining Figs. 3.4(a) and (b) reveals that both ways of backward integration produce the same backward temporal evolution in the y coordinate for each orbit. This is further reinforced in Fig. 3.4(c), where we see the distance between the trajectories calculated using these two approaches. The results for all trajectories indicate that there is no distance between an IC integrated by the two methods. Thus, the two numerical approaches produce identical results.

Although negative time step sizes for integration schemes applicable to ODEs lead to backward integration, the same cannot be said for FDEs. The reason for this, stems from the step size being raised to the power of alpha in the GL methods, i.e., there is a term h^α in (3.31) and (3.32). However, we can change the sign of the eom through multiplying by -1, as mentioned above for ODEs, and derive a method for backward integration. The derivation is completed by changing the sign of the left side of (3.29) and then redefining the explicit and implicit GL methods [(3.31) and (3.32)] in a manner which is utilised for backward time integration as

$$y_{n+1} - \sum_{\nu=1}^{n+1} c_\nu^\alpha y_{n+1-\nu} - r_{n+1}^\alpha y_0 = -(h^\alpha) f(y_n), \tag{3.47}$$

and

$$y_{n+1} - \sum_{\nu=1}^{n+1} c_\nu^\alpha y_{n+1-\nu} - r_{n+1}^\alpha y_0 = -(h^\alpha) f(y_{n+1}), \tag{3.48}$$

respectively. One drawback of this approach is that it is not time reversible. This pitfall comes from the term $\sum_{\nu=1}^{n+1} c_\nu^\alpha y_{n+1-\nu}$ in (3.47) and (3.48), which uses y_0 to y_n to calculate y_{n+1}. Thus, if we integrate forward in time, y_{n+1} is calculated using the information of the trajectory from t_0 to t_n. However, if we start with y_{n+1} from the forward integration and want to integrate backward in time (from t_{n+1} to t_0), the c_ν^α values (3.34) now place emphasis on the opposite y values compared to the forward integration. Therefore, this integration scheme is not time reversible.

3.5.3 Improving the performance of the fractional ordinary differential equation integration approach

The explicit and implicit GL methods outlined in Sect. 3.5.1 and Sect. 3.5.2 have a drawback originating from the calculation of the summation $\sum_{\nu=1}^{n+1} c_\nu^\alpha y_{n+1-\nu}$ appearing in (3.31), (3.32), (3.47), and (3.48). The first way of calculating this sum, is to re-evaluate all the c_ν^α coefficients (3.34) at each time step, which leads to an increase in required computational time. The second approach is based on the observation that the already computed c_ν^α values do not change from one time instant to the next; there is merely an increase in the number of required c_ν^α values. Thus, it becomes suitable to calculate the succeeding value as the flow progresses and sequentially append each new value to the array of existing c_ν^α values. This approach reduces the CPU runtime but can lead to memory issues depending on the considered time interval and the used step size. If a small integration time step is incorporated over a large time interval, which is required for an accurate approximation, the required memory increases drastically. Throughout our computations the programming language of choice was Python, where a floating point value uses 8 bytes of memory. Thus, for a time interval from $t = 0$ to $t = 60$ and an integration time step of $h = 0.001$, the number of floating point values in the c_ν^α array will be 60 000. This means 480 000 bytes of memory are required and the same amount of memory is needed for the $y_{n+1-\nu}$ array. Additionally, the summation is computed using Python's package called NumPy and its implementation of the dot product. This tool makes temporary copies of the arrays to perform the calculation which requires lots of memory. Therefore, this approach has the capability to experience memory troubles for systems that contain multiple FDEs. To circumvent these troubles, we notice from (2.33) that

$$c_\nu^\alpha \to 0 \quad \text{as} \quad \nu \to \infty, \tag{3.49}$$

and therefore, $c_\nu^\alpha y_{n+1-\nu} \to 0$ [seen in (3.31), (3.32), (3.47), and (3.48)] as $\nu \to \infty$. This convergence means that for large values of n, the calculation of $f(y_{n+1})$ does not depend on $y_{n+1-\nu}$ for large ν. Thus, when c_ν^α is less than some small tolerance value, we determine that $y_{n+1-\nu}$ can be omitted from the calculation of $f(y_{n+1})$, while still

maintaining a good level of accuracy. Therefore, once the tolerance level is met, we stop computing additional c_ν^α values and remove the associated $y_{n+1-\nu}$ values from its array to ensure that the c_ν^α and $y_{n+1-\nu}$ arrays have the same dimensions. This reduction in the dimensionality of the arrays lessens the required memory and simultaneously reduces the CPU runtimes.

To showcase how the introduction of a tolerance level improves the integration method, two dynamical systems are used to compare the complete explicit GL method, and the explicit GL method with a tolerance level for the c_ν^α values (which we call the explicit GL approximation method). The comparison will take place by using ten ICs per c_ν^α tolerance level and implementing multiple tolerance levels for each system. We then integrate the points forward and backward in time to reveal their evolution, which we use to calculate the distance between the orbits created by the actual GL method and the approximation of this method at each point in time. To ensure that the observation of the approximation is holistic, we use four α values ($\alpha = 0.9999$, $\alpha = 0.95$, $\alpha = 0.9$, and $\alpha = 0.7$) and multiple tolerance levels for each α value. The results of this examination will allow us to understand the impact of applying tolerance levels to the implementation of the GL method.

The first dynamical system which will be analysed is the fractional Duffing oscillator. The eom of the fractional Duffing oscillator (see e.g., [55]) are given as

$$\begin{aligned} D_*^\alpha x(t) &= y(t), \\ D_*^\alpha y(t) &= x(t) - x(t)^3, \end{aligned} \tag{3.50}$$

with x and y being the system's state variables. The results of the absolute difference between the explicit GL method [(3.31) and (3.47)] and the scheme with a tolerance level are presented in Fig. 3.5, where the resulting curves are coloured according to their associated tolerance level. The left-hand column of Fig. 3.5 [panels (a), (c), (e), and (g)] represents the forward integration, while the column on the right [panels (b), (d), (f), and (h)] depicts the backward time integration. Moreover, the rows from top to bottom indicate the order of the FDE as follows, $\alpha = 0.9999$, $\alpha = 0.95$, $\alpha = 0.9$, and $\alpha = 0.7$. Additionally, there are two black dashed lines which are situated at absolute difference levels of 10^{-6} and 10^{-8}, and show the possible desired accuracy agreement between the two methods.

Through an observation of Fig. 3.5, we note that each row of plots depicts that the errors produced by the forward integration methods (left-hand column) are approximately equivalent to that seen in the right column (backward integration methods). We also observe that the curves corresponding to the same c_ν^α tolerance level (curves of the same colour in all panels) in Figs. 3.5(c) and (d) intersect the lower black dashed line (absolute difference equal to 10^{-8}) at earlier times compared to the same coloured curves in Figs. 3.5(e) and (f). Furthermore, dynamical systems with higher fractional order FDEs [e.g., $\alpha = 0.9999$ in Figs. 3.5(a) and (b)] are able to implement larger tolerance levels over these integration intervals. The same is true when comparing Figs. 3.5(e) and (f) with Figs. 3.5(g) and (h), where the curves associated with a tolerance level of 10^{-8} (grey coloured curves) in Figs. 3.5(g) and (h)

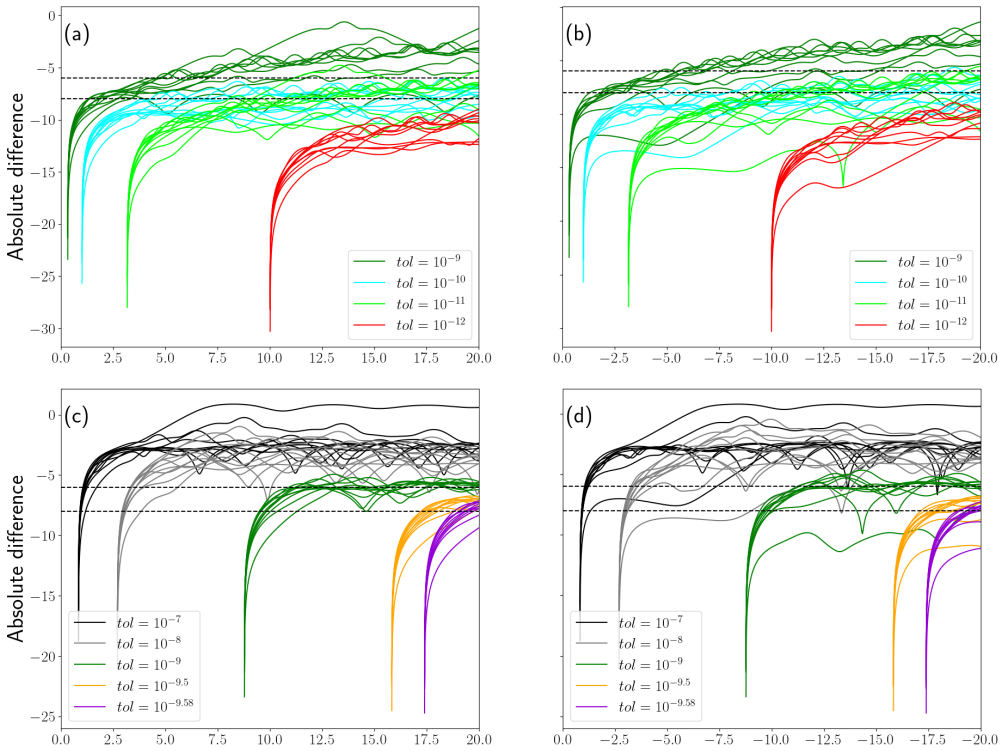

Figure 3.5: Plots showing the absolute difference between the temporal evolution of trajectories from the Duffing oscillator when it is described by FDEs (3.50) calculated by the explicit GL method and the explicit GL method with a certain tolerance level (*tol*). In computing the c_ν^α coefficients (3.34) in each panel we present results for the same ten randomly chosen ICs for various tolerance levels (different colour curves), along with two black horizontal dashed lines, indicating the absolute difference levels of 10^{-6} and 10^{-8}. Panels (a), (c), (e), and (g) correspond to forward time integration of the system from time $t = 0$ to $t = 20$, while panels (b), (d), (f), and (h) show results for backward time integration from $t = 0$ to $t = -20$. Additionally, each row of panels contains results of the dynamical system for a different α value: $\alpha = 0.9999$ in panels (a) and (b), $\alpha = 0.95$ in (c) and (d), $\alpha = 0.9$ in (e) and (f). Finally, in panel (g) we integrate from $t = 0$ to $t = 40$ and in (h) we integrate from $t = 0$ to $t = -40$, and these panels showcase the result for the system (3.50) with $\alpha = 0.7$.

only intersect the bottom dashed line after $|t| \approx 22$. Thus, larger values of α allow for more accurate tolerance levels to be utilised while still intersecting the horizontal dashed lines at earlier respective times. The earlier intersection means that a greater accuracy can be attained while still reducing the required computational time. The reason that the curves in Figs. 3.5(a) and (b) reach the bottom dashed black line sooner is attributed to the dependence of the value c_ν^α on α. We can unravel this behaviour by observing the definition

$$c_\nu^\alpha = \left(1 - \frac{\alpha + 1}{\nu}\right) c_{\nu-1}^\alpha, \tag{3.51}$$

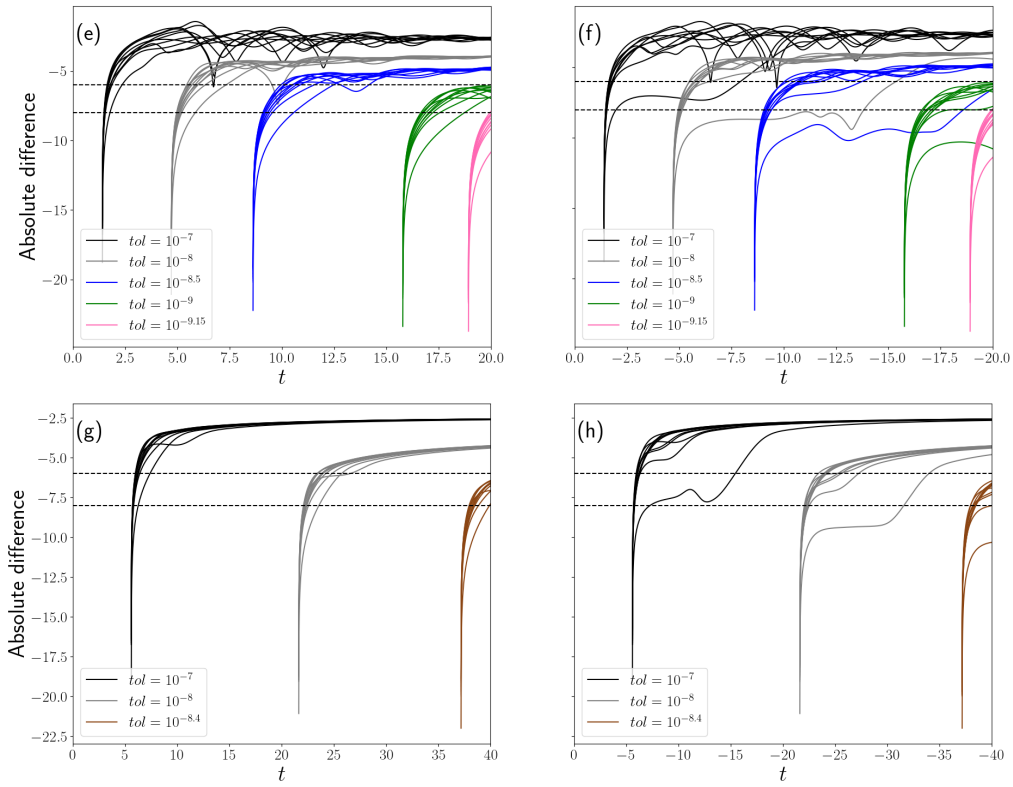

Figure 3.5: Continued.

[introduced in (3.34)] where $c_0^\alpha = \alpha$. From (3.51), it is seen that larger α values cause $1 - \frac{\alpha+1}{\nu}$ to be reduced relative to smaller α values. A smaller value of the term in parenthesis causes a larger decrease in c_ν^α. Due to the increased rate of decrease of this value, a dynamical system with a larger α value has curves of the same colour (i.e., the same c_ν^α tolerance level) that intersect the bottom dashed line in Fig. 3.5 at earlier times compared to the same coloured curves of a dynamical system with a smaller fractional order.

The next model used to demonstrate the efficiency of the GL method with a tolerance level, is the Hénon-Heiles Hamiltonian (3.19) with fractional derivatives. The eom (3.20) of this dynamical system can be explicitly given as

$$\begin{aligned} D_*^\alpha x &= p_x, \\ D_*^\alpha y &= p_y, \\ D_*^\alpha p_x &= -x - 2xy, \\ D_*^\alpha p_y &= -y - x^2 + y^2. \end{aligned} \tag{3.52}$$

To analyse this system, the same methodology as used for the Duffing oscillator is implemented. Due to the backward integration producing approximately equivalent behaviour as the forward integration (similar to what was observed in Fig. 3.5), we do not present the results for the backward integration. The results for the system with $\alpha = 0.9999$ are shown in Fig. 3.6(a), for the system with fractional order

$\alpha = 0.95$ are displayed in Fig. 3.6(b), while Fig. 3.6(c) shows the computations for $\alpha = 0.9$. Finally, the Hénon-Heiles system with FDEs of order $\alpha = 0.7$ is considered in Fig. 3.6(d).

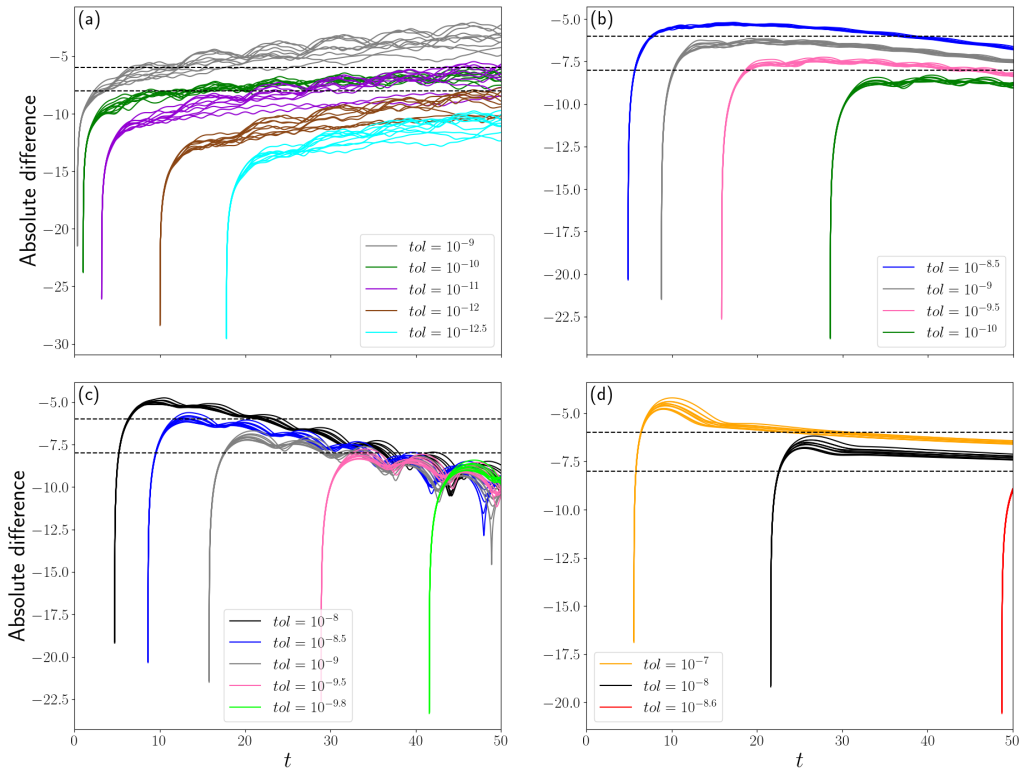

Figure 3.6: Plots showcasing the absolute difference between the forward in time flow of trajectories from the fractional Hénon-Heiles system (3.52) calculated using the explicit GL scheme and the explicit GL method with the introduction of a tolerance level. These results are presented in a similar manner to that shown in Fig. 3.5, with each panel being associated to the system with (a) $\alpha = 0.9999$, (b) $\alpha = 0.95$, (c) $\alpha = 0.9$, and (d) $\alpha = 0.7$.

Figure 3.6 demonstrates similar behaviours to those seen in Fig. 3.5. Once again, we observe that larger α values result in orbits intersecting the bottom black dashed line at smaller t values. The reason for this behaviour is yet again attributable to the calculation of c_ν^α (3.51). Therefore, we note that using the GL method with a tolerance level is extremely beneficial to reduce the CPU time while maintaining a high level of accuracy for large α values. However, in the case of smaller α values [e.g., Fig. 3.6(d)], this method does not decrease the required CPU time required to maintain a particular level of accuracy [$\log_{10}(E_r(t)) < -8$]. Thus, the complete GL method is required. Additionally, when applying a tolerance level, it is important to take note of the required integration interval as this may influence your selection of the tolerance level.

3.5.4 Time reversible integration method

The GL method that has been described up until this point is used to solve derivatives of the Caputo type (3.29). The solutions of generalised Caputo derivatives have not yet been proven to be unique [56]. Therefore, observing the dynamics associated with a backward integration method which is not time reversible [as mentioned below (3.48)] is feasible for the time being. However, it has been proven that unique solutions exist for Riemann-Liouville derivatives (see e.g., [57]). Thus, if we use the GL derivative (2.35) to approximate the Riemann-Liouville derivative (as seen in Sect. 2.2 of [2]), the integration scheme for FDEs is time reversible. Therefore, we apply (2.35) to the Riemann-Liouville derivative

$$D_R^\alpha y(t) = f(y(t)), \tag{3.53}$$

to obtain the following equation (as seen in Sect. 2.2 of [2])

$$D_R^\alpha y(t) = \frac{1}{h^\alpha}\left(y(\tau_{n+1}) - \sum_{\nu=1}^{n+1} c_\nu^\alpha y(\tau_{n+1-\nu})\right). \tag{3.54}$$

The solution of this differential equation can then be given in matrix form as

$$\frac{1}{h^\alpha}\begin{pmatrix} 1 & 0 & 0 & 0 & \dots & 0 \\ c_1 & 1 & 0 & 0 & \ddots & \vdots \\ c_2 & c_1 & 1 & 0 & \ddots & 0 \\ c_3 & c_2 & c_1 & 1 & \ddots & 0 \\ \vdots & \ddots & \ddots & \ddots & \ddots & 0 \\ c_{n+1} & \dots & c_3 & c_2 & c_1 & 1 \end{pmatrix}\begin{pmatrix} y_0 \\ y_1 \\ y_2 \\ y_3 \\ \vdots \\ y_{n+1} \end{pmatrix} = \begin{pmatrix} f_0 \\ f_1 \\ f_2 \\ f_3 \\ \vdots \\ f_{n+1} \end{pmatrix}. \tag{3.55}$$

Utilising the IC y_0, the system (3.55) can be solved numerically to reveal the forward temporal evolution. To integrate backward in time for the same orbit, the IC is now y_{n+1} and is used together with (3.55). This matrix equation can then be solved using a root finding method. To do so, one needs an initial guess of the vector containing the y values and the vector containing the f values. These vectors are then iteratively updated using a root finding method until they converge to the solution. Convergence means that the step size between one iteration and the next is less than some predetermined value, e.g., 10^{-8}.

3.6 The Lagrangian descriptors method

In this section we introduce the LDs method, which can be used to reveal the Normally Hyperbolic Invariant Manifolds (NHIMs) of a dynamical system in a computationally inexpensive manner. NHIMs are relevant in the study of dynamical systems because they are able to identify phase space regions of distinct dynamical

behaviour. Furthermore, certain properties of these manifolds allow for a comprehension of a system's underlying transport mechanisms. Thus, an introduction to and explanation of NHIMs will be the starting point of this chapter. This prelude acts as a foundation, that we will use to define and describe the LDs method in the subsequent parts of this section.

NHIMs have been presented by N. Fenichel and J.K. Moser, [58], and then further discussed by N. Fenichel in subsequent papers [59, 60]. A brief description of NHIMs can be furnished by utilising the explanation given in [61]. We begin by considering a dynamical system with an arbitrary time domain T, which may be discrete $T = \mathbb{Z}$ or continuous $T = \mathbb{R}$. The time domain may also be selected as a subset of $\mathbb{Z}$ or $\mathbb{R}$. This dynamical system has a smooth manifold X and the dynamical system's evolution is given as $\Phi : T \times X \to X$. Then the system can be given as (T, X, Φ). In the case of a discrete system we have a diffeomorphism $\varphi : X \to X$, and the full evolution function is defined as $\Phi(n, x) = \varphi^n(x)$, where $n \in \mathbb{N}_0$ is the number of iterations and $x \in X$. For a continuous system the evolution function is a flow $\Phi^t : X \to X$ which is also a diffeomorphism for any $t \in \mathbb{R}$. A manifold $\mathcal{M}$ is called invariant in a dynamical system (T, Q, Φ), where Q is the phase space and $\mathcal{M}$ is a submanifold of Q, if it is mapped to itself under Φ^t. An invariant manifold $\mathcal{M}$ is referred to as normally hyperbolic if, in the directions normal to $\mathcal{M}$, the linearisation of the flow Φ^t has a real eigenvalue spectrum, that can provide information about the stability and dynamical behaviour of the system. Due to the eigenvalues being real, the normal directions to $\mathcal{M}$ must split into directions which the linearised flow either exponentially converges towards $\mathcal{M}$ or exponentially expands along $\mathcal{M}$. However, no directions are allowed to remain neutral. The directions which experience convergence when evolved forward in time, are called stable NHIMs and those that diverge are called unstable NHIMs. When evolved backward in time, the unstable manifolds converge while those which are stable diverge. It was shown in [62] that NHIMs are preserved under small perturbations (the converse was proved in [63], specifically that manifolds which persist are normally hyperbolic). Therefore, they are useful in understanding a dynamical system's long term behaviour. This utility comes from the NHIMs enclosing regions of dynamically similar behaviour. We can then examine the trajectories associated with different phase space regions to determine their impact on various outcomes produced by a dynamical system.

Understanding the transport of particles within a dynamical system has been, and continues to be, a task which many researchers are investigating. The LDs method is a rather recently introduced tool that qualitatively discerns regions of different dynamical behaviour. At the bounds of these distinct regions lie NHIMs [3], which can be utilised to examine transport phenomena (see for example [64]). The LDs method was introduced in [65, 66] to calculate the arc-lengths of trajectories. The method has been used in a variety of research areas addressing several questions and tackling different problems, such as attempting to explain the geometry of ocean flows [66], and locating regions of bounded trajectory motion in a binary

asteroid environment [67]. Additionally, the LDs method has been used to study chemical reactions [68, 69], to examine the vibrations in molecular systems [70], and to quantify the extent of chaos found within dynamical systems [36, 71], to name a few.

The earliest form of the LDs method was called the *arc-length* definition. It quite literally measures the arc-length of a particle's evolution in phase space over an interval of time. This physical interpretation is given mathematically as follows

$$M(\mathbf{x}_0, t_0, \tau) = \int_{t_0-\tau}^{t_0+\tau} \|\mathbf{f}(\mathbf{x}, t)\| \, dt, \tag{3.56}$$

where t_0 is the time at which we focus our attention (in this study we set $t_0 = 0$), τ is the integration time, $\mathbf{x}_0$ is an IC, $\|\cdot\|$ is the usual Euclidean norm, and M denotes the LD. This process can then be repeated for each IC in some grid of points in the phase space, and each point is assigned the scalar value of the arc-length. Furthermore, we note that points which lie along a stable NHIM move towards an unstable fixed point (points which have a gradient equal to zero but are not local maxima nor local minima) when integrated forward in time, while the backward temporal evolution of the points on an unstable manifold leads them toward an unstable fixed point (see e.g., Chapt. 10 of [72]). Subsequently, the ICs with the shortest combined arc-lengths converge to a fixed point. The convergence implies that these particles form part of a NHIM. In contrast, particles which display longer arc-lengths exhibit divergence from a nearby fixed point, implying that they do not lie on a manifold.

The effect of different τ values on structures seen in LD scalar fields has been discussed in [66] and Sect. 2.1.2 of [73]. Following these works we will further discuss the impact of selecting various values of τ. The choice of time interval τ is of extreme importance when implementing the LDs method, as short intervals of integration may not allow some of the orbits to converge. Thus, the NHIMs of a dynamical system may not be depicted in their entirety, while a longer integration interval can disclose a more intricate description of a system's NHIMs. As stated in [3], 'τ in some sense is intimately related to the time scales of the dynamical phenomena that occur in the model under consideration'. This implies that one needs to determine the amount of complexity required to describe a particular dynamical mechanism of interest. However, larger values of τ require longer CPU runtimes, which reduces the benefit of this computationally inexpensive method.

To demonstrate the effect of the selection of τ, we apply the arc-length definition of the LDs method, (3.56), to the Hénon-Heiles Hamiltonian (3.19), with $H = \frac{1}{8}$. The reason that we have selected this particular energy value is because it has been shown in multiple papers (see for example [74, 75]) that it leads to significant chaoticity throughout the system. Hence, there is an increase in intricacy of the manifolds. To clearly showcase the impact of τ, we reveal manifolds in the PSS of the dynamical system, defined by $x = 0$ and $p_x > 0$. On the PSS we consider orbits with ICs on a grid of 1000×1000 points. Each orbit is integrated by the ABA864

integrator (3.18) with a step size of $h = 0.079$ to ensure the conservation of energy up to a level of $\log_{10}(E_r(t)) < -8$ as demonstrated in Fig. 3.1. For each one of the orbits the LDs method (3.56) for $\tau = 20$ and $\tau = 60$ is applied. The results are showcased in Figs. 3.7(a) and (b), respectively. The colour bars above each panel is used to colour each IC according to its LD. Additionally, in Fig. 3.7(c) we see the PSS of this Hénon-Heiles systems, as shown in Fig. 3.2(a).

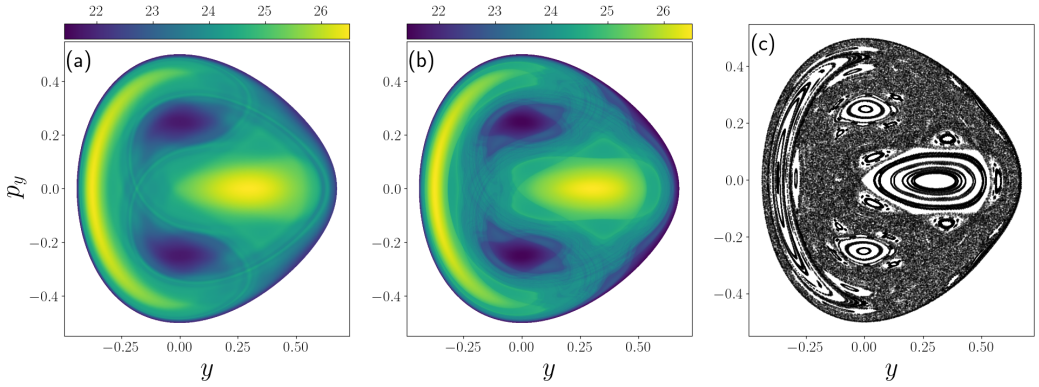

Figure 3.7: Panels (a) and (b) present ICs coloured according to the arc-length LD value (3.56), for the $x = 0$ and $p_x > 0$ PSS of the Hénon-Heiles system (3.19) with an energy of $H = \frac{1}{8}$. The magnitude of the LD values are shown in the colour bars above the panels. The plots are made using a grid consisting of 1000×1000 equidistant ICs over the interval $y \in [-0.45, 0.65]$ and $p_y \in [-0.55, 0.55]$. These panels present the results for the LDs method with (a) $\tau = 20$ and (b) $\tau = 60$. Panel (c) shows the PSS for this system and was previously depicted in Fig. 3.2.

The NHIMs in Figs. 3.7(a) and (b) are seen as the curves which correspond to sudden changes in the LD scalar field (presented as abrupt changes in colour). With this in mind, it is easy to see that the results for $\tau = 20$ [Fig. 3.7(a)] reveal less intricate manifolds when compared with the plot displaying the LD values for $\tau = 60$ [Fig. 3.7(b)]. The reason for the more complex structures seen in the phase space of the LDs figure for $\tau = 60$, is because a longer integration time allows orbits more time to potentially converge to an unstable fixed point. Additionally, we see that the phase space regions enclosed by the manifolds in Fig. 3.7(b) better define regions which are either chaotic or regular. When creating the results seen in Fig. 3.7, we note that the LDs method [Figs. 3.7(a) and (b)] requires less CPU time than the PSS in Fig. 3.7(c). Moreover, Fig. 3.7(c) shows regions that are either chaotic or regular, while Fig. 3.7(b) depicts NHIMs which further separate these different regions. Understanding how these manifolds influence the transport of trajectories in phase space for a specific Hamiltonian system will be the goal of Chapt. 4.

Since the inception of this conceptually simple definition (3.56) further modifications which contain inherent benefits to the study of dynamical systems and the corresponding transport phenomena have arisen [73]. One such definition is the

so-called p-*'norm'* definition of the LDs method. This approach allows for an in-depth analysis of the singular features of dynamical systems and is beneficial when extracting the NHIMs from LDs computations [76, 77]. The p-'norm' definition of the LD is

$$M_p(\mathbf{x}_0, t_0, \tau) = \int_{t_0-\tau}^{t_0+\tau} \sum_{i=1}^{N} \left| f_i(\mathbf{x}, t) \right|^p dt, \tag{3.57}$$

where $f_i(\mathbf{x}, t)$ is the i^{th} component of a vector field. Parameter p is chosen in such a way that it allows for the greatest discontinuity of the gradient of the LD values at the manifold, thus allowing us to extract the NHIMs from the LDs. It has been shown that this occurs at $p = 0.5$ for a wide variety of dynamical systems [76, 78]. Since $p < 1$, the integrand in (3.57) is not an actual norm; this is the reason there are inverted commas over the word norm in the definition.

Due to the p-'norm' LDs method being particularly efficient at highlighting the singularities of a dynamical system, we now wish to showcase such features and describe how they are used to extract the NHIMs from the results of the LDs method. For this purpose we apply the p-'norm' definition of the LDs method (3.57) to the Hénon-Heiles Hamiltonian in a similar fashion to Fig. 3.7. However, we do not use the same energy as seen in Fig. 3.7. Instead, we consider an energy of $H = \frac{1}{12}$, which produces a simple manifold structure to easily highlight the singularities. The PSS defined by $x = 0$ and $p_x > 0$ is examined for a set of ICs on an equidistant grid of 1000×1000 points. The grid pertains to the intervals $y \in [-0.45, 0.55]$ and $p_y \in [-0.45, 0.45]$ and the LDs method uses an integration time of $\tau = 60$. In this way we create the result displayed in Fig. 3.8(a). In this figure we select a line segment (shown in black), which is defined by $y = 0$ and $p_y \in [-0.35, 0.35]$, for which we depict the LD values in Fig. 3.8(b). In that figure we present an example of the singular features of the LD values at the points signified by the red arrows. The LD values at the points shown by the red arrows correspond to ICs which lie on the NHIMs in panel (a).

Through an examination of Fig. 3.8(b), it is seen that there are extreme changes in the gradient of LDs (also known as singularities or a discontinuity in the spatial derivative [73]) at $p_y \approx -0.28, -0.125, 0.125, 0.28$ (indicated by the red arrows in both panels). These singularities indicate that the line crosses through a NHIM and specifies a change in dynamical regimes, as seen in Fig. 3.8(a). This drastic alteration in the LD spatial gradient at a NHIM can be used to extract the manifolds from the scalar field of LD values. Observing the scalar field as a m dimensional grid of ICs in phase space ($m \leq 2N$), one is able to calculate the norm of the gradient of the LD values at each grid point ($\|\nabla M_p(x_0, t_0, \tau)\|$). The gradient values associated with each grid point is then used to determine values greater than some predetermined lower bound d, i.e., $\|\nabla M_p(x_0, t_0, \tau)\| > d$. The ICs which satisfy this condition are deemed to form part of the NHIMs, and may be extracted to explicitly display the manifolds. The value of the lower bound d is chosen appropriately such that it allows the extraction of many manifolds of a dynamical system. This value depends on the considered dynamical system and the value τ of the chosen time

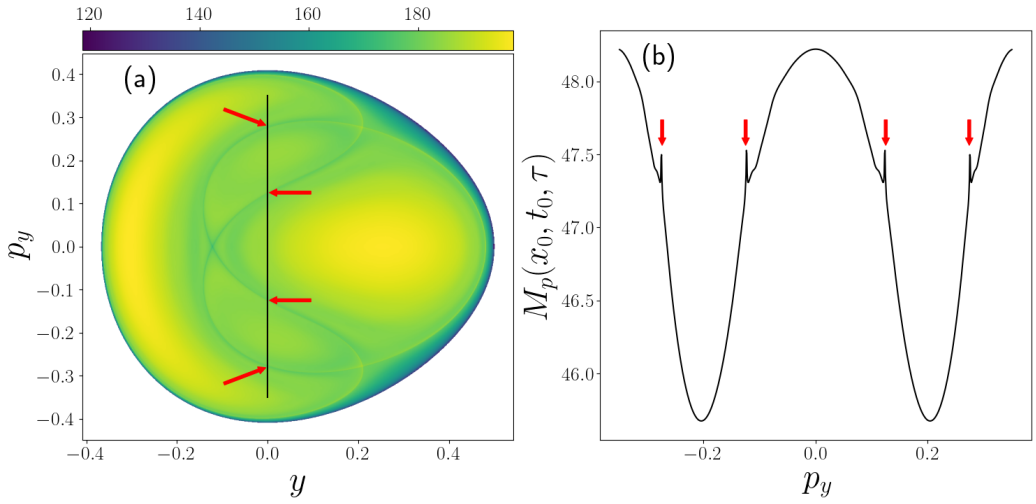

Figure 3.8: Panel (a) shows ICs coloured according to their p-'norm' LD value (3.57) for $p = \frac{1}{2}$ (presented in the colour bar above the plot), for the $x = 0$ and $p_x > 0$ PSS of the Hénon-Heiles system (3.19) with an energy of $H = \frac{1}{12}$. The LDs method uses $\tau = 60$, and the ICs lie on an equidistant grid of 1000×1000 points over the interval $y \in [-0.4, 0.55]$ and $p_y \in [-0.45, 0.45]$. The LD values along the black line on the $y = 0$ axis from $p_y = -0.35$ to $p_y = 0.35$ in (a) are depicted in panel (b). The red arrows in both panels indicate the points where the LD values correspond to a NHIM.

interval. Finally, the numerical approximation of the LD gradient $G_{LD}(x_0)$ in one direction is calculated using the central difference method as

$$G_{LD}(x_0) = \frac{M_p(x_0 + h) - M_p(x_0 - h)}{2h}, \tag{3.58}$$

where x_0 is the considered IC, h is the step size between grid points in this direction, $M_p(x_0 + h)$ is the LD value at the point $x_0 + h$, and $M_p(x_0 - h)$ is the LD value at the point $x_0 - h$. At the left and right bounds of each dimension, the central difference method cannot be used because either $M_p(x_0 + h)$ or $M_p(x_0 - h)$ does not exist. Therefore, it is required to implement the forward and backward difference methods, which are respectively given by

$$G_{LD}(x_0) = \frac{M_p(x_0 + h) - M_p(x_0)}{h}, \tag{3.59}$$

and

$$G_{LD}(x_0) = \frac{M_p(x_0) - M_p(x_0 - h)}{h}. \tag{3.60}$$

Once G_{LD} values for each grid point in every direction $(1, \ldots, m)$ is calculated, the approximation of the total gradient is evaluated as

$$\|\nabla M_p(x_0, t_0, \tau)\| = \sqrt{(G_{LD,1})^2 + \cdots + (G_{LD,m})^2}, \tag{3.61}$$

where $G_{LD,1}, \ldots, G_{LD,m}$ denote the gradient taken in each dimension.

To demonstrate how the gradient method is implemented to extract the NHIMs, the Hénon-Heiles Hamiltonian is, once again, utilised. In particular, the manifolds are extracted for the system shown in Fig. 3.8(a), with an energy of $H = \frac{1}{12}$ and the same number of ICs, the same integration time, and over the same intervals. To extract the NHIMs, we used a lower bound of $d = 0.09$ for the total LD gradient. Employing the gradient method (3.61), along with this tolerance level, reveals the NHIMs of this PSS, $x = 0$ and $p_x > 0$, as is shown in Fig. 3.9.

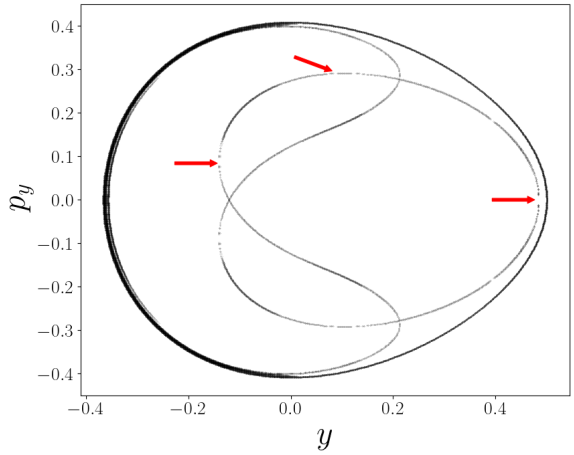

Figure 3.9: The NHIMs extracted from Fig. 3.8, using a lower bound for the values of the LD gradient (3.61) $d = 0.09$, i.e $\|\nabla M_p(x_0, t_0, \tau)\| > d$. The red arrows denote regions where our numerically calculated NHIM looks discontinuous.

In Fig. 3.9 the NHIMs are clearly seen. However, one may ask why some of the lines look discontinuous (for example see regions shown by the red arrows). This disconnect is attributable to one of two factors. Firstly, the NHIMs being extracted by means of a finite grid of points. In particular, the considered grid consists of only 1000×1000 ICs and therefore, some of the points which create the manifolds, are not a part of the grid. If a more densely populated grid is considered, the manifolds would better resemble continuous curves. The second possibility is that some of the points which make up the NHIMs have not yet had sufficient integration time to converge relative to nearby points. Thus, the gradient does not satisfy the tolerance level.

At this point, it is beneficial to recall from the start of this section, that forward integration leads to the exposition of the stable manifolds and backward integration highlights the unstable NHIMs. Thus, by splitting the LDs method into its forward and backward integration components, one can easily obtain and extract the stable and unstable manifolds using the same methodology presented for the total NHIMs. The forward p-'norm' LD is defined as

$$M_p^f(\mathbf{x}_0, t_0, \tau) = \int_{t_0}^{t_0+\tau} \sum_{i=1}^{N} \left| f_i(\mathbf{x}, t) \right|^p dt, \tag{3.62}$$

and the backward p-'norm' LD as

$$M_p^b(\mathbf{x}_0, t_0, \tau) = \int_{t_0-\tau}^{t_0} \sum_{i=1}^{N} \left| f_i(\mathbf{x}, t) \right|^p dt. \tag{3.63}$$

To demonstrate the stable and unstable manifolds of the Hénon-Heiles Hamiltonian with an energy of $H = \frac{1}{12}$, we can use the exact same setup as seen in Fig. 3.9, but calculate the gradients of the forward and backward components of the LDs separately. The stable manifolds are showcased in Fig. 3.10(a), the backward NHIMs are seen in Fig. 3.10(b), and the superposition of these two panels are seen in Fig. 3.10(c), which is identical to Fig. 3.9.

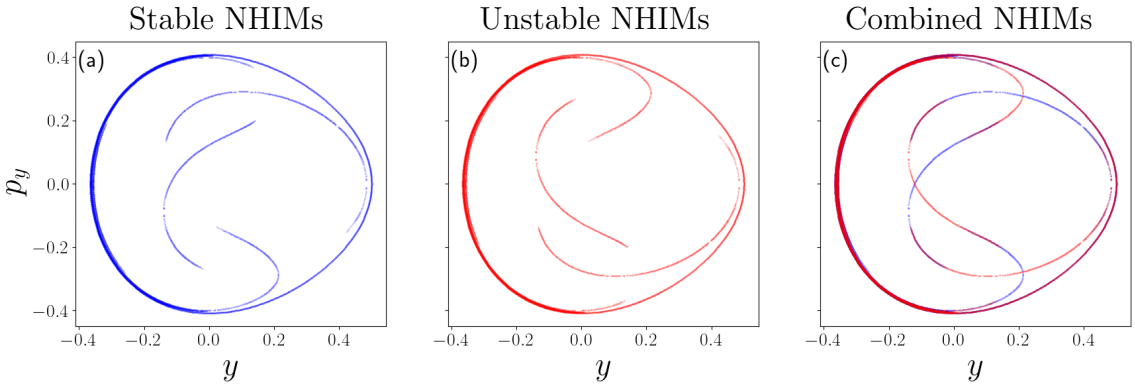

Figure 3.10: The extraction of the (a) stable and (b) unstable NHIMs of Fig. 3.8 using the forward (3.62) and backward (3.63) p-'norm' LDs method with the gradient (3.61) satisfying $\|\nabla M_p(x_0, t_0, \tau)\| > d$ with $d = 0.09$. Panel (c) shows the stable and unstable manifolds superimposed.

Figure 3.10(c) shows that the splitting of the p-'norm' LDs method, (3.62) and (3.63), allows for the entire dynamical system's NHIMs to be represented with the same accuracy as seen for the full p-'norm' definition, (3.57). Additionally, Figs. 3.10(a) and (b) display explicitly the stable and unstable manifolds, respectively. Precisely examining the stable and unstable NHIMs is beneficial when studying the transport of particles within a dynamical system. Its utility arises when examining the particular influence of the two kinds of NHIMs on a trajectory's path.

3.7 Summary

In this chapter, we initially presented two numerical integration schemes, a RK6 method in Sect. 3.1 and a symplectic integrator in Sect. 3.2. We then compared the performance of the two methods by examining the relative energy error $E_r(t)$ (3.24) of a chaotic and a regular orbit from the Hénon-Heiles system (3.19). This comparison revealed that the $E_r(t)$ curve for the ABA864 method is asymptotically

bounded from above, while the relative energy error for the RK6 method increases over time. Additionally, we found that the ABA864 scheme required less CPU time compared to the RK6 method to integrate the orbits over the given time interval for a desirable energy accuracy. However, it was noted that symplectic integrators can only be used for separable Hamiltonian systems. We then discussed the PSS method, which allows one to view phase space structures of low dimensional dynamical systems. Up to this point we had only considered systems whose evolution is governed by ODEs. Therefore, in Sect. 3.5 we presented two integration schemes for FDEs: one which preserves time reversibility and one which does not. After showcasing the method which is does not preserve time reversibility, we introduced a way to improve the computational efficiency of this technique.

Section 3.6 began by introducing the concept of NHIMs. We then presented the LDs method and provided a physical interpretation of the technique by first discussing the arc-length definition, (3.56). We showed that when many ICs are integrated forward and backward in time and those corresponding to the largest spatial gradient values of LDs form part of the NHIMs. Then we demonstrated how τ influences the obtained results. In Fig. 3.7 it was shown that smaller τ values do not fully display the complexity of NHIMs, whereas larger τ values better reveal the entire dynamical system's manifolds. However, these larger τ values require more computational time and expose manifolds which have less of a global bearing on the phase space transport. We then introduced the p-'norm' definition of the LDs method (3.57), which provides additional benefits when compared to the arc-length approach. We also used it to visualise a system's NHIMs by stimating the gradient of the LD values. Finally, we showed how the LDs method can be split into its forward and backward components to reveal the stable and unstable manifolds, respectively.

Chapter 4

Study of a galactic type potential

The goal of this chapter is to investigate the possible connection of ring and spiral structures observed in real galaxies and in dynamical models of such objects, by studying the dynamics of the manifolds associated with unstable periodic orbits through the computation of the LDs. For this purpose we consider a Hamiltonian system consisting of a simple galactic potential, which describes the movement of stars within a galaxy. The galactic potential in our study comprised of two Miyamoto disks [79] and may be considered as an approximation of the Milky Way galaxy's potential. This model is decidedly described in [4], where various phase space structures near the stable periodic orbits of the studied galactic potential were investigated in detail. This Hamiltonian system was also implemented in [80] to examine the dynamical behaviour in the vicinity of simple and double unstable periodic orbits. That research was then extended to observe the orbital behaviour in the neighbourhood of complex unstable periodic orbits in the same Hamiltonian system of galactic type [81].

4.1 The Hamiltonian model

The Hamiltonian model we consider has the following form

$$H(x,y,z,\dot{x},\dot{y},\dot{z}) = \frac{1}{2}(\dot{x}^2+\dot{y}^2+\dot{z}^2) + \Phi(x,y,z) - \frac{1}{2}\Omega_b^2(x^2+y^2), \tag{4.1}$$

where x, y, and z describe the Cartesian coordinates of a particle (star) within the galactic model, $\dot{x}$, $\dot{y}$, and $\dot{z}$ are the usual time derivatives of the spatial coordinates, and Ω_b is the rotational velocity (also known as the pattern speed). The potential of the system, $\Phi(x,y,z)$, is

$$\Phi(x,y,z) = -\frac{GM_1}{\sqrt{x^2+\frac{y^2}{q_a^2}+\left(a_1+\sqrt{\frac{z^2}{q_b^2}+b_1^2}\right)^2}} - \frac{GM_2}{\sqrt{x^2+\frac{y^2}{q_a^2}+\left(a_2+\sqrt{\frac{z^2}{q_b^2}+b_2^2}\right)^2}}, \tag{4.2}$$

and consists of two Miyamoto disks [79] of masses M_1 and M_2 having different parameter values. This is the system's gravitational potential and describes the

distribution of mass within the galaxy, as well as provides a way to examine how the mass influences the motion of stars in the gravitational field of a galaxy. If we combine the gravitational potential and the centrifugal potential [corresponding to the term in (4.1) containing the pattern speed], we obtain the effective potential, which provides a basis to understand the motion of stars within a galaxy and also the structures that these stars produce. The effective potential is delineated by

$$\Phi_{\text{eff}}(x, y, z) = \Phi(x, y, z) - \frac{1}{2}\Omega_b^2(x^2 + y^2). \tag{4.3}$$

For the purpose of our investigation, the parameter values and units of this system have been selected such that they are the same as those shown in [4]. This galactic potential possesses the following parameter values: $a_1 = 0$kpc, $b_1 = 0.495$kpc, $a_2 = 7.258$kpc, $b_2 = 0.520$kpc, $q_a = 1.2$, $q_b = 0.9$, and the masses of the two Miyamoto disks are given as $M_1 = 2.05$ mass units and $M_2 = 25.47$ mass units. The parameters $a_{1,2}$ and $b_{1,2}$ are the Miyamoto disks' scaling factors, and the geometry of the disks is ascertained by the parameters q_a and q_b (Binney and Tremaine, [82], pg 73-74). The mass unit, (m), corresponds to $10^{10} \cdot M_\odot$, where $M_\odot$ is a solar mass, which is approximately $1.989 \cdot 10^{30}$kg. The distance unit, (r), is defined by 1 kiloparsec (kpc), and the time unit, (t), is $\approx 1.4718889907 \cdot 10^{14}$s. The rationale behind the specific selection of the value of the time unit, is to ensure that the gravitational constant, G, is ≈ 1, in terms of our chosen unit values, which can be exhibited through the transformation of the units of $G = 6.672 \cdot 10^{-11} \frac{\text{m}^3}{\text{kg} \cdot \text{s}^2}$ (the actual value of the gravitational acceleration) into an expression written in terms of the selected units. The transformation is portrayed below

$$\begin{aligned}
G &= 6.672 \cdot 10^{-11} \frac{\text{m}^3}{\text{kg} \cdot \text{s}^2} \\
G &= \left(6.672 \cdot 10^{-11}\right) \frac{\left(3.08567 \cdot 10^{16}\ \text{km}\right)^{-3}}{\left(10^{10} \cdot 1,989 \cdot 10^{30}\ \text{kg}\right) \cdot \left(1.4718889907 \cdot 10^{14}\ \text{s}\right)^2} \\
G &= \left(6.672 \cdot 10^{-11}\right) \frac{\left(3.08567 \cdot 10^{19}\ \text{m}\right)^{-3}}{\left(10^{10} \cdot 1,989 \cdot 10^{30}\ \text{kg}\right) \cdot \left(1.4718889907 \cdot 10^{14}\ \text{s}\right)^2} \\
G &= 0.9785847602 \frac{(r)^3}{(m) \cdot (t)^2} \\
G &\approx 1 \frac{(r)^3}{(m) \cdot (t)^2}.
\end{aligned} \tag{4.4}$$

By incorporating the distance and temporal units, the velocity unit, (v), is obtained through the following calculation

$$(v) = \frac{(r)}{(t)} = 207.3818151\ \text{km} \cdot \text{s}^{-1}. \tag{4.5}$$

Our attention may now revert to attaining the goal set at the beginning of the chapter, with respect to the, now, fully defined Hamiltonian. One way to do this, is to examine the dynamics in the equatorial plane (where the ring and spiral structures are most prominent), and to disregard the oscillations in the vertical, z, axis. Thus, we reduce the model from 3 dof to 2 dof by setting $z = \dot{z} = 0$ in the Hamiltonian system, so that a particle's evolution would be restricted to the equatorial plane. That is, the effective potential may be written in a format which only describes the dynamics on the equatorial plane as follows

$$\begin{aligned} &\Phi_{\text{eff}}(x, y, z = 0) = \Phi(x, y, z = 0) - \frac{1}{2}\Omega_b^2(x^2 + y^2) \\ \Rightarrow &\Phi_{\text{eff}}(x, y) = -\frac{GM_1}{\sqrt{x^2 + \frac{y^2}{q_a^2} + (a_1 + b_1)^2}} - \frac{GM_2}{\sqrt{x^2 + \frac{y^2}{q_a^2} + (a_2 + b_2)^2}} - \frac{1}{2}\Omega_b^2(x^2 + y^2). \end{aligned} \tag{4.6}$$

This 2D effective potential is visualised by means of an energy surface, where a contour plot is utilised to indicate the isoenergetic curves within the effective potential. In order to create such a plot, we use the same pattern speed (rotational velocity) as implemented in [4], $\Omega_b = 60\,\text{km}\,\text{s}^{-1}\,\text{kpc}^{-1}$, along with an equidistant grid of 1200×1200 x and y points over the interval $x, y \in [-6, 6]$. The effective potential is then calculated at each of these points giving rise to the energy surface displayed in Fig. 4.1, where the colourbar showcases a subset of the energy spectrum (all possible energy valuess for this system). The 3D plot has also been projected onto the floor of this figure to define different regions of the surface by their 2D shapes. Additionally, we have selected six specific energy values, which are useful when describing the permitted evolution of an orbit with a certain energy level. Five of these values ($\Phi_{\text{eff}} = -4.9, -4.4, -4.2, -4.14, -4.08$) are represented by the red triangles on the colourbar and red curves on the 3D potential energy surface as well as its contour plot. The energy level $\Phi_{\text{eff}} = -4.247$ is shown as blue curves and indicated by a blue triangle.

From Fig. 4.1, it can be seen that there are two points where the blue curves intersect one another, at $\Phi_{\text{eff}} \approx -4.247$. These points are called saddle points: they have a gradient equal to zero but are not local minima nor local maxima. Saddle points are also called unstable fixed points. These points separate regions of higher (seen as lighter colours containing red crescent shaped curves inside the blue curves) and lower (seen as darker colours having red circular shaped curves) energies. If a star has an energy slightly greater than $\Phi_{\text{eff}} \approx -4.247$, it has the capability to move between circular regions with lower energy surrounding the origin (we shall call this the central or interior region) and the lower energy regions further away from the origin. These distant regions are found outside of the isoenergetic contour containing the saddle points (we shall refer to this as the exterior region). However, the orbit does not have sufficient energy to travel to regions of higher energy levels. The regions of larger energy are seen as crescent shapes on the left and right of the plot in the x direction of Fig. 4.1. As the orbit cannot enter these regions,

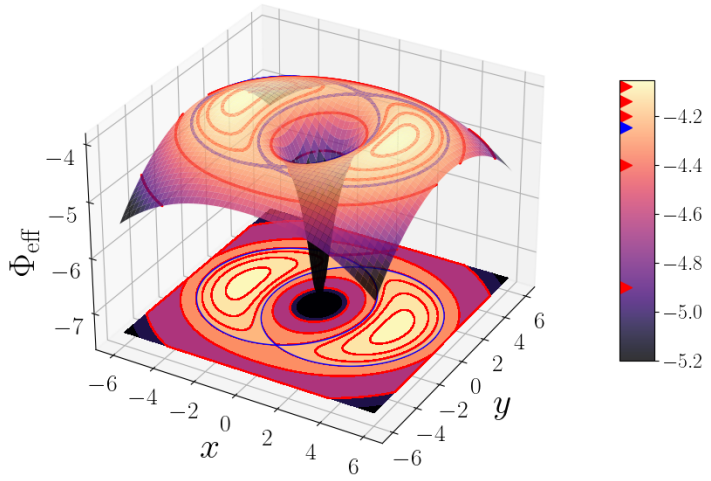

Figure 4.1: 3D contour plot of the effective potential energy (4.6), created using a 1200×1200 grid of x and y ICs. The floor of the figure shows the contour plot of the energy surface. All points are coloured according to their $\Phi_{\text{eff}}(x, y, z = 0)$ value (4.6) by using the colour scale to the right of the figure. Additionally, the colourbar contains five different red triangles which represent the following values $\Phi_{\text{eff}}(x, y, z = 0) = -4.9, -4.4, -4.2, -4.14, -4.08$ and one blue triangle which corresponds to $\Phi_{\text{eff}}(x, y, z = 0) = -4.247$. These values have also been depicted on the 3D and 2D energy surfaces as isoenergetic contour lines.

we call them the energetically forbidden regions. It was claimed in [83] that orbits which escape from the interior region, through the opening between the energetically forbidden regions, contribute to the ring and spiral structure of galaxies.

Understanding the morphological features of barred galaxies is a very small part of the broad field of galactic dynamics. For a more in-depth look at various galactic morphologies and associated features, one can refer to [84]. The work conducted on this field of research, which most closely resembles the study seen in this chapter is given by a series of papers by Romero-Gómez, Athanassoula, and their co-workers [85, 86, 87, 88]. In these works it was shown that the NHIMs ofthe galactic model dictate the dynamics of the orbits near the unstable fixed points (called Lagrange points L_1 and L_2 in galactic dynamics). It was then argued that stars within tubes of NHIMs are guided from the interior region to the exterior region and form part of the spiral and ring morphologies seen in galaxies. The fixed points of the system described by (4.1) with $H(x, y, z = 0, \dot{x}, \dot{y}, \dot{z} = 0)$, satisfy

$$\frac{\partial \Phi_{\text{eff}}}{\partial x} = \frac{\partial \Phi_{\text{eff}}}{\partial y} = 0. \tag{4.7}$$

There are five solutions to (4.7), and they are called the Lagrange points. The first two Lagrange points, L_1 and L_2, occur at the saddle points of the effective potential, the third is a local minimum, L_3. The final two Lagrange points, L_4 and L_5, are the two local maxima of the surface as seen in Fig. 4.1. The motivation

for the interest in the unstable Lagrange points, indicated in [85, 86, 87, 88], is attributable to the property that an IC's associated energy determines whether the related orbit escapes from the central region. If the energy is greater than the energy of the unstable fixed points but less than the energy of the L_4 and L_5 points, then this orbit can travel between the central region and the exterior region through the channels between the energetically forbidden regions. The same cannot be said when one considers an energy level less than that of L_1 and L_2: orbits will either exist within the central region or outside of the central region, but will not have sufficient energy to travel over the saddle points and escape. On the other hand, if the system's energy is greater than the local maxima of the potential, there are no energetically forbidden areas and particles may travel to any spatial region. Thus, such an orbit has no region to escape from.

Returning our attention to Fig. 4.1, we note that the projection of the 3D plot may be expressed in an alternate manner. Explicit isoenergetic contour curves may instead be provided to annotate the saddle points, the central region and the locally maximum stable Lagrange points (potentially causing energetically forbidden regions). This redefined plot can be seen in Fig. 4.2, where the isoenergetic contour curves are shown as black dashed curves and the curve that intersects the saddle points is displayed as an orange dashed curve. Finally, the fixed points are indicated as blue dots. The blue dots that are intersected by the orange curves are L_1 and L_2, the blue point at the origin is the local minimum (L_3) and the blue points along the $y = 0$ axis in the middle of the left and right crescent shapes are the local maxima (L_4 and L_5).

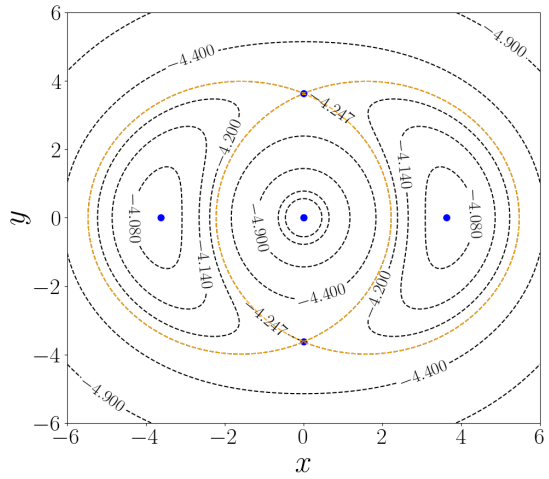

Figure 4.2: Isoenergetic contour plot of the effective potential energy (4.6), created using a 1200×1200 grid of x and y ICs. The orange dashed lines represent the isoenergetic contour relating to L_1 and L_2, shown as the blue dots on the orange curves. The blue dot at the origin represents L_4, while the remaining two dots are L_4 and L_5. The related energy value of each contour curve is also given.

Figure 4.2 allows for a qualitative explanation of the different regions encountered when describing escapes. By permitting stars to have an energy level between $\Phi_{\text{eff}} \approx -4.27$ (orange dashed curve) and $\Phi_{\text{eff}} \approx -4.2$ (first black crescent shaped black curves inside the orange curves), orbits then have sufficient energy to move from the central region (showcased by the concentric circles of contours) to the exterior region (seen as the concentric elliptical contour lines) or vice versa. However, these orbits do not have adequate energy to enter regions where the energy is greater than -4.2, referred to as the energetically forbidden regions (the approximate crescent shapes at the left and right sides of the plot). It is this movement of orbits from the interior region to the exterior region which gives rise to various orbital morphologies (galactic structures).

Having examined how the system's energy regulates its capacity to exhibit escaping orbits, a natural question arises: How can we formulate a quantitative criterion to discern whether an orbit has escaped or entered the central region? Additionally, we require that this criterion must be generally applicable across relevant energy levels and be calculable for distinct energy states. To ascertain the nature of this criterion, an obvious starting point is to acknowledge that the unstable Lagrange points exert influence on the role of escapes (or entrances); however, the question remains: In what manner? It was shown, in papers such as [89, 90, 91], that the periodic orbits (the so-called Lyapunov orbits) which surround the L_1 and L_2 points can be used to quantitatively determine whether a trajectory has escaped the interior region. To locate the Lyapunov orbit, we find the position of a period 1 periodic orbit in the phase space of the N dimensional system. We note that the periodicity of a periodic orbit, for our system, refers to the number of times an orbit crosses the x-y plane before returning to its initial position. The method to find such orbits is outlined below.

To locate an n period periodic orbit on the PSS for our system, we start with an initial guess for the IC of the periodic orbit, or if a rough estimate of the Lyapunov orbit is known it may be used as the initial position, called $u(t_0)$. In addition, we require two additional coordinates (one for each dimension of the PSS), which are slightly deviated from $u(t_0)$. They are deviated in the direction of a different dimension and are denoted as $\delta u_i(t_0),\ i = 1, 2$. Then, $u(t_0)$ and $\delta u_i(t_0)$ are integrated individually until they intersect the PSS n times. The difference between the position of vector $u(t)$ and all the vectors $\delta u_i(t)$ are calculated and then displayed in a matrix (A) where the columns of the matrix are the δu_i. The need for matrix A, is displayed in the prevailing condition

$$\delta u(t) = A\delta u(t_0), \tag{4.8}$$

and A is utilised in updating the guessed IC and iteratively converging upon the periodic orbit. The Newton-Raphson method can be implemented to iteratively determine the Lyapunov orbit through the following implementation

$$u_{j+1}(t_0) = u_j(t_0) - (A - \mathbb{I}_{N-2})^{-1}(u_j(t) - u_j(t_0)), \tag{4.9}$$

where $\mathbb{I}_{N-2}$ is the $(N-2)\times(N-2)$ identity matrix, j denotes the current iteration of the root finding algorithm and $j+1$ is the next iterate. This method is repeated until the value of the distance $|u_j(t) - u_j(t_0)|$ becomes smaller than some predefined tolerance, where the tolerance is the desired difference in distance between the initial point and the point after n intersections of the surface of sections. Once the tolerance level has been met, it means that the period n periodic orbit has been found.

To implement the method, outlined above, for our system of 2 dof (corresponding to a phase space of 4 dimensions), the relevant surface of sections is considered to be the x-y plane. Thus, deviations are chosen along the x and y directions, with a deviation size of 6.31×10^{-5}. This deviation size was found to provide the most accurate results in the shortest length of computational time. For the integration of our points, it is crucial to note that the RK6 (3.6) is utilised as the system (4.1) is not separable (see Sect. 3.2 for an explanation as to why this is important). The required step size to achieve a tolerance criterion of 10^{-14}, is determined to be $h = 10^{-7}$. Through the implementation of the method for our galactic model (4.1) with an energy of $H = -4.2$, the Lyapunov orbits surrounding L_1 and L_2 were found to intersect the x-y plane at $(x, y, \dot{x}, \dot{y}) = (0, 4.176178503629333, 0.37085199876218156, 0)$ and $(x, y, \dot{x}, \dot{y}) = (0, -3.0421633513032442, 0.3915935379499883, 0)$. However, if these Lyapunov orbits are viewed over the entirety of phase space, they are seen to be symmetric about the $y = 0$ axis. Thus, their outermost points in configuration space are $(x, y) = (0, 4.176178503629333)$ and $(x, y) = (0, -4.176178503629333)$ respectively.

As the position of the Lyapunov orbits have been determined, it is possible to qualitatively showcase that they can, indeed, be employed as a proxy in quantitatively determining whether an orbit has escaped. To depict the utility of the Lyapunov orbit, we examine how an orbit navigates from the central region to the exterior region. We use the Hamiltonian system, (4.1), with an energy of $E = -4.20$ along with the same Ω_b value ($\Omega_b = 60\,\mathrm{km\,s^{-1}\,kpc^{-1}}$) and parameters as shown previously. The results are presented in Fig. 4.3, where the grey regions represent the energetically forbidden regions, the blue elliptical curve depicts the Lyapunov orbit, the orange dot showcases the IC of the presented orbit, $(x_0, y_0, , \dot{x}_0, \dot{y}_0) = (0.9, 2.47, 0, 0)$, and the orange curve indicates the orbit's trajectory. This figure highlights the path of a particle's evolution and shows that the orbit truly escapes once it gets past the outermost point of the Lyapunov orbit, as was shown in [91]. However, the particle escapes the central region through a gap between the Lyapunov orbit and the energetically forbidden region. It is for this reason that the Lyapunov orbit cannot be directly used as a criterion for determining whether an orbit has escaped the energetically forbidden region. However, one can incorporate the outermost point of the Lyapunov orbit by constructing a circle centred at the origin of configuration space, with a radius equal to the outermost point of the Lyapunov orbit in phase space. Then the gap between the energetically forbidden regions can be covered by the two appropriate segments of this circle, shown as the black curves in Fig. 4.3. As an orbit passes through these segments,

with an outward velocity, it is classified as escaped. Although the figure below only demonstrates this behaviour for a single orbit, we have examined multiple orbits and witnessed the same result. Thus, to classify whether an escape has occurred is to determine whether an orbit has passed through either of the segments with an outward velocity.

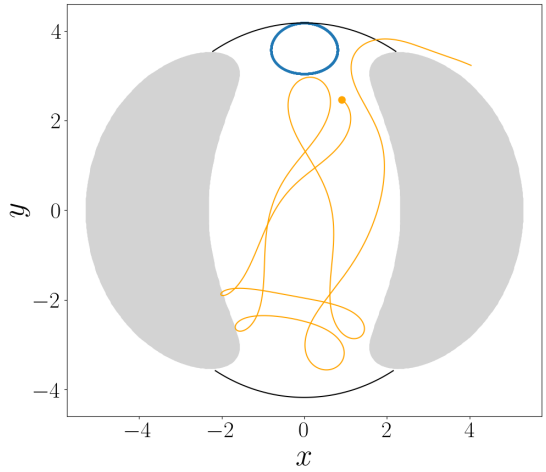

Figure 4.3: The forward temporal evolution (shown as the orange curve) of a trajectory from the Hamiltonian system (4.1) with an IC of $(x_0, y_0) = (0.9, 2.47)$ (the orange dot). The system has an energy of $H = -4.2$ and a pattern speed of $\Omega_b = 60\,\mathrm{km\,s^{-1}\,kpc^{-1}}$. The orbit is integrated until it has escaped the central region (enclosed by the grey energetically forbidden regions) defined as crossing the black curve which is found using the escape criterion (see text for details) related to the corresponding Lyapunov orbit of the system (shown as the blue elliptical curve).

4.2 Lobes defined by the Lagrangian descriptors

To examine the influence of the NHIMs on the outcomes of various trajectories it is useful to plot the LDs of the system (4.1) when motion is restricted to the equatorial plane using the p-'norm' definition of the LDs method (3.57). Extracting the manifolds from these plots allows us to identify distinct regions enclosed by various manifolds, referred to as lobes. We are then able to examine the dynamical behaviour displayed by orbits originating from different lobes. The subspace of the full phase space which is chosen for this display of the LDs method, is the PSS defined by setting $x = 0$ and $p_x > 0$. We chose this subspace because it allows us to holistically examine the dynamics of orbits from the centre of the central region to those in the vicinity of the Lyapunov orbits. This choice affords us the opportunity to determine the IC, within the lobes, of orbits which create various morphologies. The LDs in this plane are highlighted by using the system with an energy of $H = -4.2$, to ensure that there is an opening to the central part of the

galactic system. A grid size of 2000×2000 is used, as well as an integration time of $\tau = 60$, to create the results displayed in Fig. 4.4.

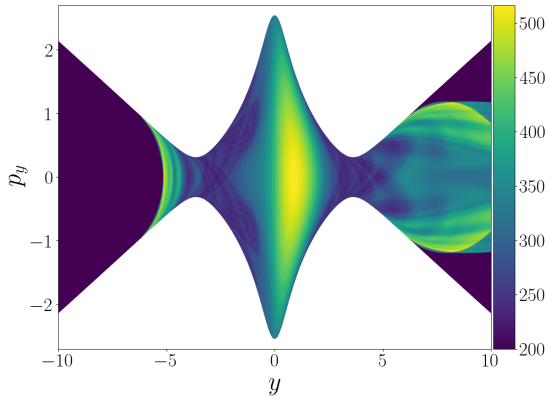

Figure 4.4: Results for the PSS, defined by $x = 0$, $p_x > 0$ for the Hamiltonian system of galactic type (4.1) with $z = \dot{z} = 0$, displaying the manifolds using p-'norm' LDs method (3.57). This system has a pattern speed of $\Omega_b = 60\,\mathrm{km\,s^{-1}\,kpc^{-1}}$ and an energy of $H = -4.2$. The plot is created using a grid of 2000×2000 evenly spaced points on the interval $y \in [-10, 10]$ and $p_y \in [-2.5, 2.5]$. The LDs method uses $\tau = 60$.

Utilising the same 2000×2000 grid of ICs, as implemented in Fig. 4.4, together with the LD gradient method described in Sect. 3.6, the stable and unstable NHIMs can be extracted from the LDs computations. The NHIMs are extracted using points on the grid with a gradient greater than $d = 0.8$. This lower bound is selected to ensure that all manifolds, seen in Fig. 4.4, are extracted. The stable manifolds are represented by blue curves, while the unstable manifolds are exhibited in red. The results are shown in Fig. 4.5, where the plot in panel (a) showcases the stable NHIMs, Fig. 4.5(b) demonstrates the unstable NHIMs, while in Fig. 4.5(c) we present a depiction of the superposition of the stable and unstable NHIMs. The superposition of the manifolds depicts the various lobe structures created by the NHIMs, which will be examined in the remainder of this chapter. The stable manifolds converge towards the unstable fixed points whereas the unstable manifolds diverge. Displaying the manifolds separately assists in defining certain areas in phase space, according to the NHIMs which enclose certain regions, and also helps in understanding their specific influence on the outcome of various orbits. An additional reason that we make this distinction is because it was shown in [86] that the forward integration of orbits which begin in the interior region of configuration space are guided toward the Lyapunov orbit by means of the stable manifolds. Afterward these trajectories reach the periodic orbits, they diverge through the influence of the unstable NHIMs.

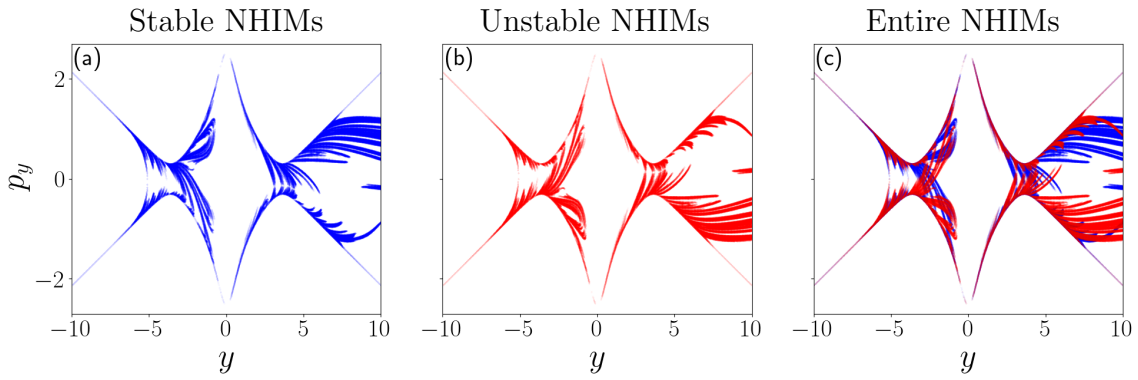

Figure 4.5: Figures which exhibit the extracted NHIMs from Fig. 4.4, by using the LD gradient method with gradients which are greater than $d = 0.8$. The same energy, pattern speed, grid size, and integration time as in Fig. 4.4 have been used. The panels in this figure present (a) the stable manifolds, (b) the unstable manifolds, and (c) both stable and unstable manifolds superimposed onto each other.

4.3 Influence of the stable normally hyperbolic invariant manifolds

As the previous section introduced the lobes found in the plane defined by $x = 0$ and $p_x > 0$, we now wish to examine the influence of the NHIMs on the flow of trajectories for the dynamical system. In particular, we wish to observe various dynamical features, defined by forward time integration, within the central region (between L_1 and L_2). We shall then compare regions of different dynamical traits with the stable manifolds. The features which will be investigated include: the duration required for an orbit to escape the central region, the time span it remains outside the central region within a given time interval, and the frequency of orbit re-entries into the central region. It is important to note that this section deals with the forward temporal evolution, but a similar analysis can be conducted for the backward temporal evolution. Additionally, through the observation of Fig. 4.5 it is seen that there exists a symmetry between the stable and unstable NHIMS. If one is reflected about the $p_y = 0$ axis, the other is obtained. It was shown in [86] that, in the case of forward time integration, the stable manifolds guide orbits from the central region of the system to the Lyapunov orbits. In backward time integration, the unstable manifolds fulfill this role. Thus, due to the symmetry of the manifolds and their influence on an orbit's flow, all results in this section can be reflected about the $p_y = 0$ axis for backward temporal evolution.

Utilising the definition of an escape, described in Sect. 4.1, we first investigate the time taken for an orbit to escape the central region. To do so, we populated the PSS by implementing a grid of 2000×2000 evenly spaced ICs, over the interval $y \in [-4.12, 4.12]$ (from the Lyapunov orbit surrounding L_1 to that surrounding L_2) and $p_y \in [-2.6, 2.6]$ (just past the energetically forbidden region). The temporal evolution of these particles is found for $\tau = 1071$ time units, which is approxim-

ately equivalent to 5Gyrs (where a gigayear is approximately $3.1516 \times 10^{16} s$). By integrating particles forward in time, we were able to separate the orbits into four distinct categories shown in Fig. 4.6(a): those that escaped before $\tau = 100$ (depicted by red points), those that escaped in the interval $100 < \tau \leq 500$ (shown as green points), those that escaped in the interval $500 < \tau \leq 1071 \approx 5$Gyrs (displayed as blue points), and the orbits that did not escape (indicated by grey points). Orbits which do not escape are either regular in motion or have not had sufficient time to escape. To demonstrate that the stable NHIMs influence the particles' trajectories, we superimposed in Fig. 4.6(b) a portion of these manifolds (shown as black curves) onto an enlarged region of Fig. 4.6(a). The subspace is seen over the intervals $y \in [-3, -0.25]$ and $p_y \in [0, 2.6]$. The stable manifolds are found using the p-'norm' LDs method with $\tau = 60$ and are obtained by considering all points with a gradient greater than $d = 0.8$ [which is the same as seen in Fig. 4.5(a)].

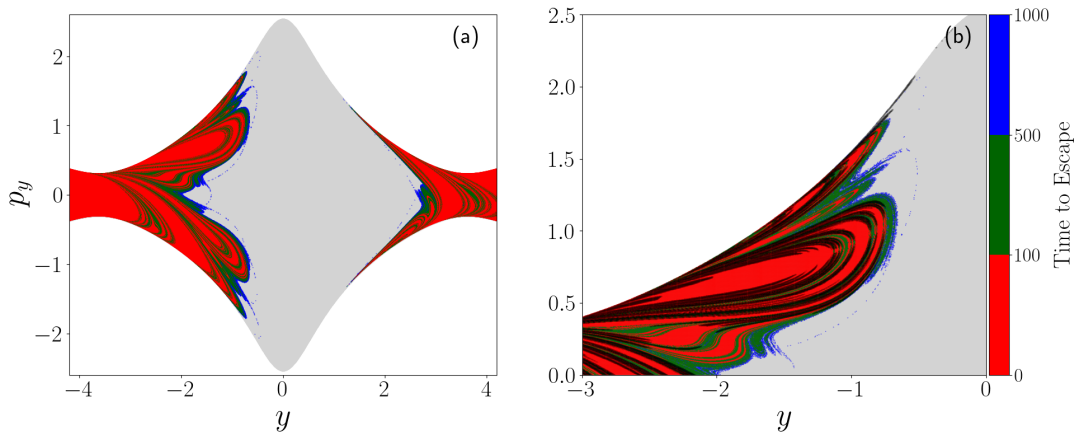

Figure 4.6: ICs coloured according to the time needed to escape the interior region in configuration space. Either the orbits escape in the time interval $0 < \tau \leq 100$ (red points), $1000 < \tau \leq 500$ (green points), or $500 < \tau \leq 1071 \approx 5$Gyrs (blue points). Those trajectories which do not escape over this period of time, are displayed by colouring their ICs grey, and the white areas are the energetically forbidden regions. Panel (a) is created using an equidistant grid of 2000×2000 ICs, over the interval $y \in [-4.2, 4.2]$ and $p_y \in [-2.6, 2.6]$. Panel (b) presents a small region of (a), $y \in [-3, -0.25]$ and $p_y \in [0, 2.6]$, along with the stable NHIMs superimposed as black curves. The stable manifolds are found using the forward p-'norm' LDs method, (3.62), with $\tau = 60$ over the interval $y \in [-3, -0.25]$ and $p_y \in [0, 2.6]$ of 2000×2000 evenly spaced ICs. The manifolds are extracted from the LDs scalar field by using the gradient method for all ICs, with a gradient greater than $d = 0.8$.

To demonstrate the symmetry of the stable and unstable manifolds, we produce in Fig. 4.7 the same plot as seen in Fig. 4.6(a), but instead integrate the orbits backward in time. We clearly see that Fig. 4.7 is a reflection of Fig. 4.6 about the $p_y = 0$ axis. Thus, for the remained of this section, we only present the forward integration time cases.

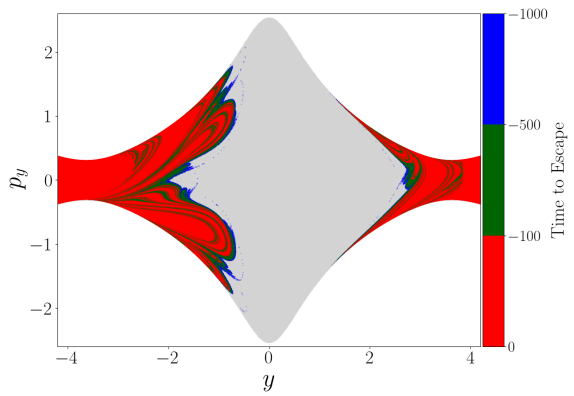

Figure 4.7: Similar to Fig. 4.6, but for orbits which are instead integrated backward in time.

It is important to note that only the chaotic orbits escape and are therefore categorised by the different colours in Figs. 4.6 and Fig. 4.7. It is worth noting that the regions in white in both figures are the energetically forbidden regions. The goal of these plots is to show the different regions corresponding to the length of integration time required, by an orbit, to escape. Additionally, we wish to show that these regions can be defined by the stable NHIMs found using the p-'norm' LDs method with $\tau = 60$. Due to the short integration time to reveal the stable manifolds, not all orbits that form the NHIMs have had time to converge. Meaning that some of the intricate manifolds are incomplete. However, we see that the manifolds that are extracted from the LDs method separate regions of the same colour. There are, however, some stable manifolds which do not act as boundaries between distinct colour regions. The reason for a lack of stable NHIIMs at these boundaries is because we have predefined three different time intervals of escape (blue, green, and red points). The time taken for an orbit to escape generates lobes which are more complex than those created by these three intervals, but the stable NHIMs are able to correctly distinguish these regions. The reason that the stable manifolds have an impact on the time taken for an orbit to escape is because they are intertwined, as discussed in [92]. The intricate interconnection follows from the fact that the manifolds of our 4D system are three dimensional structures, encapsulating the flow of the system within their confines. Consequently, if the manifolds' structure is convoluted, it can cause the trajectory of a particle to follow a lengthy and intricate path. Hence, the time required for an orbit to escape is increased.

Not only do the stable manifolds determine the time an orbit takes to escape, they can also be used to study additional dynamical phenomena. Further behaviour includes the regulation of trajectories which spend different amounts of time in the exterior region in the configuration space, once an orbit has escaped. Time is counted while the particle is outside of the central region. The timer is stopped if the orbit re-enters the central region, but it resumes if the orbit escapes again. This continues until the final integration time is met. An additional feature which

is registered is the number of times an orbit escapes from the central region over a time interval. In order to showcase these features, a similar setup as the one for Fig. 4.6 is used. Once again, the ICs are integrated forward in time for a period equivalent to 5Gyrs ($\tau = 1071$). An orbit is classified as escaped once it exits the central region, as discussed for the creation of Fig. 4.3, and the trajectory enters the central region through the lower most point of the Lyapunov orbits surrounding L_1 or L_2. The results for the amount of time spent outside of the central region in configuration space is shown in Fig. 4.8(a), where the colourbar represents the integration time, τ. The number of escapes experienced by various trajectories is depicted in Fig. 4.8(b), where a particle has either escaped the central region once or twice (shown in purple) or more than twice (shown in light blue).

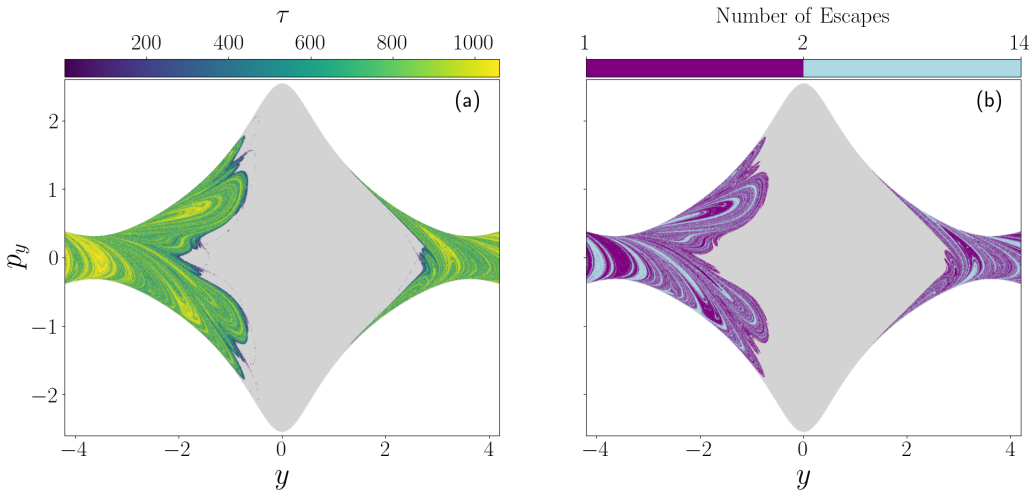

Figure 4.8: ICs of the system (4.1) with $z = \dot{z} = 0$, coloured according to (a) the length of time the related orbits spend outside of the central region in configuration space for a temporal evolution of $\tau = 1071$, and (b) the number of escapes that a trajectory experiences after being integrated forward in time for $\tau = 1071$. ICs are chosen from a grid of 2000×2000 evenly spaced points on the $y - p_y$ plane, the y interval is from one Lyapunov orbit value to the other and the $p_y \in [-2.8, 2.8]$. The grey regions correspond to orbits which did not escape during this time interval, while white areas correspond to energetically forbidden regions.

From the results of Fig. 4.8, the lobe structure is seen to influence the length of time that an orbit remains in the exterior region in configuration space and the number of times a trajectory escapes the central region. Additionally, these structures are similar to that seen in the result describing the required time for an escape (Fig. 4.6). The only difference between Fig. 4.6 and Fig. 4.8 is that the latter results present more intricate lobe structures. The time taken to escape was separated into three distinct intervals which resulted in some of the intricacies within each of these intervals being lost in Fig. 4.8. The regions portrayed by different colours (different lobes) are still associated with the stable NHIMs. Once again, if the processes were repeated for the backward integration, with the same

final time, the resulting figures would be the reflection of Fig. 4.8 about the p_y axis, as the dynamics would be governed by the unstable invariant manifolds.

4.4 Dynamical behaviour associated with both the stable and unstable normally hyperbolic invariant manifolds

It was stated in [85] that a *homoclinic* orbit is one that escapes past an unstable periodic orbit, via one of the openings between the energetically forbidden regions, and then asymptotically returns to the same opening. On the other hand, if an orbit departs from one of the openings and asymptotically enters through the other, it was defined as *heteroclinic*. Furthermore, in that paper the authors studied the effect of parameter changes on the shape of the invariant manifolds in their galactic type Hamiltonian, and found that the manifolds create ring and spiral structures. The reason this is of interest is because morphologically, it is important to understand where a star comes from and where it goes.

Numerically determining the opening that an orbit escapes from requires forward in time integration until the escape criterion is met, and if a trajectory is integrated backward in time, it is possible to obtain the opening from which the orbit entered the central region. Utilising this approach, one can then colour ICs of orbits according to whether they are homoclinic or heteroclinic, and examine the different structures created by the two types of orbits. We implement this method for our system, with an initial grid that is the same as in Fig. 4.6, for an integration time equivalent to 1.35Gyrs (which is approximately $\tau = 289$) or until an escape/entrance occurs. We no longer use $\tau = 1071$, because the larger integration time leads to orbits diverging large distances in configuration space. We found that this smaller integration time results in orbits which form pronounced structures in the configuration space. The result can be seen in Fig. 4.9(b). In this plot, we also indicate (by means of a legend) the percentage of ICs which produced orbits that are either homoclinic or heteroclinic. This result in isolation can be of interest, as it may be useful to observe the various galactic morphologies created by orbits with different escape properties.

However, the scrutiny of different pattern speeds means that a comparison between different lobe structures and the associated morphologies can be done. It is beneficial to keep the opening of the energetically forbidden regions constant when examining the effect of varying rotational velocities, as different openings of these regions can lead to skewed results. This means that one cannot simply alter the pattern speed in isolation. For this reason, it is pertinent to find an energy which leads to an opening with, more or less, the same opening size as the initial case. Such an energy is obtained by noticing that the position of the L_1 and L_2 Lagrange points will differ depending on the selected pattern speed, meaning that the system will begin to experience openings of the energetically forbidden regions at varying

positions in space. To find the energy level, for different pattern speeds, which allows for approximately the same size opening as our original case, we can begin by finding the relative energy difference between the currently studied configuration and its unstable Lagrange points, as follows

$$E_{\text{rel}} = \frac{E_L - E}{E_L}, \tag{4.10}$$

where E_{rel} is the relative energy difference, E_L is the energy at the unstable Lagrange points and E is the chosen energy ($E = -4.20$ for the initial system). Using the result from (4.10), we are able to find the appropriate energy level for different values of the pattern speed by

$$E = E_L - E_{\text{rel}} \cdot E_L, \tag{4.11}$$

where we find the energy at the unstable Lagrange points for an Ω_b value of our choice and implement the previously calculated E_{rel}.

Two additional pattern speeds have been selected for a more holistic comparison, one which is greater ($\Omega_b = 70\,\text{km}\,\text{s}^{-1}\,\text{kpc}^{-1}$) than the original pattern speed and a pattern speed less ($\Omega_b = 45\,\text{km}\,\text{s}^{-1}\,\text{kpc}^{-1}$) than the original ($\Omega_b = 60\,\text{km}\,\text{s}^{-1}\,\text{kpc}^{-1}$), which leads to energies of the system of $E \approx -4.37$ and $E \approx -3.91$, respectively. Using the interval of $p_y \in [-2.8, 2.8]$ and y up to the Lyapunov values of the faster and slower pattern speeds ($y \approx \pm 3.58$ and $y \approx \pm 5.58$ respectively) with the same integration time as before ($\tau = 1071$, which is equivalent to 1.35Gyrs), yields the results respectively seen in Figs. 4.9(a) and (c).

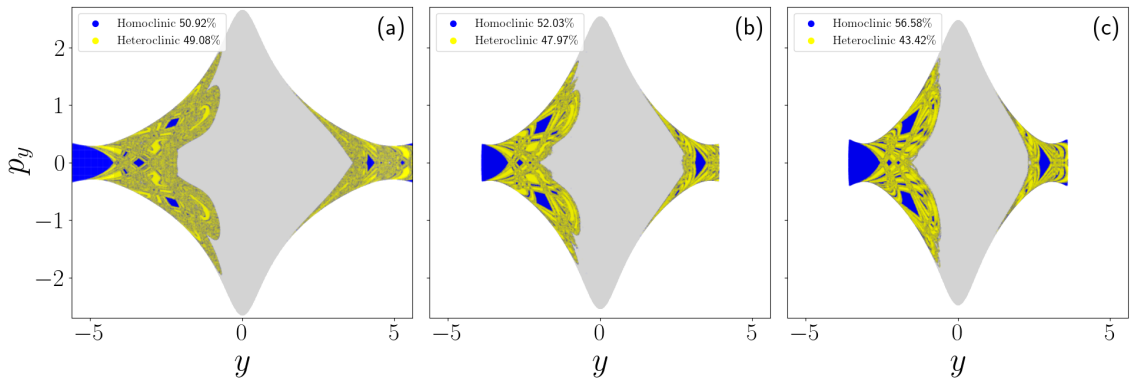

Figure 4.9: Regions of homoclinic (shown in yellow) and heteroclinic (shown in blue) orbits (see text for the definition of these terms) for a grid of 2000×2000 equidistant ICs over the interval $p_y \in [-2.8, 2.8]$ and y from one Lyapunov orbit to the other. All results pertain to the Hamiltonian system (4.1) with $z = \dot{z} = 0$, for (a) an energy of $H = -3.91$ and a pattern speed of $\Omega_b = 45\,\text{km}\,\text{s}^{-1}\,\text{kpc}^{-1}$, (b) $H = -4.2$ and $\Omega_b = 60\,\text{km}\,\text{s}^{-1}\,\text{kpc}^{-1}$, and (c) $H = -4.37$ and $\Omega_b = 70\,\text{km}\,\text{s}^{-1}\,\text{kpc}^{-1}$. The grey regions represent orbits which did not escape when integrated forward and backward in time for $\tau = 289 \approx 1.35$Gyrs.

The results seen in Fig. 4.9 are displayed over the same set of axis to showcase the differing sizes in the central region. Through an examination of the figures, it can easily be seen that as the pattern speed increases, the energy required for the same sized opening decreases, and the blue and yellow coloured regions become less mixed. Thus, as the energy is decreased, regions having the same dynamical behaviour increase in size. Additionally, the percentage of homoclinic orbits increases with a decrease in the size of the central region. This means that as larger regions of orbits which display similar dynamical behaviour appear, we witness more orbits entering and escaping through the same opening between the energetically forbidden regions.

In order to investigate the possible effect that the opening size of the energetically forbidden regions has on the system's dynamics when the pattern speed is kept constant, we reduce the dynamical system's energy. The reduction of the energy reduces the size of the opening. In order to demonstrate this result we use an energy of $H = -4.235$ and the same pattern speed of the originally considered system, $\Omega_b = 60\,\mathrm{km\,s^{-1}\,kpc^{-1}}$. The outcome of this process is seen in Fig. 4.10 where results are calculated over the same p_y interval and a different y interval with respect to Fig. 4.9(b), as the positions of the Lyapunov orbits have changed to $y \approx -3.91$ and $y \approx 3.91$. However, we notice that Fig. 4.10 shows an increased sensitivity of the dynamical evolution depending on the location of an IC. This is an opposite effect compared to the results seen in Fig. 4.9, where we examined a change of pattern speeds.

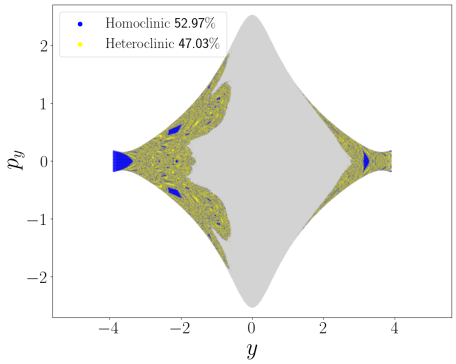

Figure 4.10: Similar to Fig. 4.9, but for an energy of $H = -4.235$ and the same pattern speed as Fig. 4.9(b) ($\Omega_b = 60\,\mathrm{km\,s^{-1}\,kpc^{-1}}$), which results in a smaller opening between the energetically forbidden regions.

As a change in the regions of different dynamical behaviours has been seen with respect to a corresponding alteration of the pattern speed and energy, a natural question to then ask is: How do the manifolds, as seen by the LDs method, differ due to these changes? To answer this question, the p-'norm' LDs method (3.57) can be used for the same grid sizes and coordinate ranges as used in Fig. 4.9 and Fig. 4.10, along with a final integration time of $\tau = 60$. The results for the LDs method are presented in Fig. 4.11, with the three panels ordered in ascending pattern speed,

and in Fig. 4.12, for a smaller opening between the energetically forbidden regions. The results, of Fig. 4.11, demonstrate that an increase in pattern speed (decrease in energy), leads to the amount and intricacy of the manifolds increasing. The reason that we change the energy level along with the pattern speed is to ensure that the openings between the energetically forbidden regions remain almost the same for all cases, which was discussed just above equation (4.10). This allows us to examine the effects of the pattern speed in isolation. Thus, if the LDs figures are observed in isolation, one can understand the relative increase or decrease in the size of regions which display the same dynamical behaviour. A relative increase in the amount and intricacy of the NHIMs (seen as the dark blue lines in Fig. 4.11, which can also be seen by extracting the NHIMs) means that there are more strict boundaries governing the phase space transport of particles which leads to a decrease in sensitivity on the location of an IC, and vice versa. A similar result is seen when examining the manifolds associated with the system containing different sized openings between the energetically forbidden regions but the same pattern speed [Fig. 4.11(b) and Fig. 4.12]. There are more manifolds for the larger opening [Fig. 4.11(b)] and they are better defined. This results in less mixing of the homoclinic and heteroclinic orbits.

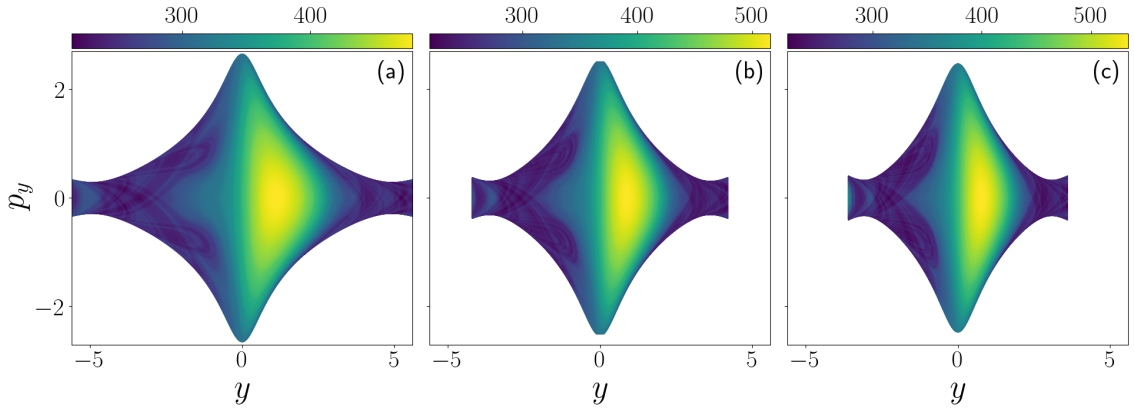

Figure 4.11: The (y, p_y) space of the Hamiltonian system of galactic type given in (4.1) with $z = \dot{z} = 0$, where points are coloured according to their p-'norm' LD value, (3.57). All results are found using a grid of 2000×2000 ICs over the interval $p_y \in [-2.8, 2.8]$ and y from one Lyapunov orbit to the other, while the LDs method uses $\tau = 60$. Panel (a) demonstrates the results for the smallest pattern speed of $\Omega_b = 45\,\mathrm{km\,s^{-1}\,kpc^{-1}}$, with an energy of $H = -3.91$, (b) was created using a pattern speed of $\Omega_b = 60\,\mathrm{km\,s^{-1}\,kpc^{-1}}$ and an energy of $H = -4.20$, and (c) is for a pattern speed of $\Omega_b = 70\,\mathrm{km\,s^{-1}\,kpc^{-1}}$ and a corresponding energy of $H = -4.37$.

Returning our attention to the plots representing regions of homoclinic and heteroclinic orbits prompts a desire for a more in-depth analysis of the specific opening, between the energetically forbidden regions, through which an orbit escapes (found through the forward temporal evolution of orbits in the central region) and enters (seen as the backward trajectory). We call the opening near L_1 the upper opening

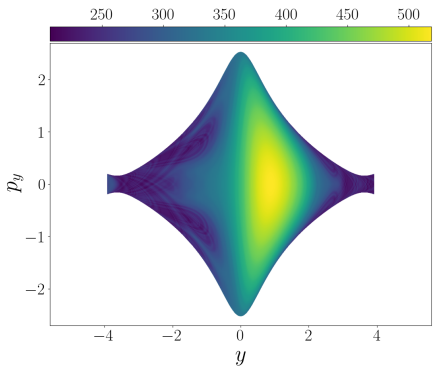

Figure 4.12: Similar results and set-up as those depicted in Fig. 4.11. However, this plot was created for an energy value of $H = -4.235$ and a pattern speed of $\Omega_b = 60\,\mathrm{km\,s^{-1}\,kpc^{-1}}$ of the Hamiltonian (4.1), when $z = \dot{z} = 0$ is considered.

and index it as 1. The opening close to L_2 is called the lower opening and is indexed as 2. If a trajectory experiences an escape in both the forward and backward temporal evolutions, we classify it according to the opening between the energetically forbidden region that it escaped from forward in time (called the trajectory's fate) and backward in time (the orbit's origin). Using this approach we create a colour map which is called the origin-fate map (OFM) and was first defined in [93], where the phase space transport in reactant-product type dynamical systems was examined. We then assign each IC an origin-fate index, which includes two numbers indicating first the origin and second the fate of a trajectory. This approach is easily implemented using the same y and p_y intervals as in Fig. 4.9 and Fig. 4.10 ($p_y \in [-2.8, 2.8]$ and y from the outermost point of one Lyapunov orbit to the other), for an equidistant grid of 2000×2000 ICs. Just as before, in Fig. 4.9 and Fig. 4.10, we integrate orbits forward and backward in time for $\tau = 289$ (which corresponds to about 1.355Gyrs), or until they escape. The results for the three different pattern speeds are shown in Fig. 4.13 and the results for the smaller opening are shown in Fig. 4.14.

As the pattern speed is increased in Fig. 4.13 [i.e., moving from panel (a) to (c)] it is seen that the regions of the same dynamical behaviour increases in size and the ocean of mixed coloured points decreases, which is in agreement with the results presented in Fig. 4.9. Comparing the effect of different openings [Fig. 4.13(b) and Fig. 4.14] yields the same conclusions as seen in the homoclinic and heteroclinic case [Fig. 4.9(b) and Fig. 4.10]. As the opening between the energetically forbidden regions is decreased in size (the energy is decreased) while the pattern speed is kept constant, the sensitivity of a trajectory on the location of the IC increases.

To observe the influence of the manifolds on the escape dynamics of orbits, we focus our attention to a portion of Fig. 4.13(b). This region of the system is shown in Fig. 4.15(a) ($y \in [-1.6, -0.8]$ and $p_y \in [0.3, 1.2]$), with a grid of 2000×2000 evenly spaced ICs The complicated structures of the various regions shown in this plot are superimposed with the manifolds of the system in Fig. 4.15(b), found by

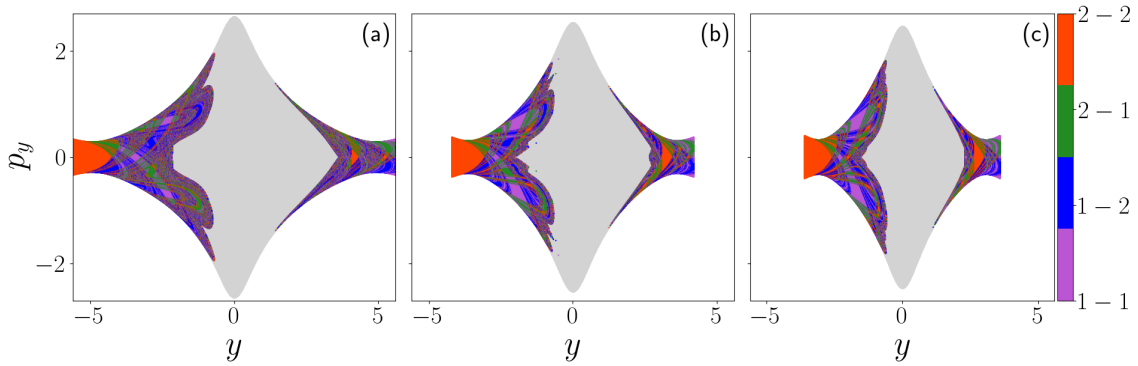

Figure 4.13: The OFM for the Hamiltonian system (4.1) (with $z = \dot{z} = 0$), on the PSS defined by $x = 0$ and $p_x > 0$. All results are calculated on the interval $p_y \in [-2.8, 2.8]$ and y from one Lyapunov orbit to the other, for the forward and backward time evolution of $\tau \approx 1.35$Gyrs. The white areas represent the energetically forbidden regions and the grey sections depict the orbits which did not escape over the considered time interval. The remaining points are coloured according to the origin-fate index, where the first number represents the opening between the energetically forbidden regions from which the orbit first escapes when evolved backward in time. The second number corresponds to the specific opening that an orbit first escaped through when evolved forward in time. The index 1 represents the upper opening in configuration space and 2 pertains to the lower opening. Panel (a) shows results for energy $H = -3.91$ and pattern speed $\Omega_b = 45\,\mathrm{km\,s^{-1}\,kpc^{-1}}$, we consider (b) $H = -4.2$ and $\Omega_b = 60\,\mathrm{km\,s^{-1}\,kpc^{-1}}$, while in (c) we have $H = -4.37$ and $\Omega_b = 70\,\mathrm{km\,s^{-1}\,kpc^{-1}}$.

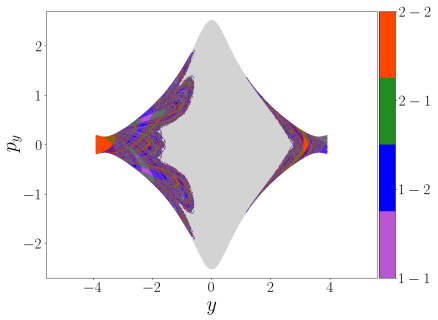

Figure 4.14: Using the same conditions and integration time as Fig. 4.13, we show the results for the OFM of the 2 dof version ($z = \dot{z} = 0$) of Hamiltonian (4.1) with $H = -4.235$ and $\Omega_b = 60\,\mathrm{km\,s^{-1}\,kpc^{-1}}$.

using the p-'norm' LDs gradient method, where $\|\nabla M_p(x_0, t_0, \tau)\| > d$ with $d = 0.8$ (in a similar manner to Fig. 3.9). These manifolds are found using an equidistant grid of 2000×2000 ICs over the same region, integrated for $\tau = 60$. Going further in time, more intricate manifolds will be revealed and will overpopulate this figure, thus a shorter τ value is used to correctly reveal the NHIMs.

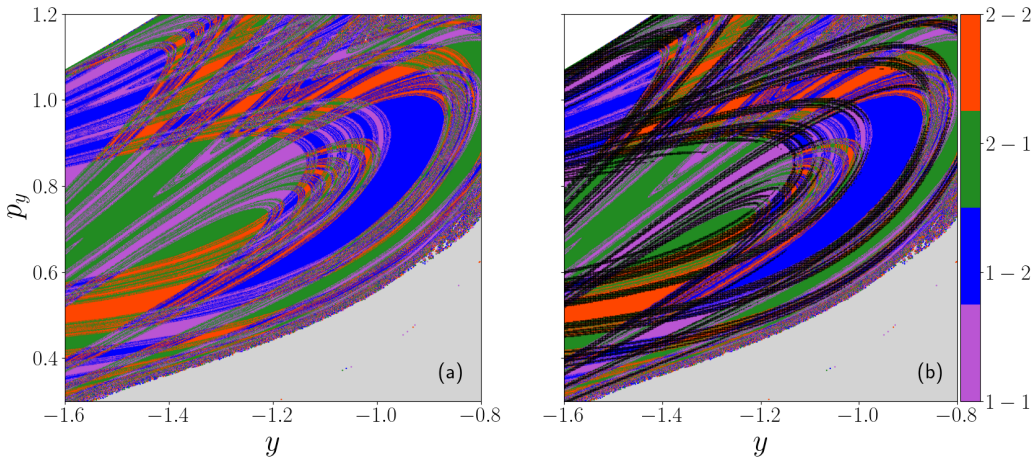

Figure 4.15: An enlargement of Fig. 4.13(b) over the interval $y \in [-1.6, -0.8]$ and $p_y \in [0.3, 1.2]$. This area is populated with 2000×2000 ICs to ensure a detailed plot shown in (a). Panel (b) presents the NHIMs superimposed onto the results of (a). The manifolds are found by implementing the p-'norm' LDs method, (3.57) with $\tau = 60$. These manifolds are then extracted from the LD scalar field by implementing the gradient method (3.61) with all points having a gradient larger than $d = 0.8$.

4.5 Morphological structures

There are many different ring and spiral structures associated with different galaxies, some of which can be seen in Chapt. 5 of [94]. In Sect. 4.1, we stated that the research conducted in our current chapter was inspired by the work done in [85, 86, 87, 88], as it was argued that ring and spiral structures are populated by orbits guided by the NHIMs. This section looks at the various dynamical phenomena discussed throughout this chapter, exploring the galactic morphological structures associated with different phase space regions and how the formations change as the pattern speed and energy is varied. These phase space regions are separated by the NHIMs and the aim is to determine the influence of these dividing structures on orbit behaviour, resulting in distinct galactic features.

In Sect. 4.3, we observed dynamical traits of trajectories associated with either the stable or unstable manifolds, such as the time taken for an orbit to escape (Fig. 4.6) the time that an orbit spends in the exterior region in configuration space [Fig. 4.8(a)] and how many times a star escapes over a period of time [Fig. 4.8(b)]. In all three of these plots, we saw approximately equivalent regions defined by the stable manifolds. Thus, we shall view only the morphologies associated with the phase space regions defined only by one of these results: the number of times that an orbit escapes over a time of $\tau = 1071$ [Fig. 4.8(b)]. The ICs of orbits which escaped on more than two occasions are depicted in light blue in Fig. 4.8(b) and those that escaped either once or twice are shown in purple. To present the supported real space morphologies, we integrate the purple and blue orbits forward

in time and show only their final position in configuration space in Figs. 4.16(a) and (b), respectively. To compare the two results, we superimpose these two panels in Fig. 4.16(c). However, we do not integrate the orbits for the full 5Gyrs ($\tau = 1071$) as it leads to a large portion of the orbits diverging, leading them to travel far away from the openings between the energetically forbidden regions from where they escaped. Consequently, we found that an integration time of $\tau = 289$ (approximately 1.35Gyrs) leads to the majority of trajectories remaining in the proximity of the system's origin and revealing appropriate morphologies. Note that in all panels of Fig. 4.16 the energetically forbidden regions are depicted in grey. Additionally, the desire to observe only the relevant structures gives rise to the figures being displayed in the range $x, y \in [-13, 13]$[1], as all orbits outside of this area do not contribute to the ring and spiral structures in our investigation.

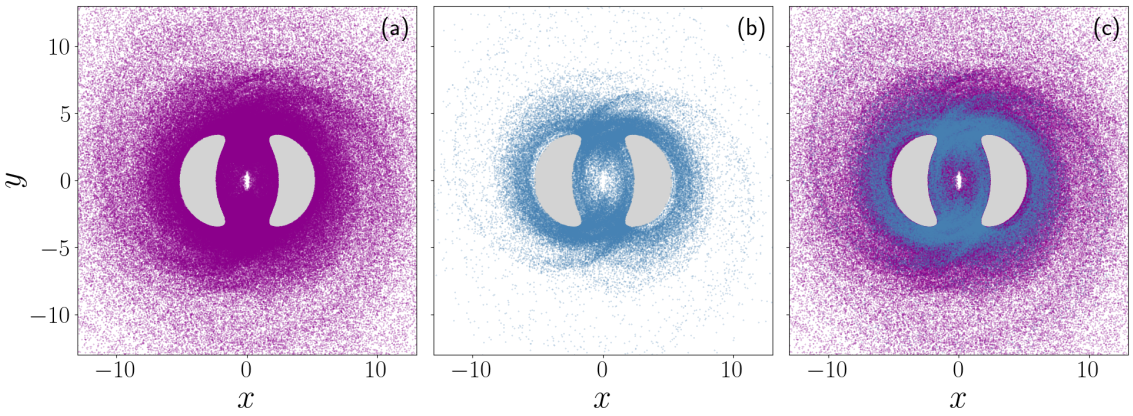

Figure 4.16: The final positions, after a forward integration time of $\tau = 289 (\approx$ 1.35Gyrs), of the orbits from the two regions described by Fig. 4.8(b). Panel (a) presents the orbits which escaped either once or twice after a time equivalent to 1.35Gyrs. Whereas, panel (b) showcases the final positions of orbits which escaped more than twice in the same time interval. Panel (c) shows the superposition of (b) onto (a).

The first difference that is seen when comparing Fig. 4.16(a) and Fig. 4.16(b) is that (b) has a lot fewer stars present at time $\tau = 289$. This is because the majority of trajectories escape either once or twice, as seen in Fig. 4.8(b). As a result of the majority of escaping orbits being depicted in Fig. 4.16(a), the morphological structure surrounding the energetically forbidden regions are more pronounced. From Fig. 4.16(c), it is seen that the structures created by the two sets of orbits are similar near the energetically forbidden regions, although purple coloured particles dominate in further away areas.

Implementing the same approach used in Fig. 4.16, the morphological features associated with the homoclinic and heteroclinic orbits (Fig. 4.9 and Fig. 4.10), as

[1]This creates an area of $(26\text{kpc})^2$, which is an appropriate scale to view the Milky Way galaxy which has a diameter of 26.8±1.1kpc as given in https://www.detailedpedia.com/wiki-Milky_Way.

well as those relating to the OFM (Fig. 4.13 and Fig. 4.14) can be investigated. This involves the forward integration of all trajectories for $\tau = 289$ (1.35Gyrs) and the presentation of their final position of the orbits in configuration space. The reason that we only present the forward time evolution and not the backward, is a result of the symmetry between the stable and unstable NHIMs seen in Fig. 4.4. This symmetry shows that the unstable manifolds are a reflection of the stable manifolds about the $p_y = 0$ axis.

We shall examine the morphologies supported by the Hamiltonian system, associated with the aforementioned orbit classification, for the different pattern speeds ($\Omega_b = 45\,\mathrm{km\,s^{-1}\,kpc^{-1}}$, $\Omega_b = 60\,\mathrm{km\,s^{-1}\,kpc^{-1}}$, and $\Omega_b = 70\,\mathrm{km\,s^{-1}\,kpc^{-1}}$) and different sized openings between the energetically forbidden regions for $\Omega_b = 60\,\mathrm{km\,s^{-1}\,kpc^{-1}}$ ($H = -4.2$ and $H = -4.235$). The results are presented in Fig. 4.17, where the top row [Figs. 4.17(a)–(f)] contains the results for $\Omega_b = 45\,\mathrm{km\,s^{-1}\,kpc^{-1}}$ and $H = -3.91$. The Figs. 4.17(g)–(l) depict the structures for $\Omega_b = 60\,\mathrm{km\,s^{-1}\,kpc^{-1}}$ and $H = -4.2$. The third row of Fig. 4.17 [panels (m)–(r)] correspond to the case $\Omega_b = 60\,\mathrm{km\,s^{-1}\,kpc^{-1}}$ and $H = -4.235$, while Figs. 4.17(s)–(x) display the morphologies of the system with $\Omega_b = 70\,\mathrm{km\,s^{-1}\,kpc^{-1}}$ and $H = -4.37$. The columns of Fig. 4.17 relate to a particular orbit classification, which is labeled at the top of each column in the plot. Four of the columns pertain to the OFM and are indicated by their origin-fate index. We recall that the origin-fate index describes first which opening of the energetically forbidden region the orbit escapes from in the backward time evolution, its origin, and then where the trajectory escapes from in forward time, its fate. The numbers 1 and 2 correspond to the opening near the Lyapunov orbits surrounding L_1 and L_2, respectively. The remaining two columns show the morphologies for orbits which escape through the same opening, for both forward and backward time integration (this is the superposition of 1–1 and 2–2 orbits, and are the homoclinic orbits), and orbits which escape from different regions (the superposition of the 1–2 and 2–1 orbits, and are the heteroclinic orbits).

To create the plots seen in Fig. 4.17 we integrated orbits associated with different classifications forward in time. As a result of the forward temporal evolution, we found that the stable NHIMs were the main influence in guiding trajectories. This effect is evident when comparing the results pertaining to the orbits which display different dynamical traits, as described by the OFM. Specifically, we refer to the first, second, fourth, and fifth columns for each individual energy level (seen as the different rows). Our examination reveals that the galactic morphologies created by the 1-1 and 2-1 orbits are approximately equivalent, as are those resulting from the 2-2 and 1-2 orbits. Conversely, if the backward temporal evolution is considered, the inverse effect occurs: the structures would be determined by the trajectories governed by the unstable manifolds, such that the 1-1 and 1-2 orbits would lead to similar structures in configuration space, just as the 2-2 and 2-1 trajectories do. Since the objects created by the 1-1 and 2-2 orbits (together they are the homoclinic orbits) closely resemble those formed by the 2-1 and 1-2 orbits (the combination of these trajectories are the heteroclinic orbits), respectively, the homoclinic and heteroclinic trajectories are seen to be roughly the same.

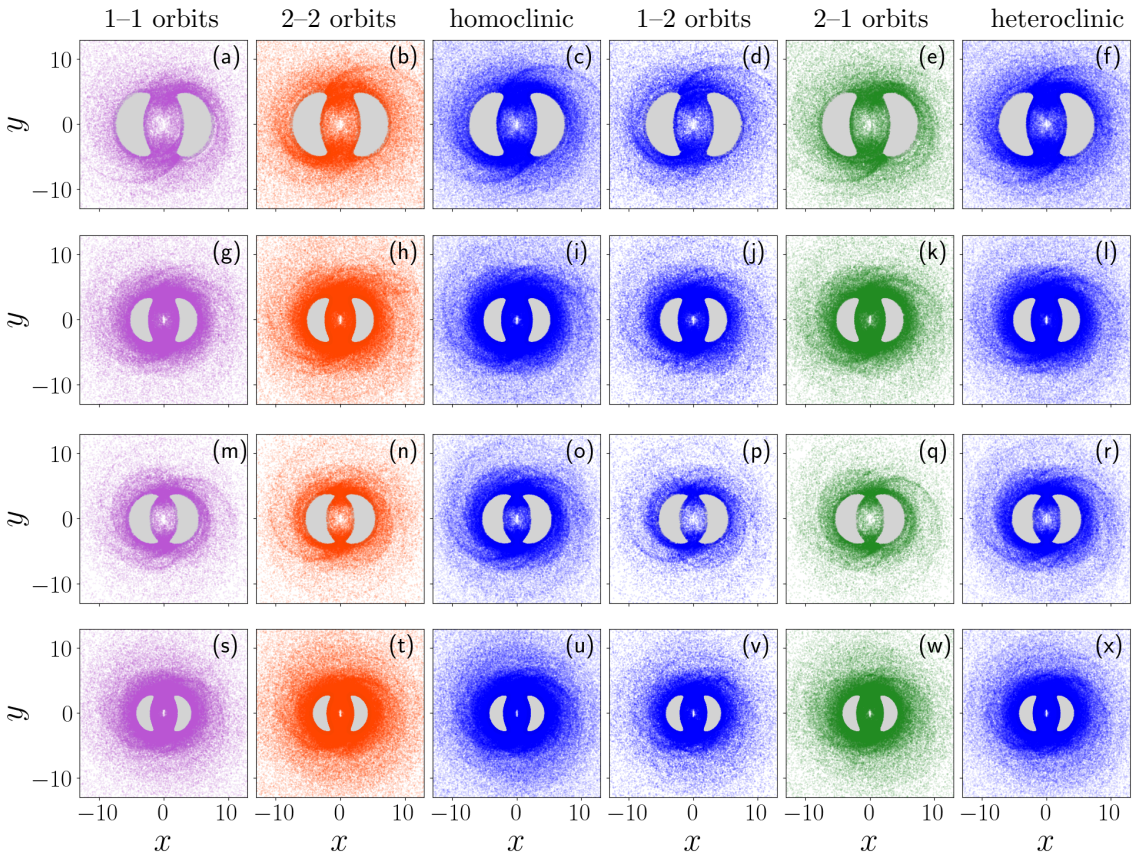

Figure 4.17: The final positions of stars, with different dynamical traits, whose trajectories have been evolved forward in time up until $\tau = 289 (\approx 1.35\text{Gyrs})$. Columns 1, 2, 4, and 5 showcase the results pertaining to various regions from the OFM results (Fig. 4.13 and Fig. 4.14). Columns 3 and 6 present the outcomes for homoclinic and heteroclinic orbits respectively, as discussed in Fig. 4.9 and Fig. 4.10. Panels (a) to (f) showcase the structures of the Hamiltonian system (4.1) (for $z = \dot{z} = 0$) with a pattern speed of $\Omega_b = 45\,\mathrm{km\,s^{-1}\,kpc^{-1}}$ and an energy of $H = -3.91$. The second row [panels (g) to (l)] displays the same dynamical system but with $\Omega_b = 60\,\mathrm{km\,s^{-1}\,kpc^{-1}}$ and $H = -4.2$, while the third row [panels (m) to (r)] correspond to the same pattern speed but for an energy $H = -4.235$. The final row [panels (s) to (x)] incorporates $H = -4.37$ and $\Omega_b = 70\,\mathrm{km\,s^{-1}\,kpc^{-1}}$. Additionally, the grey regions in all plots correspond to the respective system's energetically forbidden region. All plots are shown over the intervals $x, y \in [-13, 13]$.

Figure 4.17 allows us to examine the different structures associated with various pattern speeds. The lowest pattern speed of $\Omega_b = 45\,\mathrm{km\,s^{-1}\,kpc^{-1}}$ [Figs. 4.17(a) to (f)] leads to the creation of spiral like features which are more pronounced or disconnected from the central region, whereas the largest rotational velocity of $\Omega_b = 70\,\mathrm{km\,s^{-1}\,kpc^{-1}}$ [Figs. 4.17(s)–(x)] results in more circular structures surrounding the energetically forbidden regions. The features resulting from a pattern speed of $\Omega_b = 60\,\mathrm{km\,s^{-1}\,kpc^{-1}}$, with approximately the same size openings of the

energetically forbidden regions as the two previous values of Ω_b, are presented in Figs. 4.17(g) to (l). Here we see spiral like features which are less pronounced than those in Figs. 4.17(a) to (f), but are not as circular as those in Figs. 4.17(s)–(x). We can additionally compare the morphologies arising from the planar ($z = \dot{z} = 0$) version of the system (4.1), with the same pattern speed ($\Omega_b = 60\,\mathrm{km\,s^{-1}\,kpc^{-1}}$) but different energy levels, $H = -4.2$ [Figs. 4.17(g) to (l)] and $H = -4.235$ [Figs. 4.17(m)–(r)]. Initially, it is seen that there are more stars present in the results for the higher energy level. This is due to the fact that the openings of the energetically forbidden regions (depicted as the grey crescent shapes) are relatively larger. The wider opening implies that there is additional space for the trajectories to more easily escape. Consequently, there are more trajectories which are classified by the OFM, as well as more homoclinic and heteroclinic orbits. Although there are fewer stars in Figs. 4.17(m)–(r), the spiral like features are almost the same as those seen in Figs. 4.17(g) to (l). We can conclude that in this system, there is a stronger dependency on pattern speed instead of energy level when determining the galactic structures.

It is also important to discuss the impact of qualitative mixing on the different structures. We first observed the influence of an increase in pattern speed for similar sized openings between the energetically forbidden regions resulting in a decrease in sensitivity of the dynamical evolution on the location of an IC, as showcased in Fig. 4.9 and Fig. 4.13. By examining Fig. 4.17, it is seen that an increase in mixing of various dynamical traits corresponds to more pronounced spiral-like morphologies [Figs. 4.17(a)–(f)], whereas a decrease in complexity results in the structure being circular-like [Figs. 4.17(s)–(x)]. The same cannot be said about the mixing of dynamical traits when the pattern speed is kept constant but the energy is changed. This is because the structures seen in Figs. 4.17(g) to (l) and Figs. 4.17(m) to (r) are approximately equivalent.

4.6 Summary

In this chapter, we initially introduced the 3D and 2D forms of a galactic type Hamiltonian system. The rationale for presenting this system was to analyse the influence of NHIMs on potential orbital morphologies. We first described particular regions of this system which are useful in determining and understanding escapes from the galaxy's central region. The description of the pertinent structures was followed by an introduction of a criterion, which allows one to numerically determine whether an orbit has escaped the central region through the openings between the energetically forbidden regions. This criterion was formulated such that it is applicable to all energy levels between the energy of the system's unstable fixed points and of the local maxima of the potential function. By implementing this criterion, we were able to examine how the structures of the stable NHIMs influence the length of time required for a chaotic orbit to escape the central region, the

fraction of time that a trajectory spent outside of this region, and the frequency of orbits escaping from this region.

As the stable manifolds only impact the forward temporal evolution of trajectories, we then wanted to observe dynamical phenomena associated with phase space regions that are separate by both the stable and unstable manifolds. The reason for our interest in such regions is because the unstable manifolds guide orbits in the backward time, enabling us to know the origin of an orbit. On the other hand, the stable manifolds, associated with forward time integration, informs us of a trajectory's fate. The first orbital classification that we made with respect to regions enclosed by both the stable and unstable NHIMs was to differentiate between orbits whose origin and fate indices are the same (homoclinic orbits) and trajectories that escape from one opening when evolved forward in time and another when integrated backward in time (heteroclinic orbits). We studied these dynamical traits for three different pattern speeds ($\Omega_b = 45\,\mathrm{km\,s^{-1}\,kpc^{-1}}$, $\Omega_b = 60\,\mathrm{km\,s^{-1}\,kpc^{-1}}$, and $\Omega_b = 70\,\mathrm{km\,s^{-1}\,kpc^{-1}}$), with approximately the same size openings of the energetically forbidden regions. This required us to change the energy associated with each Ω_b value, to determine only the effects of a change in rotational velocity. The results indicated that the variation of pattern speed affected the size of regions displaying the same orbital classification, with an increase of pattern speed resulting in larger areas of orbits of the same type.

Additionally, we compared the results of two different energy levels ($H = -4.2$ and $H = -4.235$) for the same pattern speed ($\Omega_b = 60\,\mathrm{km\,s^{-1}\,kpc^{-1}}$). Through this investigation, we determined that as the energy is decreased, we see that phase space regions having the same dynamical behaviour decreases in size. This is the opposite effect of a change in pattern speed. However, when the LDs method reveals more intricate and better defined NHIMs for our system, the sensitivity of a trajectory's dynamical evolution on the location of the IC is reduced.

We then looked more closely at the homoclinic and heteroclinic orbits by specifying which opening, between energetically forbidden regions, an orbit escapes from in the forward time (defining a trajectory's fate) and backward time (its origin). This classification of trajectories is called the OFM. The orbits where then classified by the origin-fate index. We called the opening near the L_1 orbit the upper opening, which is represented by the number 1, and the lower opening close to L_2 we labeled 2. The results were once again introduced for three different pattern speeds, and for $\Omega_b = 60\,\mathrm{km\,s^{-1}\,kpc^{-1}}$, we considered two different energy values. These investigations allowed us to, once again, determine the mixing of the different dynamical traits, which revealed the same outcomes as seen for the homoclinic and heteroclinic orbits. Additionally, we demonstrated that the different regions of the OFM were separated by the NHIMs, which were extracted from LD computations by the use of the gradient method demonstrated in Sect. 3.6.

In Sect. 4.5, we presented the configuration space structures created by orbits characterised by different dynamical traits. Initially, we showed that the morphology created by orbits which escaped more than twice and those which escaped either

once or twice have many similarities. The main difference was that there are fewer stars which escaped on more than two occasions over a period of $\tau = 289$. Next, we turned our attention to the homoclinic, heteroclinic and OFM orbits and showed the morphologies for not only the different orbit classifications but also for the three different pattern speeds. The results indicated that for each energy level, there is no significant difference between the structures associated with the homoclinc and heteroclinic orbits. This is a consequence of the 1-1 and 2-1 orbits creating similar patterns, something which is also observed for the 2-2 and 1-2 trajectories. We saw that the stars in the cases of larger pattern speeds created circular-like structures whereas lower rotational velocities led to more spiral-like morphologies. Finally, we discussed the impact of qualitative mixing on the different orbit types; we determine that the impact of mixing has an effect when considering the configuration space structures associated with different pattern speeds but not for different energy levels in the case of the same rotational velocity.

Chapter 5

Application of the Lagrangian descriptors method to systems described by fractional ordinary differential equations

In the foreword of [2] it is stated that fractional calculus experienced a paradigm shift in the 1970s as it found more applications in a wide array of the applied sciences. Some of these applications are mentioned for example in [95, 96, 97]. Although this branch of mathematics was becoming more popular, providing a physical interpretation of fractional integration and differentiation was not as simple as doing so for the integer order case. This lack of an apt elucidation was admitted in some of the first international conferences on fractional calculus, with one of the more recent being an international workshop on transformation methods and special functions in 1996 [98, 99] (see [100] for more information on a few of these conferences). Since those early conferences, there have been multiple attempts to offer both physical and geometrical explanations of fractional integrals and derivatives. Some studies have been conducted in an attempt to link fractional calculus and fractal geometry such as: finding a relationship between Cantor's fractal set and a fractional integral [101]; or the interpretation of fractional operators based on fractal geometry and the construction of a Cantor set [102]; and showing that for a fractional integral, its fractional derivative is not uniquely determined by the generalised cookie-cutter set's fractal dimension [103]. However, it has been shown that systems described by fractional order equations have not been built with ideas from fractal geometry [104, 105]. Furthermore, there have been interpretations of fractional calculus which do not refer to fractal geometry, such as: providing physical and geometrical interpretations of a fractional order GL differintegral through measuring the path and acceleration of a point in motion [106]; or by introducing a simple geometric explanation of multiple fractional integrals, which is then used to provide a physical understanding of the Riemann-Liouville fractional integration with regards to a dynamic time scale [100].

In this chapter, we offer a way of qualitatively presenting phase space structures associated with systems described by FDEs, and discuss how these structures change when the order α of the used fractional derivatives is modified. The key conclusion of our work is that the LDs method can be used to reveal phase space structures of FDE dynamical systems.

5.1 Dynamics of the fractional derivative version of the Duffing oscillator

The reason that we choose to implement the LDs method for systems of FDEs is because of its utility for dynamical systems of ODEs. We demonstrated in Sect. 3.6 that this numerical technique highlights phase space structures of dynamical systems in a manner which requires very little CPU time and reveals important information about the system's manifolds not captured in the PSS (as shown in Fig. 3.7). Furthermore, in Chapt. 4 we indicated that the NHIMs exposed by the computation of LDs allow for an investigation of the phase space transport of stars within a Hamiltonian system of galactic type. Therefore, we know that the LDs method is an extremely useful numerical tool that assigns each IC (in some grid in the phase space of a dynamical system) a positive scalar value depending on the system's evolution, both forward and backward in time. Due to the method's efficacy for systems comprised of ODEs, we decided to apply the LDs method to a rather simple dynamical system comprised of FDEs. While the LDs method has been used to reveal the NHIMs of dynamical systems described by ODEs, it is important to note that, in systems governed by FDEs, any curve with a curvature greater than zero (not a straight line) cannot be invariant [107] so that NHIMs are not found in dynamical systems described by FDEs. Additionally, FDEs are non-local and thus, are impacted by the selection of the integration time. Therefore, instead of revealing NHIMs (as previously seen in Sect. 3.6 and Chapt. 4), the LDs method for dynamical systems described by FDEs highlights phase space regions of the same dynamical behaviour, and structures which separate these regions for various integration intervals. Furthermore, one can use the LDs method to understand the change of a dynamical system's (whose evolution is governed by FDEs) underlying structures and phase space regions according to various integration times (τ) and to different fractional orders of the FDEs (α).

To demonstrate that the LDs method is a useful numerical technique for systems of FDEs, we examine the effects of multiple α and τ values on the phase space structures of the Duffing oscillator described by FDEs (3.50). The reason that we use this particular dynamical system is because the LDs method has already been used to reveal the phase portrait of the Duffing oscillator described by ODEs [3, 73] and stochastic differential equations [108]. The Duffing oscillator was introduced in 1918 [109] and is used to model various damped and driven oscillators. This dynamical system has found application in many physical and biological processes

(see e.g., [110, 111, 112]). The classical Duffing oscillator is given as

$$\ddot{x}(t) + \delta\dot{x}(t) + \beta x(t) + \psi x(t)^3 = \gamma\cos(\omega t), \tag{5.1}$$

where $\ddot{x}$ and $\dot{x}$ are time (t) derivatives of order two and one, respectively, of the spatial variable x, δ is a damping coefficient, $\beta x(t) + \psi x(t)^3$ is a nonlinear restoring force, ψ controls nonlinearity, β is a stiffness coefficient, $\gamma\cos(\omega t)$ is a driving force of amplitude γ, and frequency ω. We can rewrite (5.1) as a system of first order ODEs as follows

$$\begin{aligned} \dot{x}(t) &= y(t), \\ \dot{y}(t) &= \gamma\cos(\omega t) - \delta y(t) - \beta x(t) - \psi x(t)^3. \end{aligned} \tag{5.2}$$

Before conducting the examination of the Duffing oscillator described by FDEs, we apply the p-'norm' LDs method (3.57) to (5.2) with $\delta = \gamma = 0$, $\beta = -1$ and $\psi = 1$, which is given as

$$\begin{aligned} \dot{x}(t) &= y(t), \\ \dot{y}(t) &= x(t) - x(t)^3. \end{aligned} \tag{5.3}$$

This allows us to observe the differences between (5.3) and the results that will be presented for the Duffing oscillator whose evolution is governed by FDEs

$$\begin{aligned} D^\alpha x(t) &= y(t), \\ D^\alpha y(t) &= x(t) - x(t)^3. \end{aligned} \tag{5.4}$$

To showcase the phase space structures of the Duffing oscillator governed by ODEs, we implement the LDs method for $\tau = 5,\ 10$, and 20 using an equidistant grid of 1000×1000 ICs over the intervals $x \in [-1.5, 1.5]$ and $y \in [-1, 1]$. The obtained plots are presented in Fig. 5.1(a), (b), and (c), respectively. Additionally, the colour bars above each panel depict the magnitude of the LD values.

An examination of Fig. 5.1 reveals that there is practically no difference between the phase space structures of the Duffing oscillator governed by ODEs, seen in panels (a), (b), and (c). Hence, as we change the value of τ we do not see any changes in the NHIMs, indicating that an integration time of $\tau = 5$ is sufficient for convergence of all points on the NHIMs.

As we now have base cases for different τ values, we are able to use these integration times to examine the changes of the phase space structures for the dynamical system governed by FDEs (5.4). However, the integral seen in the p-'norm' LDs method (3.57) is applicable to dynamical systems described by ODEs. On the other hand, a system whose evolution is governed by FDEs uses fractional integration (as discussed in Sect. 3.5) and calculates the flow for discrete, equidistant time steps (for example $0 = \tau_0 < \tau_1 < \ldots < \tau_n < \tau_{n+1} = t$) over the interval $[0, t]$. Thus, we instead decided to use the discrete analogue of the LDs method [113, 114], which is seen as

$$M_p(x_0, n) = \sum_{j=-(n+1)}^{(n+1)-1} \sum_{i=1}^{N} \left| y_{j+1}^i - y_j^i \right|^p, \tag{5.5}$$

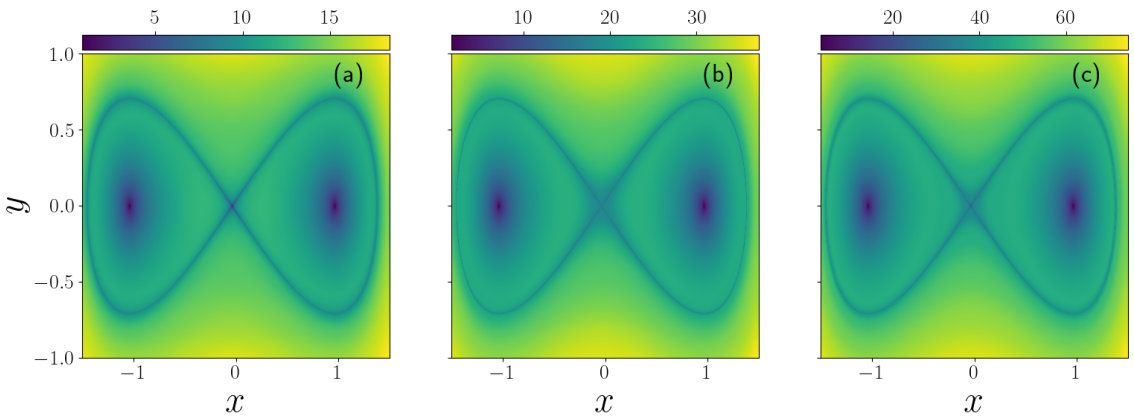

Figure 5.1: ICs of the Duffing oscillator (5.3) coloured according to the p-'norm' LD value (3.57). The colour bars above each panel indicate the LD values. The plots are created using an equidistant grid of 1000×1000 points over the intervals $x \in [-1.5, 1.5]$ and $y \in [-1, 1]$ and integration time of (a) $\tau = 5$, (b) $\tau = 10$, and (c) $\tau = 20$.

where y_j^i represents the i^{th} component of the vector y at time τ_j. We were not able to create similar dense plots to those seen in Fig. 5.1, for the Duffing oscillator described by FDEs (3.50). However, we now use an equidistant grid of 100×100 ICs in Fig. 5.2 because of CPU time restrictions experienced due to the integration of the system governed by FDEs. These limitations occur because the flow at each time step is calculated using the memory of the evolution at all previous time steps. To create the results seen in Fig. 5.2, we used both the time reversible integration scheme (3.55) for the panels (a), (e), (i), (m), (q), (u), and (y) depicted in the first column of Fig. 5.2 and the irreversible time method [the explicit GL scheme (3.31)], for columns two, three, and four of Fig. 5.2. For the time reversible integration scheme, we only used $\tau = 5$, as we experienced large CPU times for the backwards integration. In particular, the convergence of the root finding method required ample CPU time (as mentioned in Sect. 3.5.4). Additionally, in cases where the root finding technique did not converge for a particular orbit, we colour the associated IC in white, as seen in Figs. 5.2(q), (u), and (y). The second column of Fig. 5.2 [panels (b), (f), (j), (n), (r), (v), (z), (cc), (ff), and (ii)] depicts the results for $\tau = 5$, the third column [panels (c), (g), (k), (o), (s), (w), (aa), (dd), (gg), and (jj)] presents the results for $\tau = 10$ and the final column of plots [panels (d), (h), (l), (p), (t), (x), (bb), (ee), (hh), (kk)] show the LD values for $\tau = 20$. Furthermore, each row of panels of Fig. 5.2 relates to the fractional Duffing oscillator for a different α value. Figures 5.2(a)–(d) correspond to the system with $\alpha = 0.9999$, Figs. 5.2(e)–(h) present coloured phase space portraits for the system with $\alpha = 0.99$ and each row that follows refers to the fractional derivative version of the Duffing oscillator for a decreasing order of α ($\alpha = 0.98$, 0.97, 0.96, 0.95, 0.9, 0.85, 0.8, and 0.75). However, due to the root finding method not converging for systems of smaller values of α, we only display results for the time reversible approach for $\alpha = 0.9999$ to $\alpha = 0.9$.

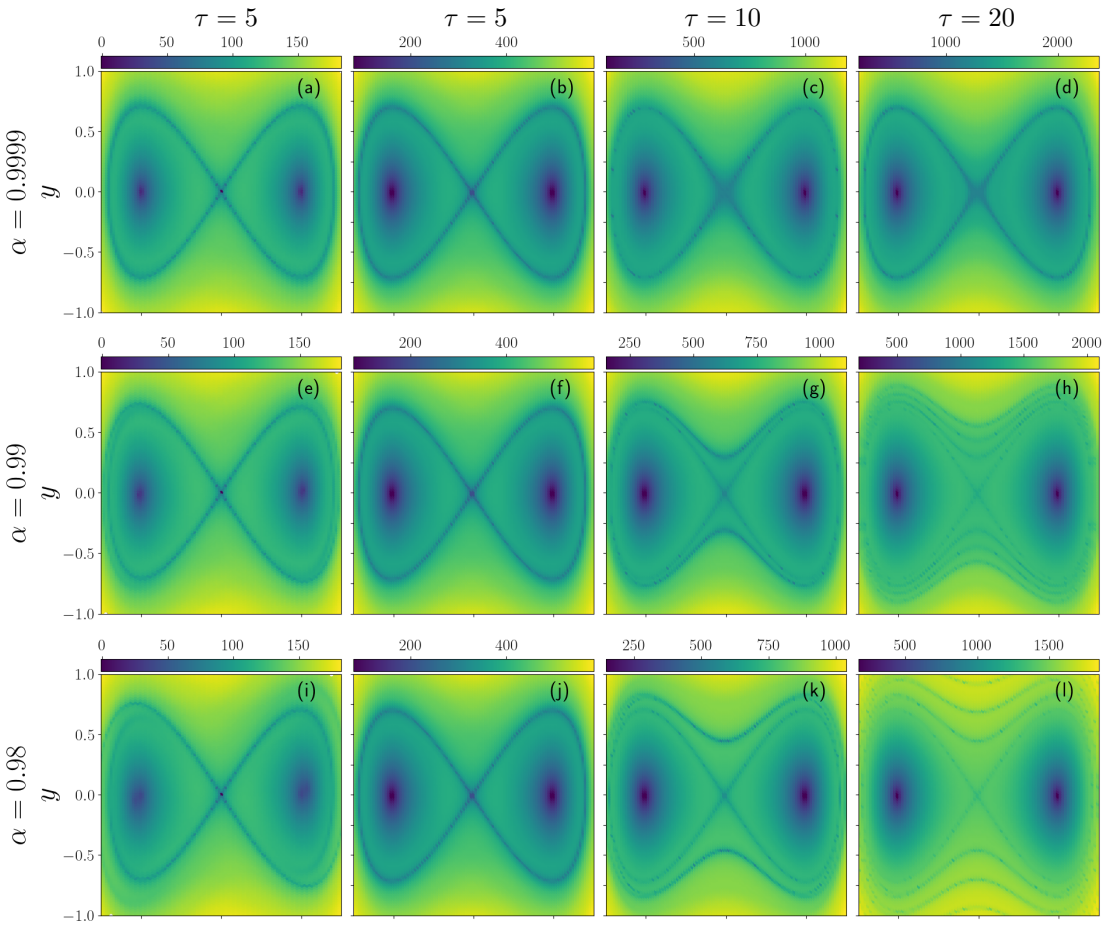

Figure 5.2: Geometric structures of the fractional duffing oscillator dynamical system (3.50) created by colouring ICs according to the p-'norm' LD value (3.57) shown in the colour bar above each plot. Panels are created using 100×100 equidistant ICs over the same intervals as seen in Fig. 5.1. The first column of plots integrates orbits using the time reversible integration scheme (3.55) and the explicit GL integrator that is not time reversible (3.31) was used to create the plots in column two, three and four. Additionally, the panels in column one and two used the LDs method with $\tau = 5$, the third column implemented $\tau = 10$, and the fourth column indicates results for $\tau = 20$. Furthermore, the results in each row relate to the system with decreasing values of α, where panels (a) to (d) reveal the geometric structures for $\alpha = 0.9999$, (e) to (h) pertain to the system with $\alpha = 0.99$ and each row that follows relates respectively to the values $\alpha = 0.98,\ 0.97,\ 0.96,\ 0.95,\ 0.9,\ 0.85,\ 0.8$, and 0.75.

In Figs. 5.2(a)–(d) we see that no matter the τ value, the system for $\alpha = 0.9999$ produces results that are approximately equivalent to those seen for the Duffing oscillator governed by ODEs, in Figs. 5.1(a)–(c). Thus, when $\alpha \approx 1$ the geometric structures of (5.4), appear to be somewhat invariant with time. That is, we see approximately the same dark areas at the fixed points [$(x, y) = (-1, 0)$ and $(x, y) =$

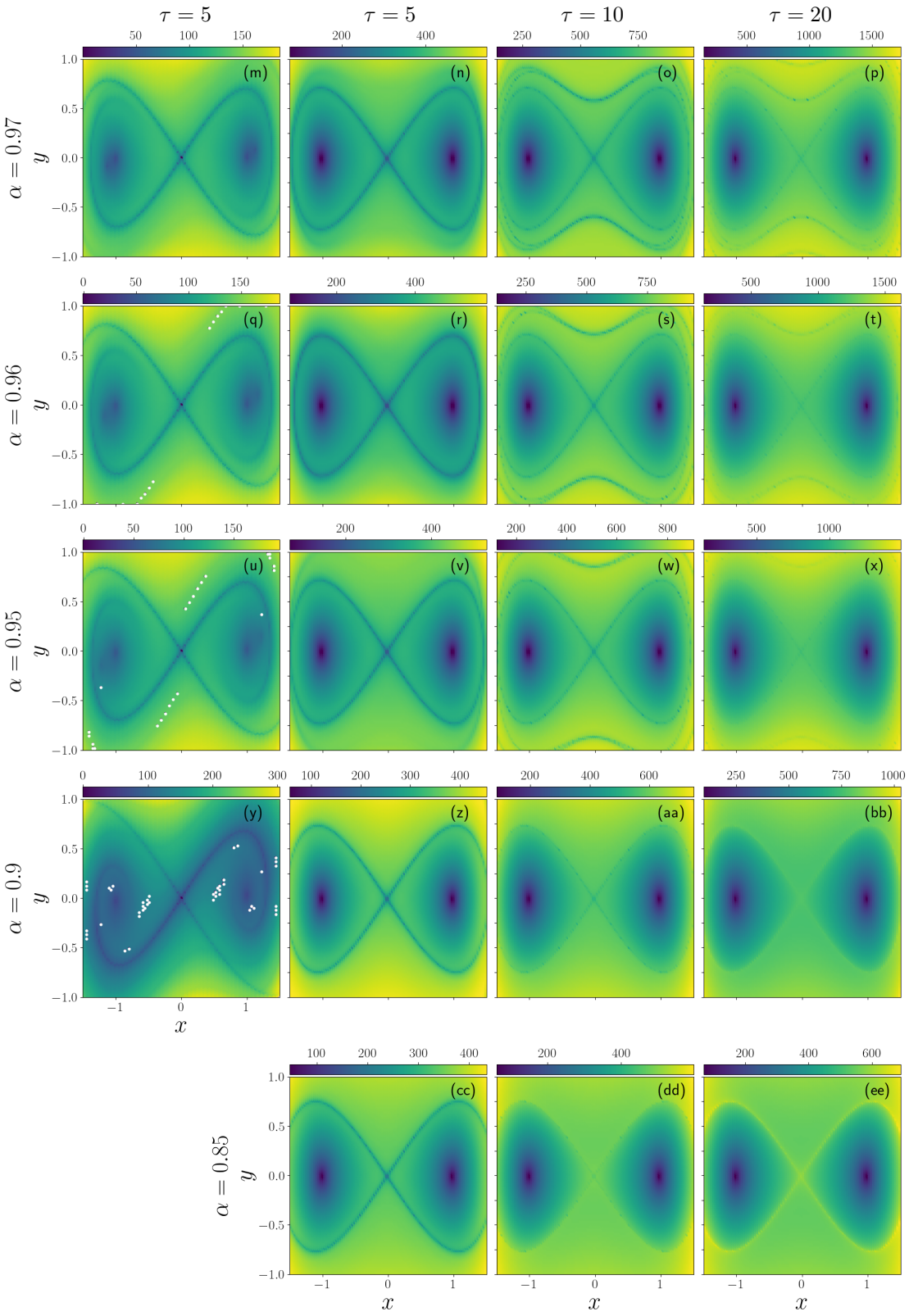

Figure 5.2: Continued.

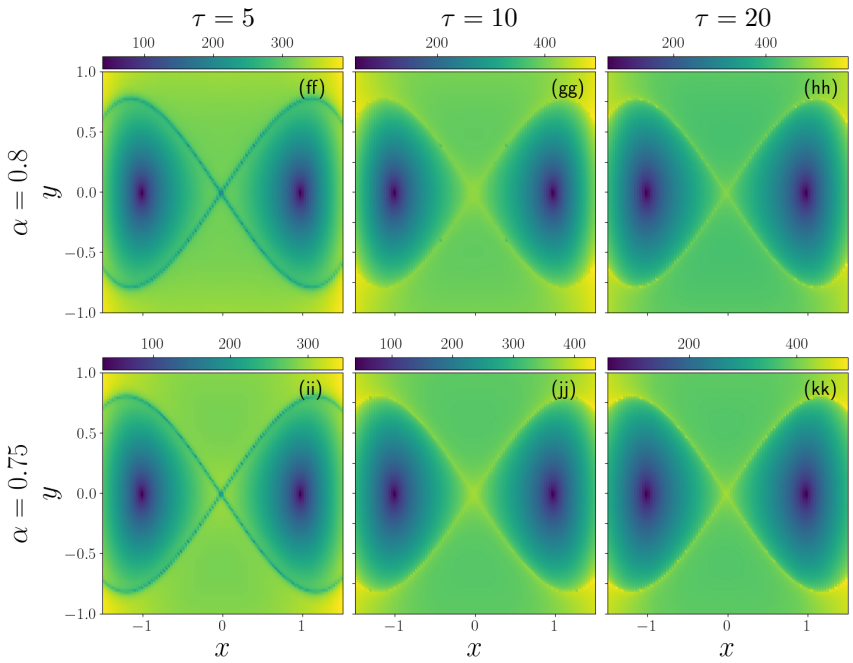

Figure 5.2: Continued.

$(1, 0)$], as well as the same dark curves shaped like the infinity symbol (which we shall henceforth call "infinity shaped") centred at $(x, y) = (0, 0)$.

As we decrease the α value slightly to 0.99 and compare the plots for the integrator which is not time reversible [Figs. 5.2(f)–(h)], we see that the structures begin to display dependency on τ. In Fig. 5.2(f), we see the infinity shaped dark curve is approximately the same as that revealed using the LDs method with $\tau = 5$ and for the system with $\alpha = 0.9999$ [Fig. 5.2(b)]. In contrast, Fig. 5.2(g) not only has the infinity shaped dark curves but also an additional dark coloured curve outside of the infinity shaped structure, while in Fig. 5.2(h) we see two more such curves outside of those seen in Fig. 5.2(g). However, through the observation of Figs. 5.2(f)–(h), we see that all panels display reflective symmetry. This symmetry is not seen when we use the time reversible integrator for the LDs method with $\tau = 5$; instead Fig. 5.2(e) displays point symmetry. In particular, the infinity shaped phase space feature seen in Fig. 5.2(e) is slightly detached near the bounds of the x-axis, and this is the reason that we see a break in the reflective symmetry. This disconnected shape is slightly different compared to the continuous infinity formation seen for the dynamical system with $\alpha = 0.9999$ in Fig. 5.2(a).

By further reducing the value of α to 0.98 and examining the effect of integration time in Figs. 5.2(j)–(l), we see an increase in the amount of dark coloured curves, which is a similar trend to that seen in the Duffing oscillator with $\alpha = 0.99$ in Figs. 5.2(f)–(h). Although, for $\tau = 10$ and $\tau = 20$ [Figs. 5.2(k) and (l)] the distance between dark curves has increased compared to the system with $\alpha = 0.99$ and the same integration times [Figs. 5.2(g) and (h)]. Through an observation of the geometrical patterns of the dynamical system described by FDEs (highlighted by

the LDs method using the time reversible integration scheme with $\tau = 5$), we see that the discontinuity of the infinity shaped, dark coloured structures [presented in Fig. 5.2, for the system with $\alpha = 0.99$] becomes more apparent for $\alpha = 0.98$.

Next, we observe Figs. 5.2(m)–(p), which present ICs of the Duffing oscillator, governed by FDEs with $\alpha = 0.97$, that are coloured according to their LD values. In these plots we see approximately the same geometric formations as presented for the dynamical system with $\alpha = 0.99$ [Figs. 5.2(e)–(h)] and $\alpha = 0.98$ [Figs. 5.2(i)–(l)]. The contrasts between these geometric structures are as follows: as we reduce the value of α and examine the phase portraits associated with the time irreversible integrator for $\tau = 10$ and $\tau = 20$ [Figs. 5.2(o) and (p) respectively], we see that the additional dark curves outside of the infinity shape, separate and leave more space between them; we also see an increase in the disconnection of the infinity shaped pattern related to the LDs method which uses the time reversible numerical scheme [Fig. 5.2(m)].

Examining the next row of plots [Fig. 5.2(q)–(t)] which show the phase space structures of the Duffing oscillator described by FDEs of order $\alpha = 0.96$, reveals the continuation of the trends discussed before (increased discontinuity and greater space between the darker geometric patterns). Furthermore, we see white points in Fig. 5.2(q) indicating that the root finding method for the time reversible integration scheme did not converge for the orbits associated with these ICs. It is also seen that the infinity shaped curve and the structures surrounding this curve, obtained by using the LDs method with $\tau = 20$ [Fig. 5.2(t)], are not as dark as the features seen in the dynamical systems with larger α values [Figs. 5.2(h), (l), and (p)].

Figures 5.2(u)–(x) show the phase space structures of (5.4) with $\alpha = 0.95$. The dark curves revealed using the LDs method with the time reversible integrator and $\tau = 5$ [Fig. 5.2(u)], are completely separate except for their intersection at the origin. We also observe an increase in the number of white points in this plot, compared to the system with $\alpha = 0.96$ [Fig. 5.2(q)]. Additionally, the interior of the two dark curves appear to be tending toward the dark regions at $(x, y) = (-1, 0)$ and $(x, y) = (1, 0)$, as we decrease the order of the fractional derivatives. All properties of this phase portrait appear to become more pronounced as we decrease the α value to 0.9 [Fig. 5.2(y)], including an increase in the number of white points. As we have seen an increase in orbits which did not converge using the root finding method as we decrease the fractional order α, we notice that the method is reaching the limits of its computational efficiency and applicability. Thus, we do not show any additional plots relating to the time reversible integrator.

Next, we observe the geometric structures displayed through the implementation of the LDs method and the time irreversible integration scheme [Figs. 5.2(v)–(x)]. It is seen that the space between the dark curves has increased when the LDs method used $\tau = 10$ [Fig. 5.2(w)], compared to the system with a larger fractional order [Fig. 5.2(s)]. Moreover, the dark geometric structures that are seen in plots corresponding to the LDs method with $\tau = 20$ and systems with higher ordered FDEs [Figs. 5.2(t), (p), (l), and (h)], are barely seen in Fig. 5.2(x).

The geometric features in Figs. 5.2(z), (aa), and (bb) (exposed by the LDs method with the irreversible time integrator for the Duffing oscillator described by FDEs of order $\alpha = 0.9$) are all infinity shaped, which is similar to the patterns revealed for the system with $\alpha = 0.9999$ [Figs. 5.2(b), (c), and (d)]. However, only the plots for $\tau = 5$ [Fig. 5.2(b) and (z)] are similar in colour. The curves seen in Figs. 5.2(aa) and (bb) are lighter than those presented in panels (c) and (d), respectively. Additionally, Fig. 5.2(bb), corresponding to the implementation of $\tau = 20$ has curves which are somewhere between green and yellow, while those displayed in Fig. 5.2(aa) are somewhat blue. Therefore, the infinity shaped structures indicate that the orbits associated with ICs on this formation, diverge. As the systems with lower α values are observed [Figs. 5.2(cc)–(kk)], we see that the infinity shaped curves become more yellow (and hence correspond to ICs with large LD values) and expand in the x direction as we can no longer see the closing of the curves on the bounds of the x axis.

5.2 Summary

In this chapter, we have seen that the LDs method can be applied to dynamical systems of FDEs. We have shown how this numerical method allows one to reveal the underlying geometric features of a dynamical system whose evolution is governed by FDEs. Not only did the LDs method reveal various patterns, it also allowed us to determine how different fractional orders of the FDEs influenced these patterns. Therefore, the method provides a qualitative geometric interpretation of such systems, while also offering a potential method which could be used to examine regions of phase space associated with various dynamical traits. In particular, we presented the structures relating to the Duffing oscillator described by FDEs with various values of α, calculated using the p-'norm' LDs method for different integration times. Thus, we offered a qualitative method to visualise the dynamics associated with such systems and potentially offer a way that can be used to study the phase space transport experienced in these systems.

Chapter 6

Summary and conclusions

In this thesis, we have numerically revealed phase space structures of dynamical systems whose evolution is governed by ODEs and FDEs by implementing the LDs method. We have shown how this computationally inexpensive and simple to implement numerical technique, not only discerns phase space regions of different dynamical features in more depth than the useful PSS but that it can also be implemented for a wide variety of dynamical systems.

Our work began by laying a foundation from which we could later conduct our main exploration. In Chapt. 2 we presented the fundamental notion of a dynamical system and stated that its flow describes the time evolution of orbits associated with different ICs. In particular, we illustrated the basic concepts of Hamiltonian mechanics and the so-called Hamiltonian eom (2.25), which are described by ODEs. We also showcased different FDEs, such as the Riemann-Liouville derivative (2.28), the Caputo derivative (2.29), and the GL derivative (2.35). We then explained how most natural and artificial processes are modelled using nonlinear eom and therefore, their flow cannot be found analytically. Thus, in Chapt. 3 we provided an exposition of various numerical integration techniques. For systems described by ODEs, we discussed two numerical integrators [the RK6 (3.6) and ABA864 (3.18) methods] and demonstrated their benefits, limitations, and differences. Furthermore, for systems of FDEs, we also presented two integration schemes: a time reversible method (3.55) and a numerical technique that is irreversible with time (3.31). For the second method, we also proposed a way to improve the required CPU time while maintaining a desired level of accuracy over an integration time interval. Based on the description of various dynamical systems and of numerical techniques for numerically computing the evolution of such systems, we then presented the LDs method in Sect. 3.6. We demonstrated this numerical method and examined its advantages over the commonly used PSS, for exposing phase space regions with similar dynamical traits in Fig. 3.7. We also showed how the LDs method can be used to extract the NHIMs from a system whose evolution is governed by ODEs. Additionally, we demonstrated how the LDs method can be split into its forward and backward components to explicitly reveal the stable and unstable manifolds, respectively.

In Chapt. 4 we described a Hamiltonian system of galactic type in order to examine the influence of NHIMs (revealed by the LDs method) on the escape of trajectories (stars) from the galaxy as well as the possible supported orbital morphologies. We first presented and discussed the influence of stable NHIMs on trajectories which are evolved forward in time. It was shown that the stable manifolds influence the time taken for an orbit to escape (Fig. 4.6), the time that an orbit spends outside of the interior region of the model's configuration space [Fig. 4.8(a)], and the number of times that an orbit escapes the central region [Fig. 4.8(b)]. It was, additionally, seen that the unstable NHIMs influence orbits that are integrated backward in time, and that the phase space regions enclosed by these manifolds are symmetric to those created by the stable manifolds. We then examined phase space regions of ICs which relate to trajectories that are influenced by both the stable and unstable NHIMs, such as: regions of homoclinic and heteroclinic orbits (trajectories which both escape and enter from the same opening between the energetically forbidden regions in configuration space or enter from one opening and escape from another, respectively) and regions characterised by the OFM (explicitly stating which opening between the energetically forbidden regions in configuration space an orbit escaped and entered from). We saw how these phase space regions changed as we altered the model's pattern speed while maintaining an equal spacing between the energetically forbidden areas, and as the pattern speed was kept constant while the energy of the system was changed. It was observed that these alterations impacted the size of regions with the same dynamical traits, the amount of NHIMs revealed by the LDs method, and how well defined these manifolds were. Finally, we presented the morphologies in configuration space that are created by orbits which display different dynamical behaviours. In Fig. 4.16, we showed the features created by orbits which were classified in different categories according to the number of times they escaped the central region in configuration space, while Fig. 4.17 displayed the structures created by orbits classified as homoclinic, heteroclinic, as well as belonging to different categories according to the OFM for different pattern speeds and energies.

In a novel attempt to display phase space structures of a dynamical system governed by FDEs, we applied the LDs method to the Duffing oscillator whose evolution is described by FDEs in Chapt. 5. We explored how features seen in the phase portrait change for the dynamical system with varying fractional orders, over different integration time intervals, and for two numerical integration schemes. We determined that the LDs method is a useful technique to qualitatively interpret geometrical structures found within the phase portrait of systems described by FDEs. Additionally, this numerical tool is able to display regions of orbits with similar dynamical traits. Therefore, we conclude that the LDs method could be useful for researchers who are interested in examining the phase space transport of systems whose evolution is governed by FDEs.

Bibliography

[1] S.H. Strogatz. *Nonlinear Dynamics and Chaos: With Applications to Physics, Biology, Chemistry, and Engineering*. CRC press, 2018.

[2] C. Li and F. Zeng. *Numerical Methods for Fractional Calculus*. CRC Press, 2015.

[3] M. Agaoglou, B.A. Sanjuan, V.J. García-Garrido, F.G. Montoya, M. Katsanikas, V. Krajňák, S. Naik, and S. Wiggins. *Lagrangian Descriptors: Discovery and Quantification of Phase Space Structure and Transport*. Zenodo, 2020.

[4] M. Katsanikas and P.A. Patsis. The structure of invariant tori in a 3D galactic potential. *International Journal of Bifurcation and Chaos*, **21**:467, 2011.

[5] B. Michael and S. Garrett. *Introduction to Dynamical Systems*. Cambridge University Press, 2002.

[6] H.E. Nusse and J.A. Yorke. *Dynamics: Numerical Explorations: Accompanying Computer Program Dynamics*. Springer, 2012.

[7] W.M. Haddad, V. Chellaboina, and S.G. Nersesov. *Thermodynamics: A Dynamical Systems Approach*. Princeton University Press, 2009.

[8] J.J. Thomson. *Applications of Dynamics to Physics and Chemistry*. Macmillan, 1888.

[9] M.J. Valtonen and H. Karttunen. *The Three-Body Problem*. Cambridge University Press, 2006.

[10] G.L. Cassiday and G.R. Fowles. *Analytical Mechanics*. Saunders College, 1993.

[11] V.V. Kozlov. *Dynamical Systems X: General Theory of Vortices*. Springer Science & Business Media, 2013.

[12] K.B. Oldham and J. Spanier. *The Fractional Calculus: Theory and Applications of Differentiation and Integration to Arbitrary Order*. Elsevier, 1974.

[13] N. Engheta. On fractional calculus and fractional multipoles in electromagnetism. *IEEE Transactions on Antennas and Propagation*, **44**:554, 1996.

[14] X. Yang, F. Gao, and Y. Ju. *General Fractional Derivatives with Applications in Viscoelasticity*. Academic Press, 2020.

[15] V.V. Kulish and J.L. Lage. Application of fractional calculus to fluid mechanics. *Journal of Fluids Engineering*, **124**:803, 2002.

[16] K.B. Oldham. Fractional differential equations in electrochemistry. *Advances in Engineering software*, **41**:9, 2010.

[17] H. Jafari, R.M. Ganji, N.S. Nkomo, and Y.P. Lv. A numerical study of fractional order population dynamics model. *Results in Physics*, **27**:104456, 2021.

[18] P. Veeresha, D.G. Prakasha, and S. Kumar. A fractional model for propagation of classical optical solitons by using nonsingular derivative. *Mathematical Methods in the Applied Sciences*, 2020.

[19] I. Podlubny. *Fractional Differential Equations: An Introduction to Fractional Derivatives, Fractional Differential Equations, to Methods of Their Solution and Some of Their Applications*. Elsevier, 1998.

[20] M. Caputo. Linear models of dissipation whose Q is almost frequency independent—II. *Geophysical Journal International*, **13**:529, 1967.

[21] R. Scherer, S.L. Kalla, Y. Tang, and J. Huang. The Grünwald–Letnikov method for fractional differential equations. *Computers & Mathematics with Applications*, **62**:902, 2011.

[22] P.J. Davis and P. Rabinowitz. *Methods of Numerical Integration*. Courier Corporation, 2007.

[23] S.O. Fatunla. *Numerical Methods for Initial Value Problems in Ordinary Differential Equations*. Academic Press, 2014.

[24] E. Süli and D.F. Mayers. *An Introduction to Numerical Analysis*. Cambridge University Press, 2003.

[25] A. Iserles. *A First Course in the Numerical Analysis of Differential Equations*. Cambridge University Press, 2009.

[26] W.H. Press, S.A. Teukolsky, W.T. Vetterling, and B.P. Flannery. *Numerical Recipes 3rd Edition: The Art of Scientific Computing*. Cambridge University Press, 2007.

[27] H.A. Luther. An explicit sixth-order Runge-Kutta formula. *Mathematics of Computation*, **22**:434, 1968.

[28] P.J. Channell and C. Scovel. Symplectic integration of Hamiltonian systems. *Nonlinearity*, **3**:231, 1990.

[29] R. De Vogelaere. Methods of integration which preserve the contact transformation property of the Hamilton equations. *Technical report 4, Department of Mathematics, University of Notre Dame*, 1956.

[30] B. Senyange and Ch. Skokos. Computational efficiency of symplectic integration schemes: application to multidimensional disordered Klein–Gordon lattices. *The European Physical Journal Special Topics*, **227**:625, 2018.

[31] M. Thudiyangal C. Danieli, B.M. Manda and Ch. Skokos. Computational efficiency of numerical integration methods for the tangent dynamics of many-body Hamiltonian systems in one and two spatial dimensions. *Mathematics in Engineering*, **1**:447, 2019.

[32] S. Komineas Ch. Skokos, D. Krimer and S. Flach. Delocalization of wave packets in disordered nonlinear chains. *Physical Review E*, **79**:056211, 2009.

[33] H. Yoshida. Construction of higher order symplectic integrators. *Physics letters A*, **150**:262, 1990.

[34] A. Farres J. Laskar J. Makazaga S. Blanes, F. Casas and A. Murua. New families of symplectic splitting methods for numerical integration in dynamical astronomy. *Applied Numerical Mathematics*, **68**:58, 2013.

[35] Ch. Skokos and T. Manos. The smaller (SALI) and the generalized (GALI) alignment indices: efficient methods of chaos detection. *Lecture Notes in Physics, Springer*, **915**:129, 2016.

[36] M. Hillebrand, S. Zimper, A. Ngapasare, M. Katsanikas, S. Wiggins, and Ch. Skokos. Quantifying chaos using Lagrangian descriptors. *Chaos: An Interdisciplinary Journal of Nonlinear Science*, **32**:123122, 2022.

[37] A. Daza, A. Wagemakers, B. Georgeot, D. Guéry-Odelin, and M.A.F. Sanjuán. Basin entropy: a new tool to analyze uncertainty in dynamical systems. *Scientific reports*, **6**:31416, 2016.

[38] M. Hénon and C. Heiles. The applicability of the third integral of motion: some numerical experiments. *The astronomical journal*, **69**:73, 1964.

[39] J.H. Jeans. On the theory of star-streaming and the structure of the universe. *Monthly Notices of the Royal Astronomical Society*, **76**:70, 1915.

[40] J.H. Jeans. The origin of binary systems. *Monthly Notices of the Royal Astronomical Society*, **79**:408, 1919.

[41] B. Lindblad. *Die Milchstraße*. Springer, 1933.

[42] B. Lindblad. *Astrophysik IV: Sternsysteme/Astrophysics IV: Stellar Systems*. Springer, 1959.

[43] G. Contopoulos. On the existence of a third integral of motion. *The Astronomical Journal*, **68**:1, 1963.

[44] A. Ollongren. Three-dimensional galactic stellar orbits. *Bulletin of the Astronomical Institutes of the Netherlands*, **16**:241, 1962.

[45] Ch. Skokos. The Lyapunov characteristic exponents and their computation. In dynamics of small solar system bodies and exoplanets. *Lecture Notes in Physics*.

[46] W. Dittrich and M. Reuter. *Classical and Quantum Dynamics. From Classical Paths to Path Integrals*. Springer-Verlag Berlin Heidelberg, 2001.

[47] J. Stewart. *Calculus: Early Transcendentals*. Cengage Learning, 2012.

[48] M. Hénon. On the numerical computation of Poincaré maps. *Physica D: Nonlinear Phenomena*, **5**:412, 1982.

[49] I. Petrás. *Fractional Derivatives, Fractional Integrals, and Fractional Differential Equations in Matlab*. IntechOpen, 2011.

[50] G. Mittag-Leffler. Sur la nouvelle fonction $e\alpha(x)$. *CR Acad. Sci. Paris*, **137**:554, 1903.

[51] K. Górska, A. Lattanzi, and G. Dattoli. Mittag-Leffler function and fractional differential equations. *Fractional Calculus and Applied Analysis*, **21**:220, 2018.

[52] J. Duan. A generalization of the Mittag-Leffler function and solution of system of fractional differential equations. *Advances in Difference Equations*, **2018**:239, 2018.

[53] A. Ghasempour, Y. Ordokhani, and S. Sabermahani. Fractional-order Mittag-Leffler functions for solving multi-dimensional fractional pantograph delay differential equations. *Iranian Journal of Science*, **47**:885, 2023.

[54] G.J.O. Jameson. A simple proof of Stirling's formula for the gamma function. *The Mathematical Gazette*, **99**:68, 2015.

[55] S. Qureshi, K.A. Abro, and J.F. Gómez-Aguilar. On the numerical study of fractional and non-fractional model of nonlinear Duffing oscillator: a comparison of integer and non-integer order approaches. *International Journal of Modelling and Simulation*, **43**:362, 2023.

[56] Y.Y. Gambo, R. Ameen, F. Jarad, and T. Abdeljawad. Existence and uniqueness of solutions to fractional differential equations in the frame of generalized Caputo fractional derivatives. *Advances in Difference Equations*, **2018**:1, 2018.

[57] N. Hayek, J. Trujillo, M. Rivero, B. Bonilla, and J.C. Moreno. An extension of Picard-Lindelöff theorem to fractional differential equations. *Applicable Analysis*, **70**:347, 1998.

[58] N. Fenichel and J.K. Moser. Persistence and smoothness of invariant manifolds for flows. *Indiana University Mathematics Journal*, **21**:193, 1971.

[59] N. Fenichel. Asymptotic stability with rate conditions. *Indiana University Mathematics Journal*, **23**:1109, 1974.

[60] N. Fenichel. Asymptotic stability with rate conditions, II. *Indiana University Mathematics Journal*, **26**:81, 1977.

[61] J. Eldering. *Normally Hyperbolic Invariant Manifolds: The Noncompact Case*. Springer, 2013.

[62] M.W. Hirsch, C.C. Pugh, and M. Shub. Invariant manifolds. *Bulletin of the American Mathematical Society*, **76**:1015, 1970.

[63] R. Mañé. Persistent manifolds are normally hyperbolic. *Transactions of the American Mathematical Society*, **246**:261, 1978.

[64] S. Wiggins. *Normally Hyperbolic Invariant Manifolds in Dynamical Systems*. Springer Science & Business Media, 1994.

[65] J.A. Madrid and A.M. Mancho. Distinguished trajectories in time dependent vector fields. *Chaos: An Interdisciplinary Journal of Nonlinear Science*, **19**:013111, 2009.

[66] C. Mendoza and A.M. Mancho. Hidden geometry of ocean flows. *Physical review letters*, **105**:038501, 2010.

[67] S. Raffa, G. Merisio, and F. Topputo. Finding regions of bounded motion in binary asteroid environment using Lagrangian descriptors. *Communications in Nonlinear Science and Numerical Simulation*, **121**:107198, 2023.

[68] G.T. Craven, A. Junginger, and R. Hernandez. Lagrangian descriptors of driven chemical reaction manifolds. *Physical Review E*, **96**:022222, 2017.

[69] M. Katsanikas, V.J. García-Garrido, and S. Wiggins. Detection of dynamical matching in a Caldera Hamiltonian system using Lagrangian descriptors. *International Journal of Bifurcation and Chaos*, **30**:2030026, 2020.

[70] F. Revuelta, R.M. Benito, and F. Borondo. Unveiling the chaotic structure in phase space of molecular systems using Lagrangian descriptors. *Physical Review E*, **99**:032221, 2019.

[71] S. Zimper, A. Ngapasare, M. Hillebrand, M. Katsanikas, S.R. Wiggins, and Ch. Skokos. Performance of chaos diagnostics based on Lagrangian descriptors. Application to the 4D standard map. *Physica D: Nonlinear Phenomena*, **453**:133833, 2023.

[72] K.T. Alligood, T.D. Sauer, and J.A. Yorke. *Chaos: An Introduction to Dynamical Systems*. Springer-Verlag Berlin Heidelberg, 1996.

[73] A.M. Mancho, S. Wiggins, J. Curbelo, and C. Mendoza. Lagrangian descriptors: a method for revealing phase space structures of general time dependent dynamical systems. *Communications in Nonlinear Science and Numerical Simulation*, **18**:3530, 2013.

[74] C. Amitrano and R.S. Berry. Probability distributions of local Lyapunov exponents for Hamiltonian systems. *Physical Review E*, **47**:3158, 1993.

[75] E.E. Zotos. Classifying orbits in the classical Hénon–Heiles Hamiltonian system. *Nonlinear Dynamics*, **79**:1665, 2015.

[76] A.S. Demian and S. Wiggins. Detection of periodic orbits in Hamiltonian systems using Lagrangian descriptors. *International Journal of Bifurcation and Chaos*, **27**:1750225, 2017.

[77] S. Naik, V.J. García-Garrido, and S. Wiggins. Finding NHIM: identifying high dimensional phase space structures in reaction dynamics using Lagrangian descriptors. *Communications in Nonlinear Science and Numerical Simulation*, **79**:104907, 2019.

[78] M. Katsanikas, V.J. García-Garrido, M. Agaoglou, and S. Wiggins. Phase space analysis of the dynamics on a potential energy surface with an entrance channel and two potential wells. *Physical Review E*, **102**:012215, 2020.

[79] M. Miyamoto and R. Nagai. Three-dimensional models for the distribution of mass in galaxies. *Astronomical Society of Japan, Publications*, **27**:533, 1975.

[80] M. Katsanikas, P.A. Patsis, and G. Contopoulos. Instabilities and stickiness in a 3D rotating galactic potential. *International Journal of Bifurcation and Chaos*, **23**:1330005, 2013.

[81] M. Katsanikas, P.A. Patsis, and G. Contopoulos. The structure and evolution of confined tori near a Hamiltonian Hopf bifurcation. *International Journal of Bifurcation and Chaos*, **21**:2321, 2011.

[82] J. Binney and S. Tremaine. *Galactic Dynamics*. Princeton University Press, 2008.

[83] J.M.A. Danby. The formation of arms in barred spirals. *The Astronomical Journal*, **70**:501, 1965.

[84] S. Van den Bergh. *Galaxy Morphology and Classification*. Cambridge University Press, 1998.

[85] M. Romero-Gómez, E. Athanassoula, J.J. Masdemont, and C. García-Gómez. The formation of spiral arms and rings in barred galaxies. *Astronomy & Astrophysics*, **472**:63, 2007.

[86] M. Romero-Gómez, J.J. Masdemont, E. Athanassoula, and C. García-Gómez. The origin of rR_1 ring structures in barred galaxies. *Astronomy & Astrophysics*, **453**:39, 2006.

[87] E. Athanassoula, M. Romero-Gómez, and J.J. Masdemont. Rings and spirals in barred galaxies–I. Building blocks. *Monthly Notices of the Royal Astronomical Society*, **394**:67, 2009.

[88] E. Athanassoula, M. Romero-Gómez, A. Bosma, and J.J. Masdemont. Rings and spirals in barred galaxies–II. Ring and spiral morphology. *Monthly Notices of the Royal Astronomical Society*, **400**:1706, 2009.

[89] G. Contopoulos. Asymptotic curves and escapes in Hamiltonian systems. *Astronomy and Astrophysics*, **231**:41, 1990.

[90] W.S. Koon, M.W. Lo, J.E. Marsden, and S.D. Ross. Low energy transfer to the Moon. *Celestial Mechanics and Dynamical Astronomy*, **81**:63, 2001.

[91] W.S. Koon, M.W. Lo, J.E. Marsden, and S.D. Ross. Resonance and capture of Jupiter comets. *Celestial Mechanics and Dynamical Astronomy*, **81**:27, 2001.

[92] D. Beigie, A. Leonard, and S. Wiggins. Invariant manifold templates for chaotic advection. *Chaos, Solitons & Fractals*, **4**:749, 1994.

[93] M. Hillebrand, M. Katsanikas, S. Wiggins, and Ch. Skokos. Navigating phase space transport with the origin-fate map. *Physical Review E*, **108**:024211, 2023.

[94] L.S. Sparke and J.S. Gallagher III. *Galaxies in the Universe: An Introduction*. Cambridge University Press, 2007.

[95] A.A. Kilbas, H.M. Srivastava, and J.J. Trujillo. *Theory and Applications of Fractional Differential Equations*. Elsevier, 2006.

[96] V.E. Tarasov. *Fractional Dynamics: Applications of Fractional Calculus to Dynamics of Particles, Fields and Media*. Springer Science & Business Media, 2011.

[97] R. Herrmann. *Fractional Calculus: An Introduction for Physicists*. World Scientific, 2011.

[98] R. Gorenflo. Afterthoughts on interpretation of fractional derivatives and integrals. *Transform methods and special functions, Varna*, **96**:589, 1998.

[99] F. Mainardi. Considerations on fractional calculus: interpretations and applications. *Transform methods and special functions, Varna*, **96**:594, 1998.

[100] I. Podlubny. Geometric and physical interpretation of fractional integration and fractional differentiation. *Fractional Calculus and Applied Analysis*, **5**:367, 2008.

[101] R.R. Nigmatullin. Fractional integral and its physical interpretation. *Theoretical and mathematical physics*, **90**:242, 1992.

[102] M. Moshrefi-Torbati and J.K. Hammond. Physical and geometrical interpretation of fractional operators. *Journal of the Franklin Institute*, **335**:1077, 1998.

[103] Z. Yu, F. Ren, and J. Zhou. Fractional integral associated to generalized cookie-cutter set and its physical interpretation. *Journal of Physics A: Mathematical and General*, **30**:5569, 1997.

[104] R.S. Rutman. On physical interpretations of fractional integration and differentiation. *Theoretical and Mathematical Physics*, **105**:1509, 1995.

[105] R.S. Rutman. On the paper by RR Nigmatullin "Fractional integral and its physical interpretation". *Theoretical and Mathematical Physics*, **100**:1154, 1994.

[106] R. Cioć. Physical and geometrical interpretation of Grünwald-Letnikov differintegrals: measurement of path and acceleration. *Fractional Calculus and Applied Analysis*, **19**:161, 2016.

[107] S. Bhalekar and M. Patil. Nonexistence of invariant manifolds in fractional-order dynamical systems. *Nonlinear Dynamics*, **102**:2417, 2020.

[108] F. Balibrea-Iniesta, C. Lopesino, S. Wiggins, and A.M. Mancho. Lagrangian descriptors for stochastic differential equations: a tool for revealing the phase portrait of stochastic dynamical systems. *International Journal of Bifurcation and Chaos*, **26**:1630036, 2016.

[109] G. Duffing. *Erzwungene Schwingungen bei Veränderlicher Eigenfrequenz und ihre Technische Bedeutung*. Friedrich Vieweg & Sohn, 1918.

[110] A.H. Salas Salas, J.E. Castillo Hernández, and L.J. Martínez Hernández. The Duffing oscillator equation and its applications in physics. *Mathematical Problems in Engineering*, **2021**:1, 2021.

[111] J. Sunday. The Duffing oscillator: applications and computational simulations. *Asian Research Journal of Mathematics*, **2**:1, 2017.

[112] H.J. Korsch, H.J. Jodl, and T. Hartmann. *Chaos: A Program Collection for the PC*. Springer Berlin Heidelberg, 2008.

[113] J. Daquin, R. Pédenon-Orlanducci, M. Agaoglou, G. García-Sánchez, and A.M. Mancho. Global dynamics visualisation from Lagrangian descriptors. Applications to discrete and continuous systems. *Physica D: Nonlinear Phenomena*, **442**:133520, 2022.

[114] C. Lopesino, F. Balibrea, S. Wiggins, and .A.M Mancho. Lagrangian descriptors for two dimensional, area preserving, autonomous and nonautonomous maps. *Communications in Nonlinear Science and Numerical Simulation*, **27**:40, 2015.